University of Nevada, Reno

EXPLORING TWISTED STRING ACTUATION FOR APPLICATION IN SOFT ROBOTICS

A Dissertation Submitted in Partial Fulfillment

of the Requirements for the Degree of Doctor of Philosophy in

Mechanical Engineering

by

Revanth Konda

Dr. Jun Zhang / Dissertation Advisor

December 2023

THE GRADUATE SCHOOL

We recommend that the dissertation
prepared under our supervision by

entitled

be accepted in partial fulfillment of the
requirements for the degree of

Advisor

Committee Member

Committee Member

Committee Member

Graduate School Representative

Markus Kemmelmeier, Ph.D., Dean
Graduate School

ABSTRACT

To make robots more ubiquitous, robotic structures that are compliant, lightweight, and low-cost are desired. Soft robots, which are fabricated using compliant materials and soft actuators, are ideal for such applications. However, producing high-performance soft robots is challenging due to the lack of systematic procedures and inherent limitations of the actuators which drive them. Despite many advances in the field of soft actuators and artificial muscles, the quest for an ideal soft actuator which exhibits sufficient contraction and force generation, while being compact is still an ongoing effort. In an attempt to explore novel actuation techniques for soft robotics, in this dissertation, the employment of twisted string actuation for soft robotic applications is investigated and potential limitations which arise as a consequence are addressed. Due to their tendon-based (muscle-like) linear actuation, high force generation, and high operational bandwidth, twisted string actuators (TSAs) are highly suitable to actuate soft robotic devices with advantages over other soft actuators. TSAs typically generate strains of 30–40% of their untwisted length, exhibit energy efficiency of 75–80%, and can exert more stress than skeletal muscles. Although TSAs have been widely adopted in multiple robotic applications, their inclusion in soft robots has been limited.

In this dissertation, the application of TSAs in soft robotic manipulation is explored, in that a soft robotic manipulator is presented. The design of the robot is discussed. A physics-based model is developed to predict the manipulator's kinematic motion. An inverse model is derived to realize open-loop control. The proposed modeling and control approaches were experimentally verified to be effective. While the proposed soft robot exhibited promising performance, there were a few notable limitations due to the soft material and actuation mechanism: Firstly, the usage of soft material resulted in the nonlinear behavior called hysteresis. In addition, termed as

lonely stroke, the first input-output cycle of the soft robots was inconsistent with subsequent cycles that were repeatable and exhibited hysteresis. The lonely stroke not only affected the behavior of the hysteretic system, but also presented coupling with the subsequent repeatable hysteresis cycles. As a part of this dissertation, a model to capture and compensate for the hysteresis with lonely stroke property is proposed. A modeling approach is developed through the expansion of the input range of the Preisach operator, a widely adopted hysteresis model, to physically infeasible region. The effectiveness of the proposed scheme was validated by simulation and experimental results.

Secondly, most existing studies on control of TSAs assume that the external force applied to the TSA is measurable or predictable. Furthermore, existing studies also assume that all the TSA parameters such as the motor properties and string stiffnesses are accurately known. However, the system parameters could be difficult to measure, could change over time due to general wear and tear, and creep. The external forces applied to the TSA could be difficult to predict or measure. To address these issues, parameter estimation and control strategies were developed for TSAs, assuming little or no knowledge about the system parameters. A parameter estimation strategy which utilized the least squares algorithm and gradient algorithm is presented. An adaptive control strategy based on model reference control with feedback linearization is proposed. The developed estimation and control strategies were tested to be effective through simulation.

Lastly, the limited strain exhibited by TSAs adversely affected the design and performance of the soft robot. Therefore, it is strongly desirable but challenging to enhance the TSAs' consistent strain generation while maintaining compliance. Existing studies predominantly considered coiling after the regular twisting stage to be undesirable—non-uniform and unpredictable knots, entanglements, and coils

formed to create an unstable and failure-prone structure. Coiling would work well for TSAs when uniform coils can be consistently formed. As a part of this dissertation, we realize uniform and consistent coil formation in coiled TSAs, which greatly increases their strain. Furthermore, we investigate methods for enabling uniform coil formation upon coiling the strings in a TSA and present a procedure to systematically "train" the strings. Coiling resulted in approximately 70% strain in stiff TSAs and approximately 60% strain in compliant TSAs. TSAs capable of operating in the coiling phase were termed as twisted and coiled string (TCS) actuators.

To further establish the coiling mechanism as a reliable actuation mode for TCS actuators, the behavior of the TCS actuators in the coiling phase was experimentally characterized. The non-smooth behavior was investigated by using sequences of input motor turns with different frequencies. The hysteretic behavior and the properties of transitioning conditions were examined by applying input cycles with different bandwidths and under multiple loading conditions. Secondly, a physics-based kinematic modeling strategy which utilized the geometry of the coiled strings were developed to capture the behavior of the coiling-induced non-smooth behavior of the TCS actuators. Lastly, the kinematic model was inverted to realize open-loop control of TCS muscles through inverse compensation. The proposed modeling and control strategies were experimentally validated to be efficient.

To my sister, parents, family members, and my partner Roshika

ACKNOWLEDGEMENTS

Firstly, I want to express my sincerest gratitude to my Ph.D. advisor Dr. Jun Zhang, for giving me the opportunity to pursue a doctoral degree under his invaluable guidance in the Smart Robotics Lab. Since the beginning of my program at UNR, Dr. Zhang has been an indispensable source of knowledge and inspiration for me. I am forever in debt for his unwavering support throughout my Ph.D. program on various aspects including research and academics, scholarship and award nominations, and future career plans. I am forever grateful for his imperative advice on career and life in general, and for being responsible for making me a competent researcher. Secondly, I want to express my heartfelt thankfulness to my Masters' advisor Dr. Ji-Chul Ryu, for his guidance and support during my initial days as a graduate student. I sincerely thank him for giving me the opportunity to work under his guidance, being extremely patient with me, and encouraging me to pursue a Ph.D degree.

Thirdly, I want to thank my Ph.D. dissertation committee members Dr. Hung (Jim) La, Dr. Petros Voulgaris, Dr. Matteo Aureli, and Dr. Yantao Shen for providing critical feedback and help with improving my doctoral dissertation. Fourthly, I want to thank all the professors with whom I have taken courses. I have greatly benefitted by all the courses I have taken as a graduate student. Fifthly, I want to thank all my colleagues from the smart robotics lab who worked with me during the five years of my Ph.D. program. I want to specifically thank my colleagues David Bombara, Dr. Thulani Tsabedze, Steven Swanbeck, and Aaron Baker with whom my relationship has transcended from professional to personal. Special mentions to David Bombara with whom I have worked on most of my research projects, and Dr. Thulani Tsabedze who has been a constant since the beginning of my Ph.D. program. Sixthly, I want to thank my friends, most notably Dr. Gurlaz Kaur Mangat and Gaurav Srikar, and my colleagues from the Department of Mechanical Engineering

for making graduate school more enjoyable. I am grateful to the UNR College of Engineering, Graduate School at UNR, and the Graduate Student Association for providing scholarships, and awards which have greatly helped me.

Seventhly, I want to thank my parents, sister, and all family members, for their enormous support with all my endeavors including pursuing a doctoral degree. Special mention to my sister Mrs. Chandra Rekha Srinath Konda for her love and care in good times and more importantly, in difficult times. Special mention also, to my parents Mr. Sasidhar Konda, Mrs. Sudha Rani Srinath Kashaboina, and my uncle Mr. Murali Kashaboina for sowing the seed of pursuing a doctoral degree. I also want to mention my late grandparents, who would have been elated and jubilant had they been present during my graduation.

Last but not the least, I want to thank my partner, Roshika, for her overwhelming support through the highs and lows of graduate student life. I want to express my sincerest gratitude to her for her massive encouragement in turbulent times, and for celebrating all my achievements. She has been a huge source of inspiration for me throughout my Ph.D. program and my Ph.D. journey could not have been the way it was without her.

TABLE OF CONTENTS

LIST OF TABLES

LIST OF FIGURES

CHAPTER 1

INTRODUCTION

1.1 Soft Robotics

To make robots more ubiquitous in scenarios where safe interaction with humans is necessary, it is highly desirable but challenging to realize robotic structures that are safe, compliant, low-cost, and generate sufficient force. Soft robots are ideal for these applications. Soft robots are defined as robotic structures that are realized using soft materials or compliant actuators (1). Numerous useful motions have been achieved using soft robots, such as grasping, crawling, walking, and swimming (2; 3; 4; 5; 6; 7; 8). Soft robots are often realized using artificial muscles as their driving mechanisms. However, high-performance soft robots are challenging to realize because most soft actuators and artificial muscles that drive existing soft robots exhibit some evident limitations.

1.2 Artificial Muscles

Artificial muscles are a class of soft actuators that are widely adopted in numerous soft robots (9). Artificial muscles generate motion by varying their shapes due to external stimuli, such as voltage or temperature (10; 11). Artificial muscles exhibit desirable properties like compliance, high power-to-weight ratio, and low mass (10; 9). This gives them strong potential as driving mechanisms for advanced robotic applications (12; 13). Some of the popular artificial muscles used to actuate soft robots are pneumatic actuators, dielectric elastomer actuators (DEAs), hydraulically

amplified self-healing electrostatic (HASEL) actuators, shape memory alloy actuators (SMAs), supercoiled polymer (SCP) actuators.

1.3 Limitations of Existing Soft Robots

While artificial muscles have been employed to drive numerous types of soft robots, the functionalities of the soft robots are often limited due to the inherent limitations of the artificial muscles used to drive them. These may include (1) fabrication complexity ([4]; [14]), (2) high power requirement ([15]; [16]), (3) slow actuation ([17]; [18]), and (4) insufficient force generation ([19]; [18]; [20]). DEAs and HASEL actuators generate sufficient actuation, but it is challenging to realize their complicated and high-cost fabrication procedures ([14]; [16]). DEAs and HASEL actuators also demand high-voltage equipment which is not only costly but also could be potentially dangerous. Magnetorheological (MR) elastomers generate acceptable ranges of force and displacement, but they require large rigid parts to generate magnetic fields which are utilized for actuation ([21]; [22]). This could lead to difficulty in including them in compact devices. Similarly, pneumatic actuators exhibit appreciable strain and force generation, but adopting them in robotic devices demands the inclusion of pumps or compressors ([23]; [24]). Furthermore, the thermal actuation of SMAs ([17]; [25]; [26]) not only results in low bandwidth and low force generation, but also could be dangerous and cause damage to the soft robotic devices in which they are employed. In addition, ionic polymer-metal composite (IPMC) actuators which display acceptable strain generation at low voltages, exhibit low power-density and low-stress ([9]; [20]). As such, the quest for an ideal soft actuator which exhibits sufficient output strain and output force generation, while being compact is still an ongoing effort.

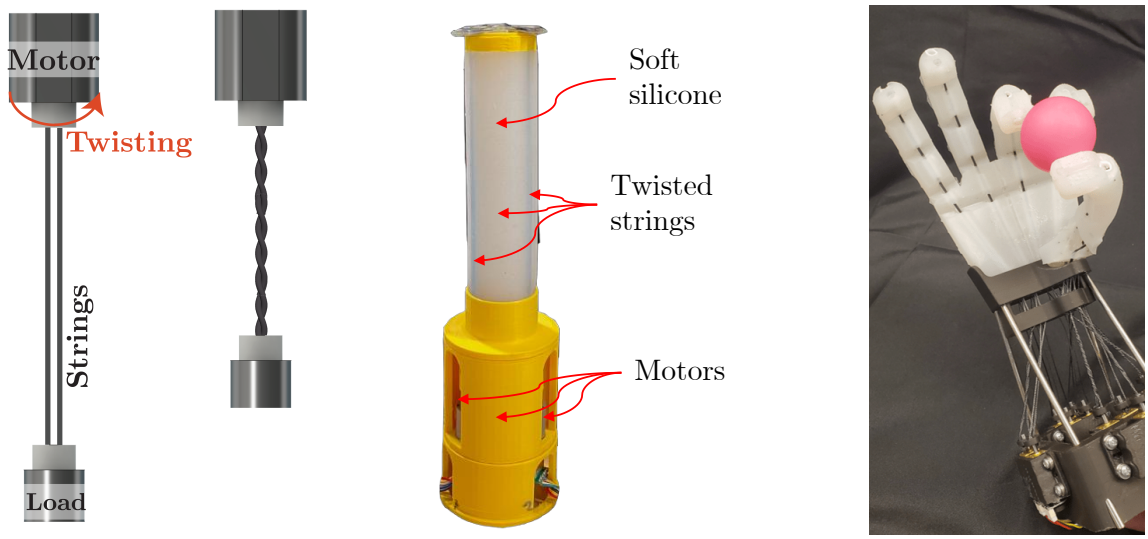

(a) (b) (c) (d)

Figure 1.1: The twisted string actuator (TSA) in (a) fully untwisted state and (b) twisted (actuated) state. (c) The TSA-driven soft robotic manipulator. (d) A TSA-driven anthropomorphic soft robotic manipulator.

1.4 Twisted String Actuators (TSAs)

A twisted string actuator (TSA) is an artificial muscle that consists of at least two strings connected to an electric motor at one end and a load at the other end of the strings (27; 28). As shown in Fig. 1.1(a)–(b), actuation is realized by twisting the strings with a motor to shorten the strings' length and linearly displace the attached load (27). TSAs typically generate strains of 30–40% of their untwisted length, exhibit high energy efficiency, and can exert more stress than skeletal muscles (27). A similar actuation mechanism to TSAs is the motor and spool actuator, which has been used to drive cable-driven robots (9; 29). TSAs are advantageous over a motor and spool configuration: TSAs convert rotational motion to translational motion without the use of any external mechanisms like gears (30). In addition, the TSA's motor is placed in line with the strings' linear motion, whereas with a motor and spool, the motor is perpendicular to the string's linear motion. Furthermore, TSAs can output higher

forces with less input torques than motors and spools (31; 32). Due to these reasons, TSAs are more efficient than the motor and spool configuration. A brief study on the comparison of torque outputs of TSAs and motors with spools was recently conducted (33).

1.5 Motivation

Actuating soft robots with TSAs or other twisting-based actuators (34) could present unique advantages over other actuation mechanisms (19; 23). These advantages are due to TSAs' simplicity in fabrication and assembly, low power requirement, high energy efficiency, high linearity, and compactness (9). Although TSAs have been widely employed in multiple robotic applications, such as tensegrity robots, robotic fingers, robotic hands, and exoskeletons (30; 35; 36; 37), their applications in soft robots have been limited. This is likely because motors are required to construct TSAs and are thus difficult to be incorporated into soft structures. Meanwhile, the successful applications of TSAs in exoskeletons and assistive devices (38; 33; 39) demonstrate their strong promise in areas where safe interaction with humans is demanded. Although the strings used in traditional TSAs are not stretchable, the compliant properties of the twisting configuration could be very useful in soft robots. Furthermore, by employing stretchable strings, the compliance of the TSAs could be greatly enhanced. More recent studies have presented the design and analysis of compliant TSAs (40; 41; 42).

1.6 Proposed Work

The primary goal of this dissertation is to explore the employment of TSAs to actuate a set of soft robots. More specifically, the employment of TSAs to drive soft robots utilized for manipulation is investigated. To this end, a TSA-driven soft robotic manipulator (Fig. 1.1(c)), which was a *first* soft robotic device to use TSAs as the driving mechanism is presented. The advantages of utilizing TSAs to drive soft robots in the context of overall performance, modeling, and control synthesis are explored through the proposed robot. The usage of TSAs facilitated the use of many number of TSAs while maintaining the overall footprint of the actuator in acceptable ranges. While the proposed robot exhibited acceptable performances, it exhibited a few evident limitations which will be discussed in detail in Chapter 2. While most of these limitations were specific to a given robot, two critical limitations which affected the design and performance of TSA-driven soft robots were identified as follows:

- The *usage of soft material* for constructing the robots greatly enhanced their compliance. However, the soft material introduced complex nonlinearities into the behavior of the robots.
- The assumption that all TSA system parameters are accurately known and will remain constant may introduce error in the control scheme of TSAs as the string and motor parameters could change over time due to general wear and tear, and creep.
- The *limited output contraction* exhibited by TSAs affected the actuation of the soft manipulator, since embedding the strings into the soft material resulted in unwanted interaction of the twisted strings with the soft material.

The limitations mentioned above will be discussed in further detail in Chapter 2.

The secondary goal of this dissertation is address the aforementioned limitations and provide feasible solutions to overcome them. Firstly, the nonlinear behavior which manifests due to the usage of soft material in soft robots is analyzed and a model is proposed to accurately capture it. The proposed model utilizes a common hysteresis model namely the Preisach operator to capture the aforementioned nonlinear behavior. Secondly, the change in TSA system parameters over time is addressed by proposing parameter estimation and adaptive control schemes based on their kineto-static and dynamic models. Lastly, the issue of limited output contraction of TSAs is examined and a potential solution in the form of coiling the strings is studied.

The remainder of this document is organized as follows: The proposed soft robotic manipulator driven by TSAs is presented in Chapter 2. The evident drawbacks of the TSA-driven soft robots are detailed in Chapter 2. The modeling, and open-loop control of the nonlinear behavior encountered in soft material is discussed in Chapter 3. The parameter estimation and adaptive control of TSAs is presented in Chapter 4. The fabrication and performance characterization of the twisted and coiled string actuators, which are TSAs capable of actuation through twisting and coiling, is presented in Chapter 5. The detailed experimental characterization of the behavior of twisted and coiled actuators in the coiling mode of actuation is presented in Chapter 6. Chapter 7 includes the modeling and inverse compensation of the unique coiling-induced non-smooth behavior of twisted and coiled string actuators in the coiling phase. Conclusions and future work of this dissertation are presented in Chapter 8.

CHAPTER 2

TWISTED STRING ACTUATED SOFT ROBOTIC MANIPULATOR

In this chapter, we present the design, characterization, modeling, and open-loop control of a multiple degree-of-freedom (DOF) soft robotic manipulator powered by TSAs (Fig. 1.1(b)). Firstly, the soft manipulator was designed and fabricated to include TSAs for high performance. Secondly, the robotic device was experimentally characterized in terms of its bending angle and axial force from a single TSA. Thirdly, a physics-based model to capture the kinematic behavior of the soft manipulator was derived. The model was extended to three-dimensional (3D) space to estimate the position of the end point of the manipulator, given the twists of the TSAs. Fourthly, an inverse kinematic model was derived to enable open-loop control of the manipulator's bending angle. Fifthly, the proposed modeling and control strategies were experimentally validated. Lastly, the chapter is concluded with discussions on drawbacks of the presented work. The contents of this chapter are based on the findings presented in (44; 45; 46).

2.1 Design and Fabrication

2.1.1 Related Work

The design was inspired by existing studies (19; 23) that developed soft robotic manipulators. (19) reported a general soft robotic module actuated by twisted and coiled actuators (TCAs). Despite their similarities, TCAs and TSAs are significantly different. For example, both TSAs and TCAs have been used to develop haptic

devices ([47]; [48]). Although both actuators are tendon-based actuators, TCAs contract under applied heat (commonly in the form of Joule heating). TCAs are very energy-inefficient, whereas TSAs are highly energy-efficient when compared to other actuators ([9]). Similar to our work, the soft robot from ([19]) contained three actuators embedded inside a silicone elastomer. However, it was capable of exerting significantly less force than our TSA-driven soft robot. The relatively low force output of TCAs limits their applicability to larger-scale robots such as ours. For that reason, the robot by ([19]) is on the scale of a finger as opposed to a manipulator. Soft robotic gripper sensor skins for haptic object visualization were reported by ([23]). Although the main contribution was the sensor skins, it used pneumatic soft robotic fingers made of silicone elastomer to test the sensor ([23]). Pneumatic devices require air compressors that add much volume and mass to the system. By using TSAs, as opposed to other actuators, our robot is capable of high output forces without requiring bulky equipment — future iterations of our robot could be untethered.

2.1.2 Robot Body

The body of the robot which was comprised of a soft silicone manipulator and rigid base will be discussed in this section. The soft manipulator, as shown in Fig. 2.1, was constructed from Smooth-On Ecoflex™00-50 silicone via a 3D-printed mold. The mold was designed to be printed quickly and be disposable. The wall thicknesses of each mold part were chosen to be 0.8 mm, which was twice the nozzle diameter of the 3D printer. The thickness was chosen to optimize slicing and printing. The thin walls also allowed the model to be quickly broken apart to retrieve the cast arm. The soft arm, which was 175 mm long, utilized three internal channels for the TSAs to travel through to facilitate bending. The channels were placed evenly at angles 120°

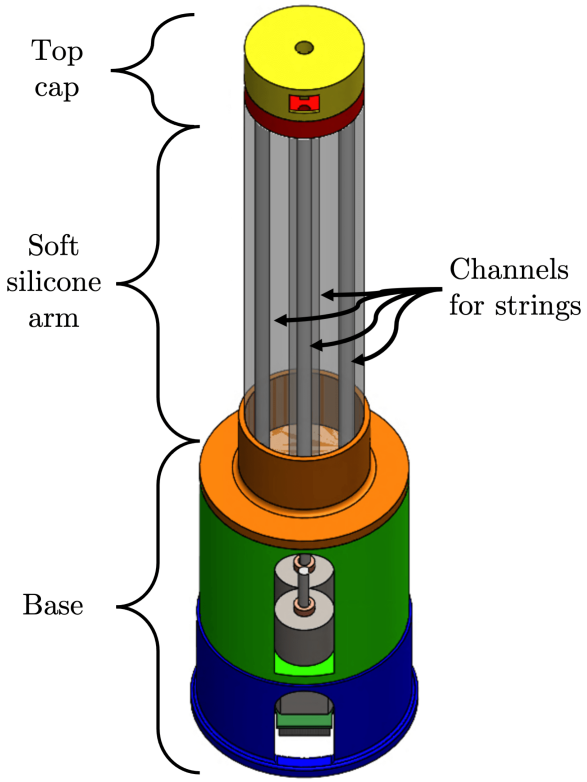

Figure 2.1: Model of the TSA-powered soft robotic manipulator.

from each other near the circumference of the arm. A channel was also provided in the center of the manipulator to place an additional TSA which could actuate and attached gripper.

The soft manipulator utilized three TSAs to enable bending in different directions, thereby providing the robot with multiple DOF. The manipulator moved by actuating the TSAs, where each TSA could twist by varying amounts independently or in conjunction with one another to bend in different directions. The base of the manipulator housed the motors for actuating the TSAs and encoders to measure the number of twists.

2.1.3 Actuators

This study utilized two strings with the same length and material properties to construct each TSA. More strings with different material properties could also be used ([27; 49]). The strings were hung vertically in tension with one end attached to the motor shaft. The free end of the strings was attached to the top cap of the arm and was constrained such that the arm bent due to the TSA's contraction. More information on the design and assembly of TSAs can be found in previous work ([27; 49]).

2.1.4 Materials

Now that the design of the manipulator has been discussed, we will detail the fabrication process. All rigid parts of the manipulator were 3D printed on a traditional fused deposition modeling (FDM) printer from acrylonitrile butadiene styrene (ABS) plastic. The base section was designed using a peg-and-slot system to be printed separately and efficiently, reducing support material, printing time, and printing cost. The manipulator had a mass of approximately 710 g. This included the motors and inertial measurement unit (IMU) but did not include the circuit boards located outside the manipulator. Leading up to the arm, the topmost base section used friction to grip the outer diameter of the arm so that it did not fall off of the base. The tension induced by the TSAs also allowed the arm to remain attached to the base. The top cap was attached to the ends of the TSA. These pieces were attached both by (a) friction against the inner diameter of the center channel and (b) tension from the twisted strings. Additionally, the simple design of the end piece allowed for any type of end-effector to be attached. The TSAs were realized using polyethylene (UHMWPE) strings with diameters of 1.3 mm. This material and diameter were chosen due to

their high strength and usage in previous studies ([27]).

2.1.5 Electronics

The electronics, such as the microcontroller, were placed outside of the robot and were wired to the motors. A microcontroller based on the ATmega2560 microchip (MEGA 2560 R3 Board, Elegoo) with brushed DC motor drivers (DRV8871, Adafruit) controlled the robot. Four 46-g brushed DC motors (Metal Gearmotor 20Dx44L, Pololu) with a 125:1 gear ratio were chosen to twist the pairs of strings. Each DC motor utilized a dual-channel Hall-effect sensor board to track the motor rotations. Accounting for the gear ratio, the encoders enabled 2500 counts per revolution (CPR), which corresponded to 0.144°-resolution sensing of the angle of the motor output shaft. With a 12-V input, each motor was able to output 7.8 kg·cm of torque before stalling. The total cost of all materials and electronics was approximately 240 USD.

An IMU (VR IMU Breakout - BNO080, Sparkfun) was utilized to measure the orientation of the soft TSA-driven arm. According to the manufacturer, the measurement uncertainty of the angle of the IMU was 3.5°. Although the measurement uncertainty may have been greater than in other devices, its low cost (approximately 35 USD) kept the overall cost of the robot low. The IMU returned the orientation in terms of roll, pitch, and yaw angles (Tait-Bryan angles).

2.2 Experimental Characterization

The design and fabrication of the robot revealed two crucial variables to experimen-

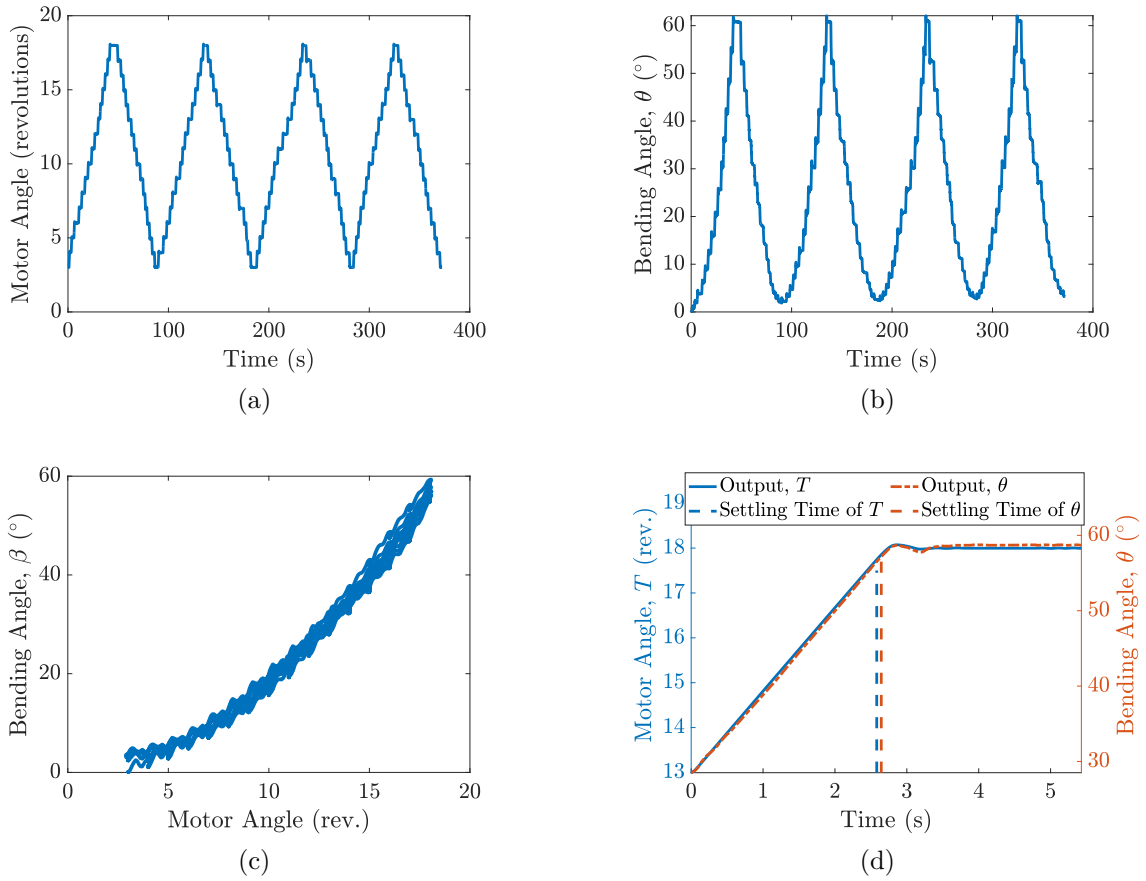

Figure 2.2: (a) Applied motor angle θ input sequence. (b) Bending angle β versus time. (c) The correlation between θ and β. (d) A comparison of the transient response of the experimentally obtained θ and β.

tally characterize: the bending angle of the soft manipulator and axial force of the TSA. The bending angle β and axial force F_z of the TSA-driven soft robot were characterized in relation to the TSA's motor angle θ. The input sequence for this experimental characterization is provided in Fig. 2.2(a). The motor rotations were applied in monotonically increasing, then monotonically decreasing steps for four complete cycles. The motor was actuated in steps of 1 rotation and paused for 2 s to ensure the motor angle became steady. The motor angle was only slightly underdamped such that the motor angle experienced one period of oscillation. The 2-s pauses were mainly to ensure that the bending angle became steady, which oscillated

at low bending angles. The motor angle (twists in the TSA) varied between 3 and 18 revolutions (rev). The initial offset of three rotations was introduced to the motor to ensure the actuating strings were taut. However, this offset was not applied for the other (non-actuating) motors to ensure that they did not exert significant force to oppose the motion of the manipulator. Because TSAs require tension to actuate, this offset had a negligible effect on the initial bending angle of the manipulator.

The bending angle versus time and motor angle is shown in Fig. 2.2(b)–(c). The bending angle was measured about the axis normal to the actuating motor shaft. As expected, mild hysteresis was observed, which was commonly observed in TSAs in previous work (40; 27). One experimental observation was that, during some experiments, the softness of the silicone in the arm caused the bending angle to slightly oscillate. However, the oscillations only occurred at low motor angles when the TSA underwent high jerk and the silicone was still soft. In addition, the oscillations quickly decayed due to the silicone's inherent damping. The bottom of the silicone tube was fixed to the rigid TSA base via the tension in the strings. Thus, at low twisting angles, there was not enough stress applied to the silicone to dampen the free oscillations. The manipulator was fabricated this way to simplify the modeling strategy, which will be presented in detail in the next section.

The oscillations could potentially be suppressed via feedback from the IMU. The IMU could detect the oscillations which would instruct the microcontroller to adjust the motors' input voltages. Another way to suppress these oscillations could be to induce additional pre-twists and therefore pre-tension in each of the TSAs. These strategies were not implemented in the current work, because the main goals in this study were to (1) characterize the manipulator's behavior absent advanced control strategies and (2) realize open-loop control in order to test the accuracy of the pro-

posed model.

Because the TSA's twists stiffened the silicone as it bent, the maximum attainable oscillation amplitudes also decreased as the silicone's bending angle increased. By starting the experiment with three initial twists in the TSA, these oscillations were mostly avoided. For tests on angular velocity (presented in Section 2.4.1), any remaining oscillations present in the data were filtered using a Savitsky-Golay filter (50) during the analysis. The filter was only utilized to display the results, and not during the real functioning of the system.

During a separate experiment, the soft manipulator achieved a maximum bending angle of 97.4°at 21 motor rotations. The maximum bending angle depended on (1) the toughness of the silicone and (2) maximum attainable twists in the strings. Although it was physically possible to bend beyond 97.4°, the silicone risked breakage due to the high stresses exerted by the strings on the inner walls of the channels in the arm. In Fig. 2.2(d), the bending angle is shown to closely follow the transient motor angle — there is negligible phase offset between the two signals. Their settling times T_s are similar: $T_s = 2.61\,\text{s}$ for θ and $T_s = 2.67\,\text{s}$ for β. The settling time was defined as the time in which the output variable reached and stayed within 5% of its steady-state value. The system settled before reaching its peak because it did not exit the 5% error bound after it reached the peak. The aforementioned oscillations in β are not present in Fig. 2.2(d) because of the high motor angles (13–18 rev). Fig. 2.2(d) shows that there is almost no phase delay between θ and β.

Secondly, the axial force F_z exerted by the manipulator on the TSA was studied. The force measurements were recorded using force-sensitive resistors (FSR-404, Interlink Electronics). The axial force versus time is shown in Fig. 2.3(a). An initial force of 4.57 N kept the strings taut. The force–motor rotations correlation showed evident

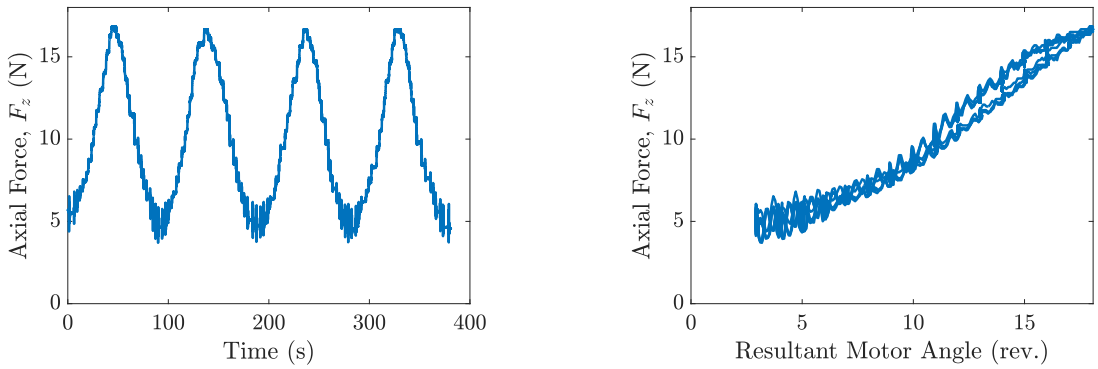

Figure 2.3: (a) Axial force F_z versus time. (b) Correlation between θ and F_z.

hysteresis (Fig. 2.3(b)); the force during twisting was greater than the force during untwisting. The material properties of the silicone could be one potential reason for hysteresis. Furthermore, previous studies have demonstrated the frictional effects of TSAs due to the strings' sliding along surfaces (51) or placement in conduit (52) as another potential cause for hysteresis. The maximum difference between the force due to hysteresis was around 1.37 N. At the starting and ending motor rotations, the forces during twisting and untwisting were approximately equivalent. At 18 motor rotations, the TSA exerted an axial force of approximately 16.85 N. At increased motor angles, the oscillations in F_z disappeared because the silicone stiffened. The results of the experimental characterization suggest that β and F_z may be predicted using physics-based models.

2.3 Modeling

2.3.1 Related Work and Motivation

Numerous modeling strategies have been proposed for soft robots over the past decade. These strategies are often developed based on standalone or a combination of multiple techniques ranging from data-driven approaches (53), finite elements analysis (54), continuum mechanics (55; 56), and actuator-specific models (57; 56). The first step towards developing models for soft robots is to capture the interaction between the robot and the actuator used to drive it. While these interactions have been extensively studied for soft robots driven by several popular artificial muscles (54; 56), TSAs have had limited uses in soft robotics. Consequently, modeling and control of TSA-driven soft robots have not been sufficiently studied. A similar type of actuation mechanism which has been employed to drive soft robots is the spooled motor tendon actuation (SMTAs) (29; 9). While TSAs and SMTAs are both motor based actuators and result in tendon-driven soft robots, there are evident differences: TSAs convert rotational motion to translational motion without the use of any external mechanisms like gears (30). As a result, the models describing the behaviors of TSAs and SMTAs are significantly different (33). While tendon-driven soft robots have been extensively studied in the literature (57; 58), TSA-based soft robots have received little attention.

Besides superior performance metrics (9), TSAs also possess advantages in terms of modeling and control: Unlike many soft actuators, the behavior of TSAs can be captured using traditional models which were derived using first principles (27). TSA models not only result in closed form solutions but also provide scope for further analysis in terms of stability and controllability (59). In terms of design and performance, the unique advantages of adopting TSAs to drive soft robots have been explored in

our recent works (44; 43; 60). However, to fully unleash TSAs' potential in the field of soft robotics, it is essential to develop modeling and control strategies for TSA-driven soft robots. The models presented in this work are based on the kinematic interactions between the soft robot and the TSAs used to drive them. The study was restricted to kinematic modeling of the considered soft robotic manipulator for two reasons: Firstly, previous studies on soft robots actuated by other actuators have indicated that while accuracy is slightly sacrificed, efficient control of soft robots can be achieved using kinematic models (53; 61). Secondly, previous studies on TSA-driven robots have demonstrated that kinematic modeling results in efficient and accurate robot control (37; 38; 35; 62). Furthermore, due to the simplistic design of the soft manipulator considered in this study, the presented models could be generalized to other soft robots driven by TSAs such as the soft gripper developed in (43).

2.3.2 Single TSA kinematic Model

The single TSA model predicts the bending angle of the manipulator under the actuation of a single TSA. The diagram of the robot is provided in Fig. 2.4. Table 2.1 summarizes the model variables. The model is relied on the following assumptions:

1. The manipulator bends with a curvature κ that is constant across the entire arc length X.
2. The center length of the silicone body of the manipulator, L, is constant during bending.
3. When a single TSA induces bending of the manipulator, the value by which the inner arc length of the manipulator decreases is equal to the TSA contraction.

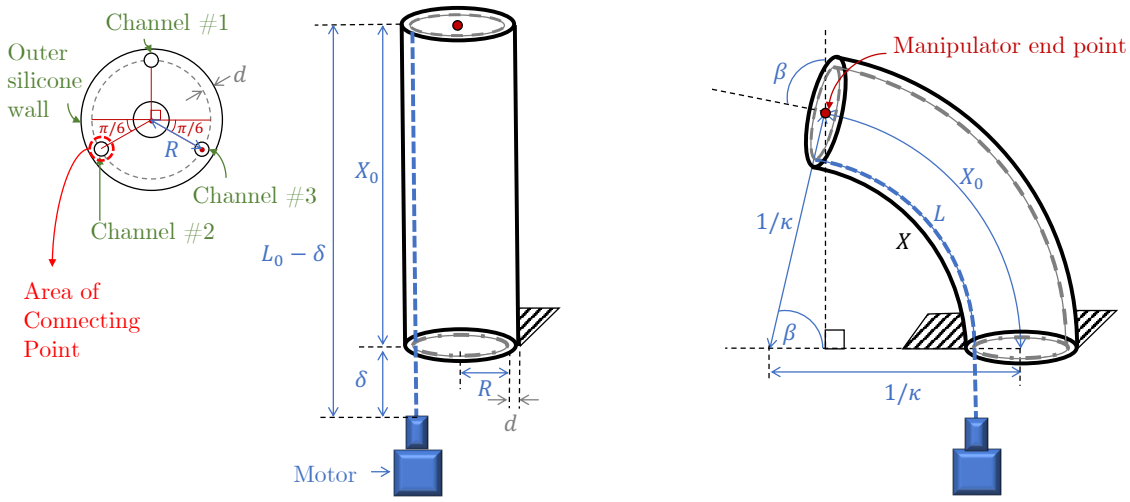

Figure 2.4: The diagram of the TSA-driven manipulator, with relevant variables labeled. (a) The manipulator in unactuated state. From the top view of the robot, the motors are placed 120°apart. (b) The manipulator in the actuated state.

If all TSAs in the manipulator are fully untwisted, then their lengths L are slightly greater due to slack.

4. Within the bending range of the manipulator, the effect of the untwisted TSAs is localized to the area around its point of connection with the manipulator and does not affect the center length of the manipulator.

5. The stiffness of the TSA is great enough such that, within the range of tested loads, the axial force F_z on the TSA alone caused negligible strains in the TSA.

6. The propagation of twists of the TSAs induced by the motor is uniform across the length of the strings, and the friction between the TSA and the manipulator's channels does not affect TSA's actuation.

Assumptions #1 and #2 have been previously used in studies on soft robotics ([63]; [19]; [4]). A direct implication of Assumption #1 is that the robot operates in free space without any obstacles. Assumption #3 is valid due to the locations of the motors

Table 2.1: Variables names and symbols for the robot.

	Symbol	**Unit**
Manipulator		
Bending angle	β	°
Bending direction	α	°
Curvature	κ	m
TSA		
Motor angle	θ	revolutions
Radius	r	m
Axial force	F_z	N

relative to the silicone. Furthermore, a small amount of slack was introduced into strings to mildly compensate for the increase in the silicone length due to bending. Due to this, within the tested range, the untwisted TSAs not only exerted negligible tension on the soft robot, but also had a dead zone where the insertion of twists in the initial actuation stages did not result in significant actuation. However, it was observed that after initial actuation, even with slack, the untwisted strings exerted some tension on the silicone. Meanwhile, it was also observed that the tension exerted by the untwisted TSAs had an effect which was localized to the volume around the conduit and did not greatly affect the center length of the manipulator. Based on these observations, Assumption #4 was also considered. Assumption #5 has precedent in the TSA literature ([59]; [49]; [27]). Within the bending range of the manipulator, the forces exerted on the TSAs did not show significant effect on the length of the TSAs. The stiffness of a single 1.3-mm UHMWPE string was measured to be 1013 N, normalized to its unit length of 1 m. The conventional kinematic model of the TSA relies on Assumption #6 ([27]; [49]). Assumption #6 is valid with the tested range of actuation. To relax assumption #6, modeling strategies from a previous study by ([64]) can be used.

Bending Angle

Let β be the bending angle of the manipulator in radians. Based on the experimental characterization results presented in (44), $\beta \in [0, \pi/2]$. Although our recent study showed that β could reach beyond 97.4° (44), this range was deemed to be the safe range within which the manipulator could bend consistently without performance degradation or damage of the silicone body of the manipulator. The arc length X can be expressed as

$$X = \beta\left(\frac{1}{\kappa} - R\right), \tag{2.1}$$

where curvature, κ, is the inverse of the radius of curvature, and R is the distance between the center of the manipulator and the TSA's strings. Note that R is not the radius of the manipulator itself, which is slightly larger than R. As shown in Fig, 2.4, d is the difference between R and the manipulator's radius. The center arc length $X_0 = \beta/\kappa$, which can be rearranged as

$$\frac{1}{\kappa} = \frac{X_0}{\beta}. \tag{2.2}$$

Let X_0 be constrained as constant such that X_0 is also the arc length of the robot when it is not bent. During bending, X will decrease because the axial forces exerted by TSA will compress one side of the silicone body. Substituting Eq. (2.2) into Eq. (2.1) yields

$$X = X_0 - \beta R. \tag{2.3}$$

If L is the contracted length of the TSA, and δ is the distance between the connecting point of the strings with the motors and the base of the silicone body, then X and L can be correlated as $X = L - \delta$. As derived in previous studies (27; 49), the kinematic model of the TSA is given by

$$L = \sqrt{{L_0}^2 - \theta^2 r^2}, \tag{2.4}$$

where L_0 is the initial (untwisted) length of the TSA's strings, θ is the angle of the motor's shaft and r is the variable radius of the TSA. Consistent with existing studies and assumption #5, it is considered that the stiffness is infinitely large, and Eq. (2.4) does not have a stiffness term (49; 27). It is noted that recent studies considered compliant TSAs (49; 65).

According to (27), the variable radius r of the TSA can be computed by

$$r = r_0 \sqrt{\frac{L_0}{L}}, \tag{2.5}$$

where r_0 is the radius of the string when it is untwisted (49). In practice, r_0 can be measured with a caliper, but measuring L will be more challenging due to its time-varying property. Thus, L is estimated based on the previous estimate of r, such that

$$L[k] = \sqrt{{L_0}^2 - \theta[k]^2 r[k-1]^2}, \tag{2.6}$$

where k is the discrete-time index, $r[0] = r_0$, and $\theta[1] = 0$. $r[k]$ is computed by Eq. (2.5) based on $L[k]$.

Utilizing Eq. (2.3), Eq. (2.4) and the correlation between X and L, and then solving for β yields

$$\beta = \frac{X_0 - X}{R} = \frac{X_0 - \sqrt{{L_0}^2 - \theta^2 r^2} + \delta}{R}. \tag{2.7}$$

The validity of Eq. (2.7) depends on the validity of the assumptions. While most of the assumptions can be justified in a quantitative manner, the validity of Assumptions #2, #3 and #4 requires further justification through mathematical analysis. This is because, if Assumption #3 is true, it implies that the outer arc length of the manipulator only increases until the untwisted strings are taut and then

it would remain constant. Consequently, Assumption #2 which states that center arc length of the manipulator remains constant while bending, will be violated. To avoid this contradiction Assumption #4 was considered. To test the validity of these assumptions, we derive a model which drops the aforementioned Assumptions #2 and #4, and compare its ability to predict the bending angle against the proposed model (Eq. (2.7)).

As mentioned earlier, Assumption #3 implies that until the limit of the slack is reached by the untwisted TSAs, the outer arc length will increase by the amount by which the inner arc length is decreasing. After the limit of slack is reached, the outer arc length will remain constant. The outer arc length X_{outer} is described as

$$X_{\text{outer}} = \begin{cases} X_0 + (X_0 - X), & \text{if} \quad X_{\text{outer}} < L_0 - \delta \\ L_0 - \delta, & \text{if} \quad X_{\text{outer}} \geq L_0 - \delta. \end{cases} \tag{2.8}$$

Using Eq. (2.8), β can be computed as follows,

$$\beta = \frac{X_{\text{outer}} - X}{2R} = \frac{X_{\text{outer}} - \sqrt{{L_0}^2 - \theta^2 r^2} + \delta}{2R}. \tag{2.9}$$

Angular Velocity

In this study, three different models of the angular velocity, $\dot{\beta}$, are considered:

1. The "complete model" accounts for $\dot{r}$, the estimated rate of change in the TSA's radius.
2. The "conventional model" approximates that $\dot{r} = 0$. This model is accepted in the TSA literature (49; 59; 65).
3. The "linearized model" simplifies the conventional model by approximating dL/dt as a linear function of θ.

As reported in (27), differentiating Eq. (2.7) with respect to time yields

$$\dot{\beta} = \frac{\left(\dot{\theta}r + \theta\dot{r}\right)\theta r}{R\sqrt{{L_0}^2 - \theta^2 r^2}}. \tag{2.10}$$

Eq. (2.10) is the "complete model" because it accounts for $\dot{r}$, a variable that is impractical to measure during actuation. This means $\dot{r}$ must be derived analytically from Eqs. (2.4) and (2.5). Another option is to numerically differentiate the estimates of r. In this work, a Savitzky-Golay filter (50) is adopted for this purpose due to its ability to efficiently supress the noise while not significantly damping the actual profile of the signal. For clarity, the analytical derivation of $\dot{r}$ is provided below:

$$\dot{r} = \frac{r_0 {L_0}^{1/2}\theta r^2}{2L^{5/2} - r_0 {L_0}^{1/2} r\theta^2}\dot{\theta}. \tag{2.11}$$

Eq. (2.11) is used in Eq. (2.10) to obtain the complete mathematical description of $\dot{\beta}$.

In many previous studies on TSAs, $\dot{r}$ is assumed to be negligible (65; 49; 59). In that case,

$$\dot{\beta} = \left(\frac{1}{R}\frac{dL}{d\theta}\right)\dot{\theta} = \left(\frac{1}{R}\frac{r^2\theta}{\sqrt{{L_0}^2 - r^2\theta^2}}\right)\dot{\theta}. \tag{2.12}$$

The second model of $\dot{\beta}$ is Eq. (2.12), which is hereby named the "conventional model" because it approximates that $\dot{r} = 0$. This approximation is conventionally used in the TSA literature (49; 59; 65). Following the naming convention from (65), the quantity $dL/d\theta$ is known as the TSA Jacobian, which we denote by $h(\theta)$. This quantity also equals the inverse of the TSA transmission ratio (65). Although $h(\theta)$ also depends on r, r is implicitly a function of θ. According to the models in this study, $h(\theta)$ is

therefore ultimately a function of θ only. If a constant radius of the TSA is assumed, the Jacobian of the overall system is

$$\mathcal{J} = \frac{h(\theta)}{R}, \tag{2.13}$$

where

$$\dot{\beta} = \mathcal{J}\dot{\theta}. \tag{2.14}$$

Eq. (2.14) is another way to express Eq. (2.12).

The third model of $\dot{\beta}$ termed as the "linearized model", is obtained by computing the second-order approximation of $h(\theta)$ from Eq. (2.13) around $\theta = 0$ as follows.

$$h(\theta) = \sum_{n=0}^{\infty} \frac{h^{(n)}(\theta)}{n!}\theta^n = \frac{r^2}{L_0}\theta + \mathcal{O}(\theta^3), \tag{2.15}$$

where $h^{(n)}(\theta)$ is the n^{th} derivative of $h(\theta)$ with respect to θ. This defines linearization of the inverse transmission ratio $\tilde{h}$ and linearization of the system Jacobian $\tilde{\mathcal{J}}$ when $\theta \approx 0$, respectively:

$$\begin{aligned} \tilde{h}(\theta) &= \frac{r^2}{L_0}\theta, \\ \tilde{\mathcal{J}} &= \frac{\tilde{h}(\theta)}{R} = \frac{r^2}{RL_0}\theta. \end{aligned} \tag{2.16}$$

In this linear region, Eq. (2.14) can be simplified to

$$\dot{\beta} = \tilde{\mathcal{J}}\dot{\theta} = \frac{r^2\theta}{RL_0}\dot{\theta}. \tag{2.17}$$

Eq. (2.17) is the "linearized model". Detailed derivation of Eq. (2.17) can be found in (45).

It is also possible to find the range of motor turns where the linear approximation is within a given percentage tolerance λ by solving

$$\lambda = \frac{h(\theta) - \tilde{h}(\theta)}{h(\theta)} = 1 - \frac{\tilde{h}(\theta)}{h(\theta)} = 1 - \frac{\frac{r^2}{L_0}\theta}{\frac{r^2}{\sqrt{L^2 - \theta^2 r^2}}\theta}, \tag{2.18}$$

which can be simplified to

$$\lambda = 1 - \frac{\sqrt{L^2 - \theta^2 r^2}}{L} = 1 - \frac{X}{L}. \tag{2.19}$$

Solving for θ yields

$$\theta = \pm \frac{L}{r} \sqrt{1 - (1-\lambda)^2}, \tag{2.20}$$

where $[-\theta, +\theta]$ defines the region where the linear approximation of the inverse transmission ratio is within a percentage tolerance $\lambda \in [0, 1]$ of the nonlinear model. $\theta < 0$ indicates counterclockwise rotation of the motor. In particular, the utilization λ^* is defined to be

$$\lambda^* = \sqrt{1 - (1-\lambda)^2}. \tag{2.21}$$

This defines the percentage of the domain that the linearization approximates the inverse transmission ratio with percentage tolerance λ.

To test the validity of Eqs. (2.18)–(2.21), a simulation was conducted in which the achievable bending angle, strain, and motor angle were computed for a given percentage tolerance λ. The percentage tolerance from Eqs. (2.18)–(2.19) is the percentage difference in the computation of the Jacobian when the complete model is used versus when the linearized model is used. Coincidentally, λ also equals the contraction ratio of the TSA. For given error tolerances, Fig. 2.5(a) shows the achievable bending angle. Similarly, Fig. 2.5(b) shows the results of Eq. (2.19). In other words, Fig. 2.5 shows the region where the linear approximation of the generalized reduction ratio is within the given percentage tolerance. Our model predicts that the manipulator can achieve a bending angle of 61° while the linearized model remains within 10% tolerance. Although the linearized model's accuracy mostly decreases as the motor

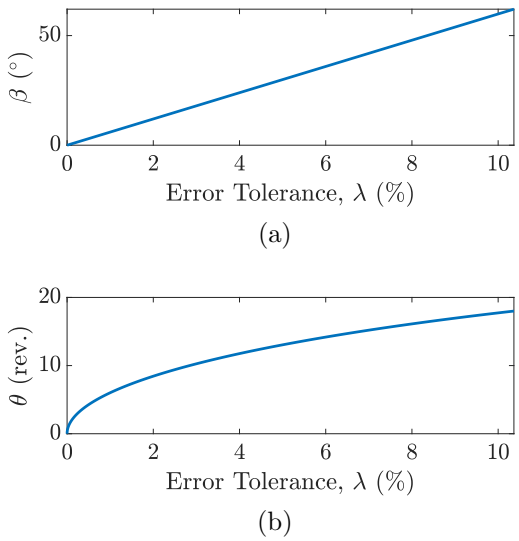

Figure 2.5: The achievable (a) bending angle and (b) motor angle that can be predicted using the linearized model with error tolerance λ. Note that the achievable motor angle is also implicitly a function of the string radius.

angle, bending angle, and bending velocity increase, the linearized model still provides an acceptable approximation of the manipulator's true bending velocity. Please note that the linearized reduction ratio is only utilized to estimate the manipulator's bending velocity and not any other states of the manipulator.

2.3.3 Multi-TSA kinematic Model

In this subsection, the bending angle, β, and bending direction, α, of the manipulator are derived as functions of the actuations of the three TSAs. Without loss of generality, the reference frame is placed such that TSA #1 intersects and is perpendicular to the positive y-axis, as shown in Fig. 2.6. In Figs. 2.6 and 2.7, $\mathbf{i}$, $\mathbf{j}$, and $\mathbf{k}$ are the unit vectors along the x, y, and z-axes, respectively. These unit vectors are fixed relative to the top of the soft manipulator. Since the TSAs are placed 120° apart from each other, TSAs #2 and #3 have an orientation of 30° ($\pi/6$ rad) between the negative

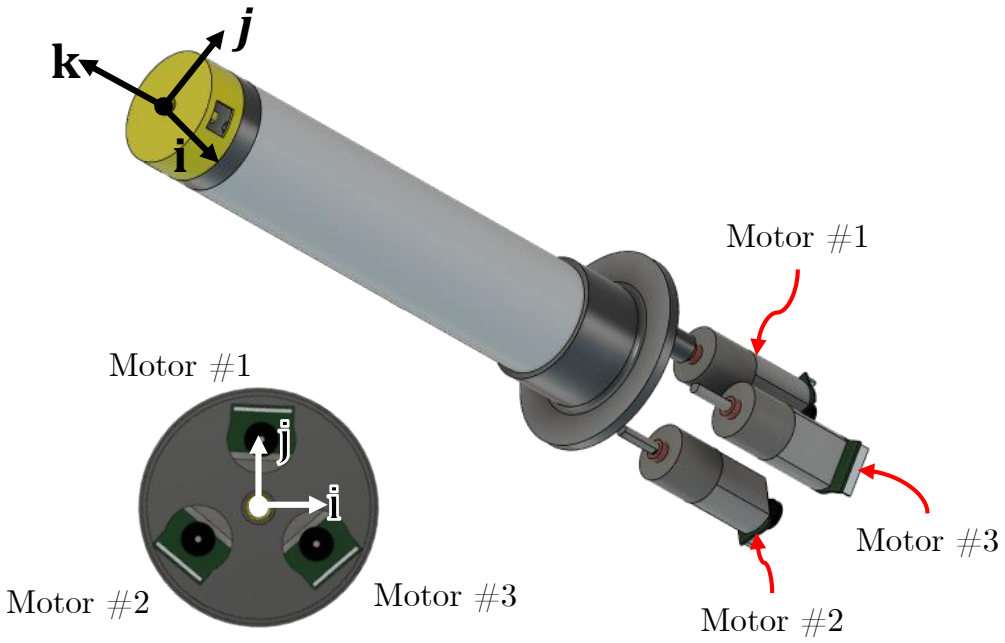

Figure 2.6: The placement of the motors within the robot with the labeled reference frame composed of the unit vectors **i**, **j**, and **k**.

and positive x-axis, respectively. All TSAs are parallel to the z-axis (**k** unit vector).

Since the three TSAs were placed evenly at angles 120° from each other near the circumference of the manipulator (details in Section 2.3), the contraction of each TSA will exert an axial force $\mathbf{F_{z,i}}$ at a distance $R_i = R$ from the center of the manipulator and induce a bending moment $\mathbf{M_i}$ on the manipulator, where $i = \{1, 2, 3\}$. $\mathbf{R_i}$ is a vector that has a magnitude of R. It is noted that for the purpose of this analysis, only the net force exerted by the TSA relative to the initial force exerted by the TSA is considered. As shown in Fig. 2.7(a), the direction of each **R** vector is determined by the placement of the TSA within the manipulator:

$$\begin{aligned} \mathbf{R_1} &= R\mathbf{j}, \\ \mathbf{R_2} &= R\left(-\cos\left(\frac{\pi}{6}\right)\mathbf{i} - \sin\left(\frac{\pi}{6}\right)\mathbf{j}\right) = R\left(-\frac{\sqrt{3}}{2}\mathbf{i} - \frac{1}{2}\mathbf{j}\right), \\ \mathbf{R_3} &= R\left(\cos\left(\frac{\pi}{6}\right)\mathbf{i} - \sin\left(\frac{\pi}{6}\right)\mathbf{j}\right) = R\left(\frac{\sqrt{3}}{2}\mathbf{i} - \frac{1}{2}\mathbf{j}\right). \end{aligned} \tag{2.22}$$

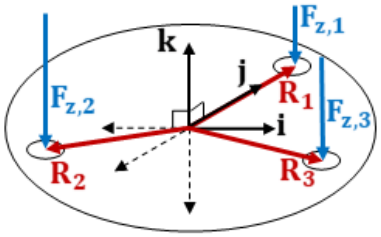

(a)

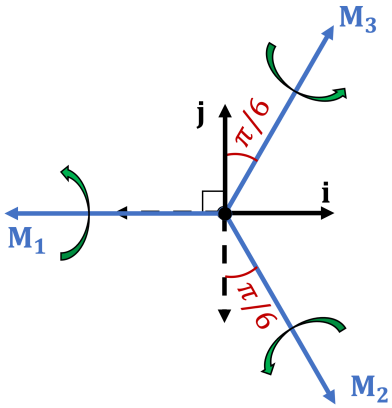

(b)

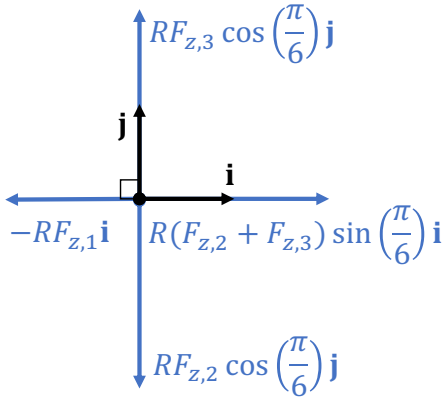

(c)

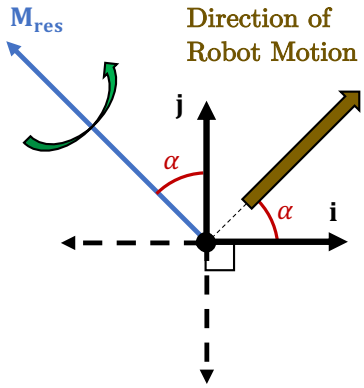

(d)

Figure 2.7: (a) The force vectors from the TSAs that induced a bending moment in the silicone. (b) The moments induced by each TSA and their rotation directions. (c) The moments distilled into their **i** and **j** components. (d) The resultant moment, $\mathbf{M}_{\text{res}}$, and the resulting bending direction of the robot. The bending direction is represented by the angle α, which is the angle between $\mathbf{M}_{\text{res}}$ and the unit vector **j**. α is also the angle between the direction of the robot's motion and the **i** unit vector.

The forces exerted by each TSA on the manipulator can be expressed as

$$\begin{aligned} \mathbf{F_{z,1}} &= -F_{z,1}\mathbf{k}, \\ \mathbf{F_{z,2}} &= -F_{z,2}\mathbf{k}, \\ \mathbf{F_{z,3}} &= -F_{z,3}\mathbf{k}, \end{aligned} \tag{2.23}$$

where the forces act in the direction of $-\mathbf{k}$ because the linear contractions of the strings exert a force to bend the manipulator. The moments (Fig. 2.7(b)) are

$$\begin{aligned} \mathbf{M_1} &= \mathbf{R_1} \times \mathbf{F_{z,1}} = -RF_{z,1}\mathbf{i}, \\ \mathbf{M_2} &= \mathbf{R_2} \times \mathbf{F_{z,2}} = RF_{z,2}\left(\frac{1}{2}\mathbf{i} - \frac{\sqrt{3}}{2}\mathbf{j}\right), \\ \mathbf{M_3} &= \mathbf{R_3} \times \mathbf{F_{z,3}} = RF_{z,3}\left(\frac{1}{2}\mathbf{i} + \frac{\sqrt{3}}{2}\mathbf{j}\right). \end{aligned} \tag{2.24}$$

The resultant bending moment $\mathbf{M}_{\text{res}}$ on the manipulator due to the actuations of the three TSAs can be expressed as follows:

$$\begin{aligned} \mathbf{M}_{\text{res}} = \mathbf{M_1} + \mathbf{M_2} + \mathbf{M_3} = &\frac{R}{2}((-2F_{z,1} + F_{z,2} + F_{z,3})\mathbf{i} \\ &+ (\sqrt{3}F_{z,3} - \sqrt{3}F_{z,2})\mathbf{j}). \end{aligned} \tag{2.25}$$

The $\mathbf{i}$ and $\mathbf{j}$ components of $\mathbf{M_{res}}$ are shown in Fig. 2.7(c). $\mathbf{M_{res}}$ can also be expressed as follows:

$$\mathbf{M}_{\text{res}} = \mathbf{R}_{\text{res}} \times \mathbf{F}_{\text{res}}, \tag{2.26}$$

where $\mathbf{R}_{\text{res}}$ is the resultant direction (Fig. 2.7(c)) perpendicular to which the resultant force $\mathbf{F}_{\text{res}}$ acts to apply moment $\mathbf{M}_{\text{res}}$ on the manipulator. $\mathbf{F}_{\text{res}}$ and $\mathbf{R}_{\text{res}}$ can be expressed as follows:

$$\begin{aligned} \mathbf{F_{res}} &= -F_{\text{res}}\mathbf{k}, \\ \mathbf{R_{res}} &= R(\cos\alpha\mathbf{i} + \sin\alpha\mathbf{j}), \end{aligned} \tag{2.27}$$

where α is the orientation of $\mathbf{R}_{\text{res}}$ with respect to the x-axis, as shown in Fig. 2.7(d). α is the bending direction of the manipulator. $\mathbf{M}_{\text{res}}$ can be expressed as follows:

$$\mathbf{M}_{\text{res}} = RF_{\text{res}}(-\sin\alpha\mathbf{i} + \cos\alpha\mathbf{j}), \tag{2.28}$$

where $\alpha \in [-2\pi, 2\pi]$. Comparing Eqs. (2.27) and (2.28) results in the following equations:

$$\begin{aligned} \sin\alpha &= \frac{F_{z,1} - \frac{1}{2}(F_{z,2} + F_{z,3})}{F_{\text{res}}}, \\ \cos\alpha &= \frac{\sqrt{3}(F_{z,3} - F_{z,2})}{2F_{\text{res}}}, \end{aligned} \tag{2.29}$$

where α can be derived as follows:

$$\alpha = \arctan\left(\frac{F_{z,1} - \frac{1}{2}(F_{z,2} + F_{z,3})}{\frac{\sqrt{3}}{2}(F_{z,3} - F_{z,2})}\right). \tag{2.30}$$

The magnitude of $\mathbf{F}_{\text{res}}$, acting perpendicular to $\mathbf{R}_{\text{res}}$ can be written as

$$F_{\text{res}} = \sqrt{\left(F_{z,1} - \frac{1}{2}(F_{z,2} + F_{z,3})\right)^2 + \frac{3}{4}(F_{z,3} - F_{z,2})^2}. \tag{2.31}$$

To derive the inverse kinematics of the manipulator, it is convenient to express Eqs. (2.30) and (2.31) in terms of the TSA contraction $C_i = L_0 - L_i$ with $i = \{1, 2, 3\}$. For this purpose, it is assumed that the force–TSA contraction correlation is linear, i.e. $F_{i,z} = aC_i$, where a is a constant. The correlation between C and F_z more closely resembles a higher-order polynomial with mild hysteresis. However, the linear approximation of F_z generates modest modeling errors, as will be shown in Section 2.4.

If $\dot{L} = 0$, the TSA cannot accelerate the robot. In that case, the forces produced by the TSAs are balanced by the reaction forces of the silicone body of the manipulator, making the manipulator's bending decay into static equilibrium. Using this correlation in Eqs. (2.30) and (2.31), the following relations are obtained:

$$\alpha = \arctan\left(\frac{C_1 - \frac{1}{2}(C_2 + C_3)}{\frac{\sqrt{3}}{2}(C_3 - C_2)}\right), \tag{2.32}$$

$$C_{\text{res}} = \pm\sqrt{(C_1 - \frac{1}{2}(C_2 + C_3))^2 + \frac{3}{4}(C_3 - C_2)^2}, \tag{2.33}$$

where C_{res} is the contraction of the resultant "virtual" TSA. Eqs. (2.32) and (2.33) imply that, in theory, the actuation of multiple TSAs can be represented by a single "virtual" TSA that applies the combined actuation of all three TSAs on the manipulator. Actuating all three TSAs at once will result in reduction of the center arc length of the manipulator, thereby directly contradicting assumption #2 in Section 2.3.2. Thus, this work will consider actuating no more than two TSAs simultaneously. Using Eq. (2.33), the resultant TSA length L_{res} can be computed as $L_{\text{res}} = L_0 - C_{\text{res}}$. Consequently, the bending angle β can be computed using Eq. (2.7) and the value of L_{res}.

2.3.4 TSA Dynamic Model

In this section, the dynamics of the TSAs used to drive the soft robotic manipulator are modeled. The purposes of the presented model were twofold: Firstly, the presented model was used to test the effects of linearizing $h(\theta)$ on the TSA dynamics. Secondly, the presented model was used to examine the effects of the assumption that the force exerted by the TSA on the silicone increases linearly with the TSA motor rotations, on the TSA dynamics. The following assumptions are considered for the derivation of the dynamic model (59):

1. The dynamics of the string are negligible when compared to the dynamics of the motor.
2. The string can only return to its original length if there is an external tensile force.
3. The electrodynamics of the motor are much faster than the mechanical dynamics.

The torques on the shaft of the motor are in equilibrium when

$$\Pi_m(t) = K_m I(t) = J_0\ddot{\theta}(t) + \nu\dot{\theta}(t) + \Pi_p(t) + \Pi_L(t), \tag{2.34}$$

where Π_m is the torque applied by the motor, $K_m > 0$ is the proportionality constant between the current draw of the motor and the motor's torque output, I is the current input to the motor, $J_0 > 0$ is the motor's polar moment of inertia, $\nu > 0$ is the viscous friction coefficient, Π_p is the opposing torque due to Coulombic friction (59), and Π_L is the torque produced by the strings. Π_L could either oppose or add to the torque output of the motor. When the strings are twisting, Π_L opposes Π_m, whereas when the strings are untwisting, Π_L supports Π_m. Π_L depends on both the applied axial force F_z and the inverse transmission ratio $h(\theta)$, where $\Pi_L(t) = h(\theta)F_z$. Due to the elasticity of the manipulator, the axial force F_z increases as θ and β increase (L decreases): $F_z = F_z(\theta) = a\theta$, where a is a constant. In addition, the opposing torque due to friction, Π_p, is assumed to be negligible, which is consistent with existing work on TSAs (59). Finally, the electrodynamics of the motor are considered much faster than the mechanical dynamics. Therefore, the current I to the motor can be approximated as proportional to the input control voltage V_c. The reduced-order model is then written as

$$\hat{K}_m V_c(t) = J_0\ddot{\theta}(t) + \nu\dot{\theta}(t) + h(\theta)F_z(\theta). \tag{2.35}$$

2.4 Control

2.4.1 Single TSA Control

To realize open-loop control, the necessary motor rotations must be computed for any desired bending angle β_d and bending direction α_d. For a single TSA case, the model

in Eq. (2.7) can be inverted to predict the required motor rotations θ_{req} corresponding to β_d. It is noted that α will be a constant. θ_{req} can be obtained such that

$$\theta_{\text{req}} = \pm \frac{\sqrt{L_0^2 - (X_0 + \delta + \beta R)^2}}{r}, \tag{2.36}$$

where $\theta_{\text{req}} = \theta_i$, for $i = \{1, 2, 3\}$. θ_{req} may be positive or negative because if a TSA starts with 0 twists, then either clockwise or counterclockwise twists will cause linear contraction. In this study, the convention is used that $\theta_{\text{req}} > 0$ is clockwise motor rotation, whereas $\theta_{\text{req}} < 0$ is counterclockwise rotation.

2.4.2 Multi-TSA Control

Multi-TSA open-loop control becomes more complicated. There are three actuators but only two desired angles, namely, the bending angle β_d and the bending direction α_d. This indicates that in theory, there could be infinitely many ways to twist the motor to realize the given β_d and α_d. The proposed control will only involve actuating one or two TSAs, considering its simplicity and the assumption of the derived Multi-TSA kinematic Model (more details in the last paragraph of Section 2.3.6).

The proposed control of multi-TSA manipulator consists of three steps. In step 1, θ_{res} is computed using Eq. (2.36). In step 2, two motors are selected to rotate according to α_d. The motors that rotate are selected based on the value of α_d. In this problem, $\alpha_d \in [-2\pi, 2\pi]$. Based on Fig. 2.7(a):

1. If $-\pi/6 < \alpha_d < \pi/2$, then only TSAs #1 and #3 actuate.
2. If $\pi/2 < \alpha_d < 7\pi/6$, then only TSAs #1 and #2 actuate.
3. If $7\pi/6 < \alpha_d < 11\pi/6$, then only TSAs #2 and #3 actuate.

4. If $\alpha_d = \pi/2$, then only TSA #1 actuates.

5. If $\alpha_d = 7\pi/6$, then only TSA #2 actuates.

6. If $\alpha_d = 11\pi/6$ or $\alpha_d = -\pi/6$, then only TSA #3 actuates.

These conditions are determined based on definitions and analysis in Fig. 2.6 and Fig. 2.7. In step 3, after selecting one or two TSAs that will actuate, Eqs. (2.32) and (2.33) will each become functions of two variables. For example, if TSA #1 does not actuate, then $C_1 = 0$ so that Eqs. (2.32) and (2.33) become functions of C_2 and C_3 only. With two unknown variables and two equations, C_2 and C_3 can then be derived analytically. Eqs. (2.37), (2.38), and (2.39) show the final solutions for C_1, and C_2, and C_3, respectively:

$$C_1 = \begin{cases} C_3 \sin(\pi/6) + C_{\text{res}} \sin\alpha_d, & \text{if} \quad -\pi/6 < \alpha_d < \pi/2 \\ C_{\text{res}}, & \text{if} \quad \alpha_d = \pi/2 \\ C_2 \sin(\pi/6) + C_{\text{res}} \sin\alpha_d, & \text{if} \quad \pi/2 < \alpha_d < 7\pi/6 \\ 0, & \text{if} \quad 7\pi/6 \le \alpha_d \le 11\pi/6, \end{cases} \tag{2.37}$$

$$C_2 = \begin{cases} 0, & \text{if} \quad -\pi/6 \le \alpha_d \le \pi/2 \\ -C_{\text{res}} \frac{\cos\alpha_d}{\cos(\pi/6)}, & \text{if} \quad \pi/2 < \alpha_d < 7\pi/6 \\ C_{\text{res}}, & \text{if} \quad \alpha_d = 7\pi/6 \\ -\frac{1}{2} C_{\text{res}} (\frac{\sin\alpha_d}{\sin(\pi/6)} + \frac{\cos\alpha_d}{\cos(\pi/6)}), & \text{if} \quad 7\pi/6 < \alpha_d < 11\pi/6, \end{cases} \tag{2.38}$$

$$C_3 = \begin{cases} C_{\text{res}} \frac{\cos(\alpha_d)}{\cos(\pi/6)}, & \text{if} \quad -\pi/6 < \alpha_d < \pi/2 \\ 0, & \text{if} \quad \pi/2 \le \alpha_d \le 7\pi/6 \\ (C_{\text{res}} \frac{\cos(\alpha_d)}{\cos(\pi/6)} + C_2), & \text{if} \quad 7\pi/6 < \alpha_d < 11\pi/6 \\ C_{\text{res}}, & \text{if} \quad \alpha_d = \{-\pi/6, 11\pi/6\}. \end{cases} \tag{2.39}$$

In Eqs (2.37)–(2.39), the limits of the piecewise functions equal the angles of the radius vectors $\mathbf{R_i}$. Although β_d does not explicitly appear in Eqs. (2.37)–(2.39), C_{res} is a function of β_d, so that Eqs. (2.37)–(2.39) depend on both β_d and α_d. In all cases, C_2 can be computed first, after which C_3 and finally C_1 can be computed. This ordering is due to the locations of the motors on the robot.

After solving for C_i, L_i and the desired motor angles θ_i are computed using the following equation.

$$\begin{aligned} L_i &= L_0 - C_i, \\ \theta_i &= \pm\frac{\sqrt{L_0^2 - L_i^2}}{r}. \end{aligned} \tag{2.40}$$

In the above equations, $i = \{1,2,3\}$. Then closed-loop control of the motors' input voltages were used to realize the desired motor angles. In this study, a proportional controller was used, although nearly any closed-loop strategy may work.

2.5 Experimental Results

2.5.1 Single TSA kinematic Model

Bending Angle

The model between motor angle θ and bending angle β was validated through experiments. For this purpose, the steady-state values of the motor rotations and the corresponding bending angles were utilized. This correlation was compared to the model in Eq. (2.7). Relevant model parameters are provided in Table 2.2. The parameters L_0, X_0, δ, R, and r_0 were experimentally measured. As seen from the results

Table 2.2: Model parameters of the TSA-driven soft robot.

Parameter	**Symbol**	**Value**	**Unit**
Initial string length	L_0	0.1884	m
Center arc length of the manipulator	X_0	0.165	m
Distance from the string-motor connecting point and the manipulator base	δ	0.023	m
Distance from X to X_0	R	1.625×10^{-2}	m
Initial TSA diameter	r_0	6.5×10^{-4}	m
Motor and hub inertia	J_0	3.9×10^{-4}	kg·m^2
Motor torque constant	$\hat{K}_m$	7.8×10^{-4}	N·m/V
Viscous damping coefficient	ν	1.2×10^{-2}	N·m·s

in Fig. 2.8(a), the experimental results agree well with the derived model. The error in the model was defined as

$$E_{y,k} = |y_{k,\text{exp}} - y_{k,\text{model}}|, \tag{2.41}$$

where $E_{y,k}$ is the error of the k^{th} point. $y_{k,\text{exp}}$ and $y_{k,\text{model}}$ are respectively the k^{th} point of experimentally obtained and modeled outputs of the system. The error between the experimental results and the model is presented in Fig. 2.8(b). The mean modeling error was found to be 1.82°, which was considered to be accurate since (1) the measurement error of the IMU itself was ±3.5° and (2) the range of bending angle was 60.4° during this experiment. More results and details can be found in (45).

To further test the validity of the assumptions made to formulate the proposed model, the results obtained from Eq. (2.7) were compared to those obtained from Eq. (2.9). As mentioned in Section 2.3.2, Eq. (2.9) was obtained by dropping Assumptions #2 and #4. The results, which are presented in Fig. 2.8(a)-(b) show that the proposed model performs better than the model presented in Eq. (2.9). The mean modeling error with Eq. (2.9) was found to be 12.35°, which was around seven times more than the error obtained by the proposed model. This indicates that the consideration of Assumptions #2 and #4 are valid.

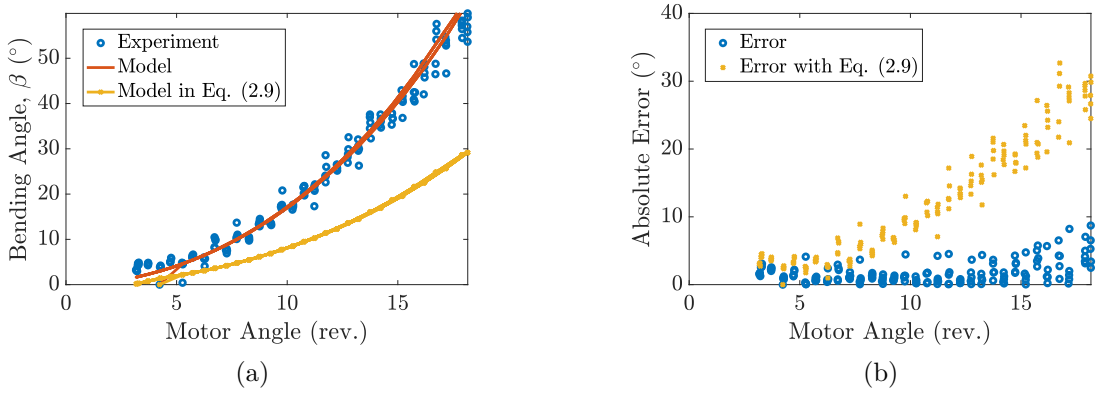

Figure 2.8: (a) The experimental and modeled results of β versus motor rotations θ. (b) The modeling error in β.

Axial Force

The correlation between TSA contraction $L_0 - L$ and axial force F_z was identified through experiments. This model was necessary to verify the multi-TSA model which assumed a linear correlation between the TSA contraction and the force output of the TSA. For this purpose, the steady-state values of the motor turns were measured and the corresponding TSA contraction were computed. The axial force was measured using force-sensitive resistors (FSR-404, Interlink Electronics). The sensors were placed at the attachment point of the strings with the manipulator such that when the strings are actuated, they exert force on the sensors. The location of the FSR sensors is shown in Fig. 2.9(a) The axial force was approximated as proportional to the TSA contraction such that $F_z = a(L_0 - L)$. Based on the experimental data the constant a_1 was identified as 884.91 N/m. This approximation simplified the multi-TSA model and enabled the straightforward derivation of the inverse model. Fig. 2.9(b) shows the identified model on top of the experimental results. The corresponding error is shown in Fig. 2.9(c), in which the average error was found to be 0.612 N. The modeling performance is reasonably well. By comparison, a fourth-order polynomial

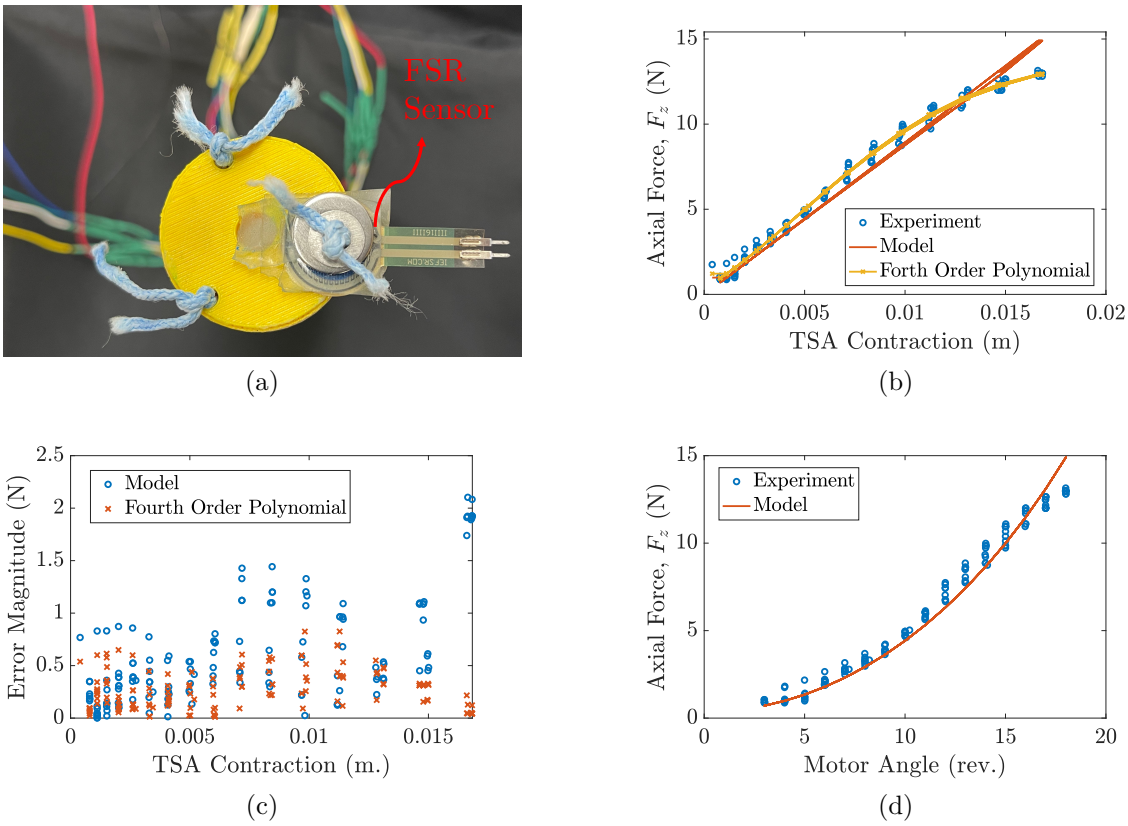

Figure 2.9: (a) The location of the FSR sensors. The way the FSR sensors are constrained with the strings can be seen. (b) The experimental and modeled results of F_z versus TSA contraction. (c) The modeling error in F_z. (f) The experimental and modeled results of F_z versus TSA motor rotations. (d) The modeling error in F_z versus TSA motor rotations.

modeled the correlation with a mean error of 0.325 N. While a modest improvement is obtained, inverting a fourth-order polynomial will be significantly more challenging. Another source of error was its mild hysteresis in the force–TSA contraction correlation (Fig. 2.9(b)), and accounting for hysteresis is beyond the scope of this work. Thus, considering the range of the axial force and the consequent simplicity of the inverse model, this mean error was deemed to be acceptable. The variation of F_z with motor rotations is shown in Fig. 2.9(d).

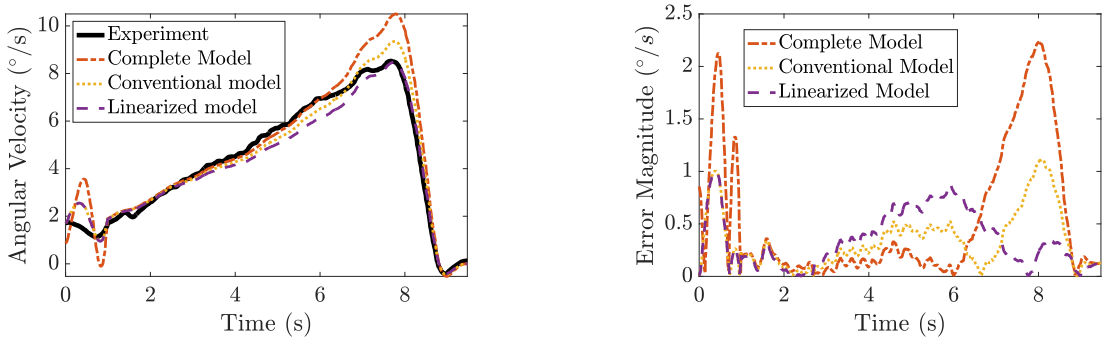

Figure 2.10: (a) The experimental results of the bending angular velocity $\dot{\beta}$ and modeled bending velocities versus time. (b) Modeling error in $\dot{\beta}$ for Eq. (2.10), Eq. (2.12) and Eq. (2.17).

Bending Velocity

The correlation between the angular velocity of the motor shaft $\dot{\theta}$ and the bending angular velocity $\dot{\beta}$ was validated through experiments. For this experiment, a step input voltage of 3.6 V was applied to the motor for 9 s, after which the input voltage immediately dropped to 0 V. During this period, the motor reached a steady-state velocity of 1.90 rev/s. A third-order Savitsky-Golay filter (50) with a window size of 151 samples taken at approximately 53.9 Hz differentiated θ to obtain $\dot{\theta}$, β to obtain $\dot{\beta}$, and r to obtain $\dot{r}$. A Savitsky-Golay filter was used to determine $\dot{r}$ instead of Eq. (2.11) because $\dot{r}$ was found sensitive to the measurements of r_0 and L. The Savitsky-Golay filter also smoothed the experimentally obtained β and θ as well as the analytic estimates of r. In particular, the filter was designed to reject the low-amplitude transient oscillations in θ.

To model the correlation between $\dot{\theta}$ and $\dot{\beta}$, three different models were tested using the parameters in Table 2.2, namely the "complete model", "conventional model", and "linearized model". The experimental data and modeling results for each strategy are

shown in Fig. 2.10(a)–(b). Interestingly, each modeling strategy produced similar amounts of error. All models performed reasonably well. For the complete model, the error was mostly below the mean error, 0.523°/s. The median error of the complete model was 0.187°/s. The conventional model error had a mean of 0.346°/s and median of 0.266°/s. The error of the linearized model model was 0.356°/s and its median error was 0.308°/s. It is noted that between [0,1] s, there is evident disagreement between the experimental results and the models. The complete model and conventional model also overestimate $\dot{\beta}$ at approximately 8 s. This overestimation may be due to the fact that the proposed models only consider the kinematics of the manipulator and not its dynamics which consist of inertia, restoring, and viscous damping forces. Consequently, the maximum frequency of $\dot{\beta}$ may be less than that of $\dot{\theta}$. The reduced bandwidth of $\dot{\beta}$ implies potentially decreased performance levels in high-speed control applications. Modeling the dynamic behavior of the manipulator is beyond the scope of this paper, and will be considered as a part of future work.

2.5.2 Multi-TSA kinematic Model

Two motors were actuated simultaneously to verify the multi-TSA model. An offset of three rotations was introduced to the two motors that spun to ensure their strings were taut and also to ensure that the third motor had a negligible effect on the actuation of the manipulator. A random sequence of desired motor rotations in the range of [3, 18] revolutions (revs) was generated to demonstrate the effectiveness of the proposed model. Using closed-loop proportional control, the motors were then driven to those setpoints. The corresponding bending angles (β) and bending directions (α) were recorded using the IMU.

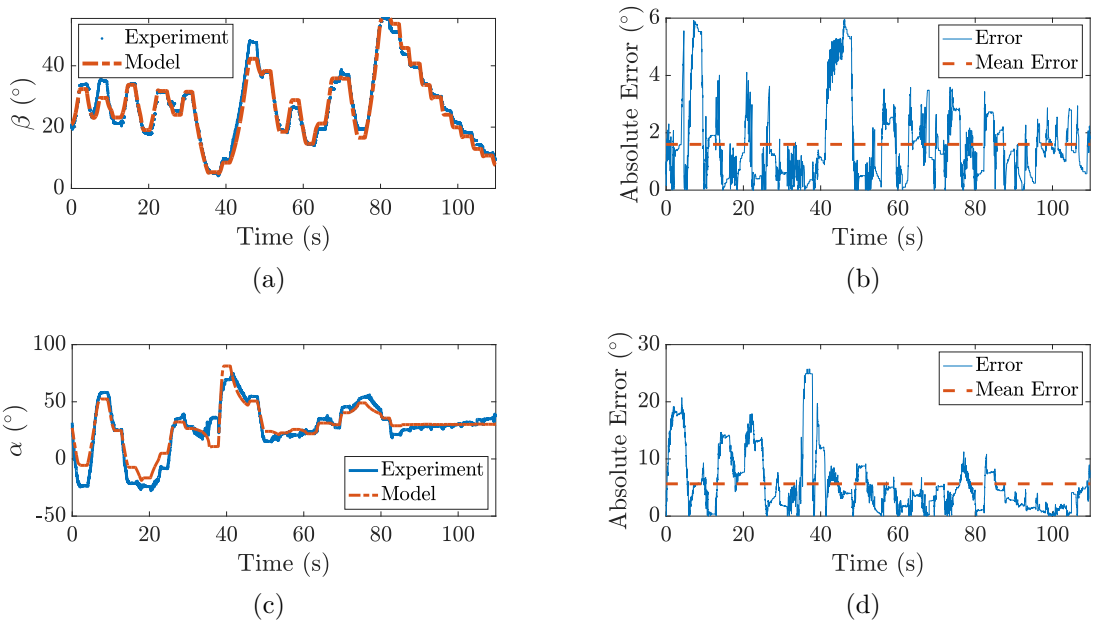

Figure 2.11: Multi-TSA modeling results using Motors #1 and #3. (a) The experimental and modeled bending angle β versus time. (b) The corresponding modeling error in β. (c) The experimental and modeled bending direction α versus time. (d) The corresponding modeling error in α.

The modeling results are presented in Fig. 2.11. The modeling results for β are shown in Fig. 2.11(a), with a mean error of 1.60° (Fig. 2.11(b)). Similarly, the modeling results for α are shown in Fig. 2.11(c) with a mean error of 4.65° (Fig. 2.11(d)). The errors in β and α were 3.11% and 4.53% of their respective ranges. Although the mean error in α was greater than the mean error in β, it was deemed to be acceptable considering the range of α during this experiment was $[-27.8°, 74.7°]$ (Fig. 2.7(a)), which was greater than the range of β. The range of β during this experiment was $[4.1°, 55.4°]$. Spikes in the errors in both α and β occurred at approximately 40 s. Assumption #4 in Section 2.3.2 is a possible source of error: the non-actuated TSA may have had mildly affected the bending angle and direction of the manipulator. The approximation that $F_z = a(L_0 - L)$, where a is a constant, may have introduced minor amounts of error in the computation of θ_{res}. In addition,

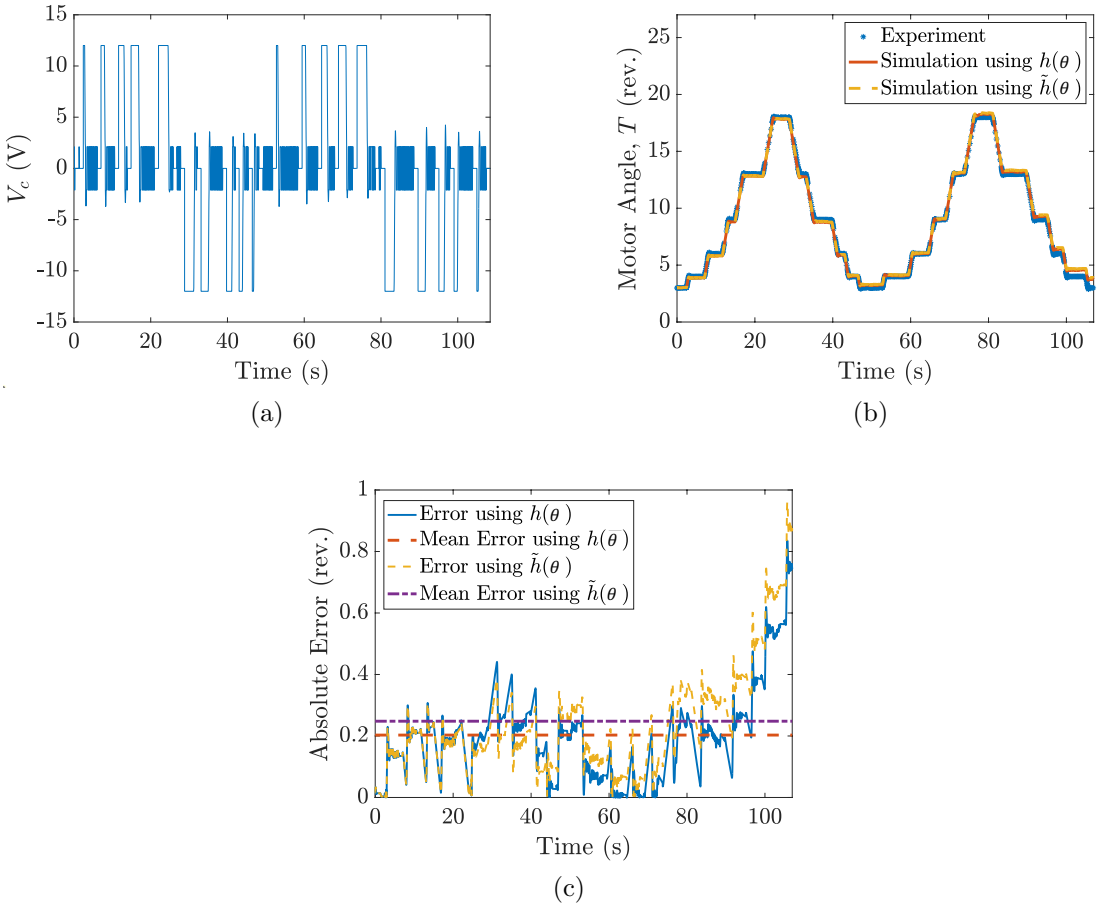

Figure 2.12: TSA dynamic model verification. (a) The input voltage to the motor that was applied during both the experiment and simulation. This voltage was a consequence of the closed-loop control of the motor during the experiment. (b) The experimentally obtained and simulated motor shaft angle under identical input voltages. (c) The error between the simulated and experimental values.

the hysteresis introduced into the behavior due to the usage of soft material could also be a potential source of error.

2.5.3 TSA Dynamic Model

The effectiveness of the dynamic model (Eq. (2.35)) was evaluated. Firstly, an experiment was conducted in which the motor was driven to setpoints of $[4, 6, 9, 13]$ revs

after initially being twisted 3 revs. The motor was controlled in a closed-loop manner with a proportional gain of $K_p = 0.27\,\mathrm{V/revolution}$ and a sampling period of 40 ms. Secondly, the system was simulated in SIMULINK using the same voltage input sequence that was applied during the experiment (Fig. 2.12(a)). During simulation, both the models with the complete reduction ratio (Eq. (2.10)) and the linearized reduction ratio ($\tilde{h}(\theta)$ from Eq. (2.16)) were tested. F_z was included in the simulation using the corresponding identified model. Parameters from Table 2.2 were utilized. The motor parameters were obtained from the datasheet provided by the manufacturer. As shown in Fig. 2.12(b), the experimentally obtained and simulated motor angles were very close.

The error, $|\theta - \theta_{\mathrm{sim}}|$ is quantified in Fig. 2.12(c), where the mean error is 0.203 revs (1.35% of the range of θ) using the complete reduction ratio $h(\theta)$ and 0.248 revs (1.65% of the range of θ) using the linearized reduction ratio $\tilde{h}(\theta)$. These errors were acceptable considering the motor angle had a range of 15 revs during the experiment. The errors in Fig. 2.12(c), for both the models with linearized and non-linearized reduction ratios, steeply increased at approximately 80 s into the simulation. This behavior is likely due to a slight under-estimation of Π_L. The effect of Π_L is that when $\dot{L} < 0$, Π_L resists the torque induced by the input voltage. In contrast, when $\dot{L} > 0$, Π_L adds to the torque induced by the input voltage. As shown in Fig. 2.12(b), the motor angle on the last descending cycle is greater in the simulation than in the experiment. This means that the coupling torque Π_L during the experiment was slightly larger than the simulated Π_L. Additional friction and hysteresis in the motor torque may have also led to the deviation between the experimental and simulated values ([65]). The accuracy of the models also confirmed that the assumption that F_z varied linearly with $L_0 - L$, did not have a significant effect on the TSA dynamics.

2.5.4 Open-Loop Control

To validate the inverse model, open-loop control of the manipulator using two motors was conducted. Similar to the multi-TSA model validation, random sequences of desired bending angles β_d and bending directions α_d were generated, where $\beta_d \in [0, \pi/3]$ and $\alpha_d \in [-\pi/6, \pi/2]$. Although our model is valid for $0 \leq \beta \leq \pi/2$, β_d was chosen to be $\leq \pi/3$ during this experiment to ensure the bending angle was within a safe operating range. The sampling period for this experiment was 8 ms. The corresponding rotations of Motor #1 and Motor #3 were computed using Eqs. (2.37) and (2.39). The open-loop control results are presented in Fig. 2.13. By replacing y_{model} with y_{des}, Eq. (2.41) was also utilized to evaluate the control error magnitude, where y_{des} is the desired output of the system. The mean control errors in β and α were 2.21° (3.68% of the range of β) and 5.15° (4.52% of the range of α), respectively. These error values were considered to be acceptable because they were similar to the modeling errors in Section 2.4.2. Similar to the multi-TSA model validation, the results can be generalized to three TSAs since for any α_d, only two TSAs need to rotate simultaneously. The particular TSAs that rotate could change if α_d changes.

2.6 Discussions

Within the testing range of β which was [0 60]°, the proposed models and control strategies performed satisfactorily. However, it is noted that both the modeling and control strategies were developed based on several assumptions. The models may not be valid when these assumptions fail. For example, for the case of the bending angle model losing accuracy at higher motor rotations, the failure of assumption #4 could

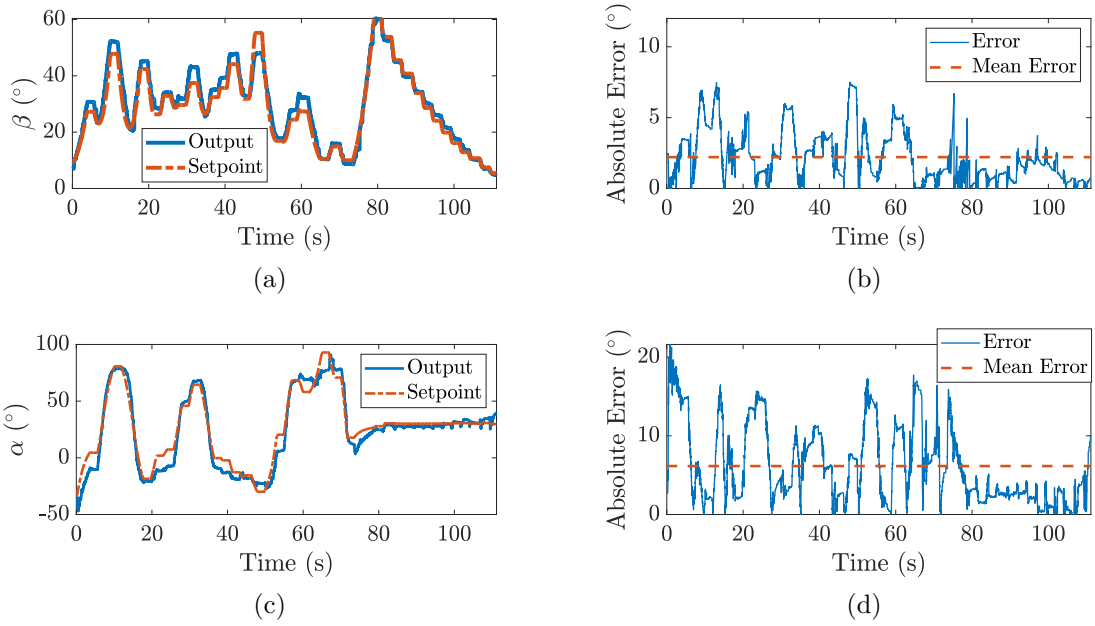

Figure 2.13: Open-loop control results using Motors #1 and #3. (a) The bending angle results and (b) error. (c) The bending direction results and (d) error. The means errors were 2.21°and 6.15°for β and α, respectively.

be a possible cause. It was expected that the untwisted TSAs would receive some tension due to the twisting of the other TSAs after certain actuation range. This could potentially cause the bending angle to increase with a slower rate relative to the proposed model. This could be verified from the experimental results presented in Fig. 2.8(a)–(b) where the proposed model overestimates the bending angle at higher motor rotations. However, assumption #4 was reasonable within the tested range of motion, because it did not significantly impact the model's accuracy in estimating the angular position of the manipulator. This was verified through comparing the results of the proposed model with a model where Assumption #4 was dropped. In future work, the validity of assumption #4 will be analyzed in more detail by studying the dynamics of the manipulator which would consider all the forces acting on it. Assumption #2 in Section 2.3.2 and the constraint of actuating one or two TSAs in Section 2.3.3 and Section 2.3.6 resulted in relatively large modeling and

control accuracy with low complexity strategies. Relaxing assumption #2 and the aforementioned constraint would result in the manipulator's central arc length, X_0, to be a function of the forces exerted by the three TSAs. This phenomenon will be considered as a part of developing a dynamic model for the manipulator in future work.

Similarly, the TSAs were placed within the manipulator through channels present along the length of the manipulators and assumption #6 was applied. However, previous studies analyzed the frictional effects of TSAs due to the sliding of the strings along surfaces (51) or placement in conduit tubes (52). Experimental characterization was conducted on the resulting non-uniform twist propagation and contraction of TSAs due to the frictional effects. The correlations between bending angle and motor angle presented in Fig. 2.8(a) were fairly consistent with the proposed model. This indicated that the propagation of the twists inside the silicone was mostly uniform within the tested range of actuation. More accurate physics inferred data-driven models, such as the ones presented in (64) may be used in future work. The relationship between bending angle and axial force presented in Fig. 2.2(c) showed hysteresis. The friction inside the silicone may be a contributor to the hysteresis, as indicated by previous studies (51; 52). The presented models were derived considering the use of three TSAs. More TSAs can be included in the design of the manipulator to increase the controllable DOFs. For such modifications, the models and control strategies must be derived considering the placement of the TSAs in the manipulator. The process of deriving the modeling and control strategies for such modifications can be based on the processes presented in this chapter. However the presented models and control strategies in this chapter cannot be directly scaled for such modifications.

2.7 Limitations of TSA-driven Soft Robots

2.7.1 Nonlinear Behavior

The motor angle – bending angle correlations of the soft robotic manipulator (Fig. 2.2(b)–(c)) were nonlinear. The nonlinearities consisted of hysteresis. Besides soft robots, most artificial muscles exhibit hysteresis nonlinearity ([66]; [67]; [68]; [69]; [70]). With hysteresis, the output of an actuator depends not only on current input, but also on the input history, even under quasi-static conditions ([71]; [72]). To capture hysteresis, both physics-based methods ([73]) and phenomenology-based approaches, such as the Preisach operator, Prandtl-Ishlinskii model, and Bouc-Wen model ([70]; [74]; [75]; [76]; [77]), have been proposed. Different control schemes like feedforward control, proportional–integral–derivative control, and robust and adaptive control have been realized ([68]; [78]; [79]; [80]; [81]; [82]). However, the existing modeling and control studies have not considered another nonlinear behavior that appeared in both the soft robots presented in this dissertation and also commonly appeared in artificial muscles – under quasi-static input sequences, the first input-output cycle is often inconsistent with subsequent cycles that are repeatable and exhibit hysteresis. This first cycle is termed as "lonely stroke" ([83]). To practically employ artificial muscles and soft robots, it is often crucial to reliably and accurately characterize, model, and control their behavior. Despite significant progress, it still remains a challenge to accurately characterize the nonlinear properties of artificial muscles due to their inherent material properties, such as hysteresis, creep, and vibrations ([83]). Although all the robots exhibited acceptable consistency in their respective motor input–output correlations, the presence of the aforementioned nonlinearities could complicate the physics-based modeling process. Utilizing an extended Preisach operator ([83]; [84]) to capture the

aforementioned nonlinearities could be a viable option. This topic is presented in detail in Chapter 3.

2.7.2 Change of TSA Parameters Over Time

Previous studies have presented highly accurate TSA models by considering different phenomena such as varying radius of the strings along the range of actuation, friction in different parts of the system, and finite string stiffness ([49]; [27]; [65]). However, limited studies have been conducted on TSAs considering time-varying properties. While existing modeling and control strategies show strong promise ([49]; [31]; [59]), they exhibit a few limitations. Firstly, the external force applied to the TSAs is assumed to be measurable or predictable. Secondly, it is assumed that all the system parameters are accurately known. Existing studies do not consider the effects of wear and tear and long term usage on the system parameters. However, in practical scenarios these assumptions may not be valid, especially during long-term operation of TSA-driven systems. For example, in most robotic and mechatronic applications, the external force can be complex, highly dynamic, and difficult to predict or measure. In addition, the system parameters such as the string stiffnesses could change over time due to general wear and tear, creep, and when used over long durations of time ([85]). Furthermore, TSAs have also shown load-dependent hysteretic behavior ([40]; [27]). These behaviors could be difficult to predict accurately. Similarly, while most motor parameters can be obtained from the data provided by the manufacturer, in inexpensive motors, the effect of wear and tear might not be negligible when used in practical applications ([86]). Under such circumstances, control strategies that employ adaptive laws to estimate system or control parameters could be highly suitable. To address these issues parameter estimation and adaptive control strategies for TSAs

will be discussed in Chapter 4.

2.7.3 Limited Output Contraction

While TSAs have many advantageous properties, one major limitation of TSAs is the limited contraction which they produce – TSAs exhibit an output contraction of around 30% of their initial untwisted length. Consequently, TSAs lack in the area of compactness due to the limited contraction. To circumvent the issue of compactness, the TSA strings were embedded inside the silicone of the soft manipulator. Doing so resulted in the interaction of the twisted strings with the internal walls of the silicone. While this phenomenon did not cause major issues in terms of performance of the modeling and control strategies within the tested ranges of actuation, it could have a non-negligible effect in the ranges of actuation which go beyond the tested range of actuation since interaction with silicone could result in non-uniform propagation of twists across the twisted strings ([52]). To avoid the interaction of the strings with the silicone, in ([43]), the twisting of the strings was restricted to be outside of the silicone structure by employing a constant twisting zone strategy. While this did not have adverse affects on the performance of the gripper presented in ([43]), the overall size of the gripper increased due to the employment of a constant twisting zone. Therefore, to avoid the aforementioned issues in future application of TSAs which demand compact actuation solutions, the overall actuation range of the TSAs need to be increased. Overtwisting and coiling the strings beyond the normal twisting range could be a viable option to address this issue. This will be evaluated in chapter 5.

CHAPTER 3

MODELING AND INVERSE COMPENSATION OF HYSTERESIS WITH LONELY STROKE

In this chapter, we present the study to model and compensate for the hysteresis with lonely stroke property which appeared in the proposed soft robots and also has been reported in popular artificial muscles. A modeling approach is developed through the expansion of the input range of a Preisach operator to physically infeasible region. The expansion of the Preisach operator results in additional model parameters. The effects of such expansion on model accuracy and computational cost are studied. Lastly, an iterative algorithm is developed to compensate for the hysteresis with lonely stroke by approximately inverting the proposed model. The effectiveness of the proposed scheme is validated by comprehensive simulation and experimental results. The contents of this chapter are based on the findings presented in (83; 94; 84).

3.1 Motivation

The input–output correlation of a robotic finger as part of the TSA-driven anthropomorphic soft robotic gripper (43), presented in Fig. 3.1, shows the hysteresis with lonely stroke behavior. This type of behavior was also found in the input–output correlation of the TSA-driven soft robotic manipulator presented in Chapter 2 (Fig. 2.2(b)–(c)). In addition to soft and compliant structures (87; 88), the hysteresis with lonely stroke behavior has been observed in a number of popular artificial muscles and materials, such as pneumatic actuators (66; 89), McKibben actuators (67), silicon elastomers (90), SMAs (91; 92), and SMPs (93). However, no studies have conducted systematic characterization, modeling, and compensation of the hysteresis with lonely stroke behavior. Our recent study found that the lonely stroke not only affected the

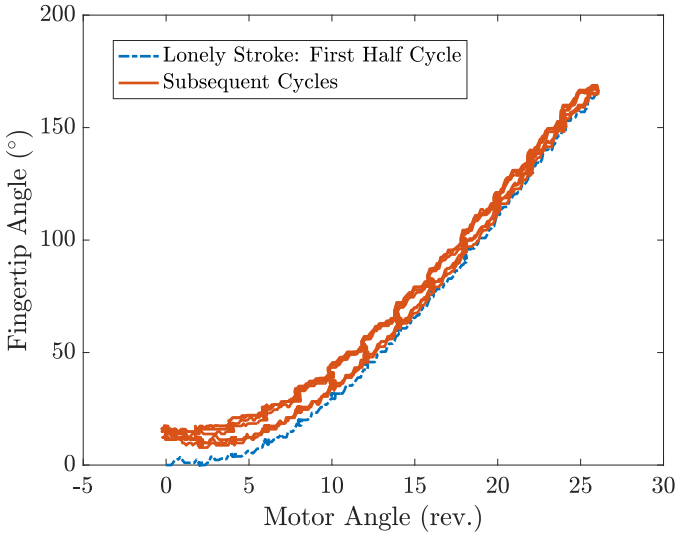

Figure 3.1: Illustration of the hysteresis with lonely stroke behavior in the input–output correlation of a soft robotic finger which was part of the TSA-driven anthropomorphic soft robotic gripper.

behavior of SCP actuators, but also presented coupling with the subsequent repeatable hysteresis cycles (94). A preliminary study (87) showed that the neural network model was capable of capturing the hysteresis with lonely stroke behavior. However, the coupling between the repeatable hysteresis and lonely stroke was not specifically studied. As pointed out over three decades ago, neural networks have been proven by many researchers as universal approximators of any continuous function with arbitrarily desired accuracy, at the cost of computational cost (95; 96). Therefore, while the proposed method in (87) worked, its computational cost was high with relatively low modeling accuracy. In addition, the model was not specifically designed for hysteresis with lonely stroke behaviors. From a physics point of view, hysteresis with lonely stroke is likely caused by the material-induced nonlinear properties and residual stress (91; 97). Due to residual stress, the output of the lonely stroke may be a summation of the input-induced output and the residual stress-induced output.

Although existing nonlinear models of soft robots and artificial muscles have shown

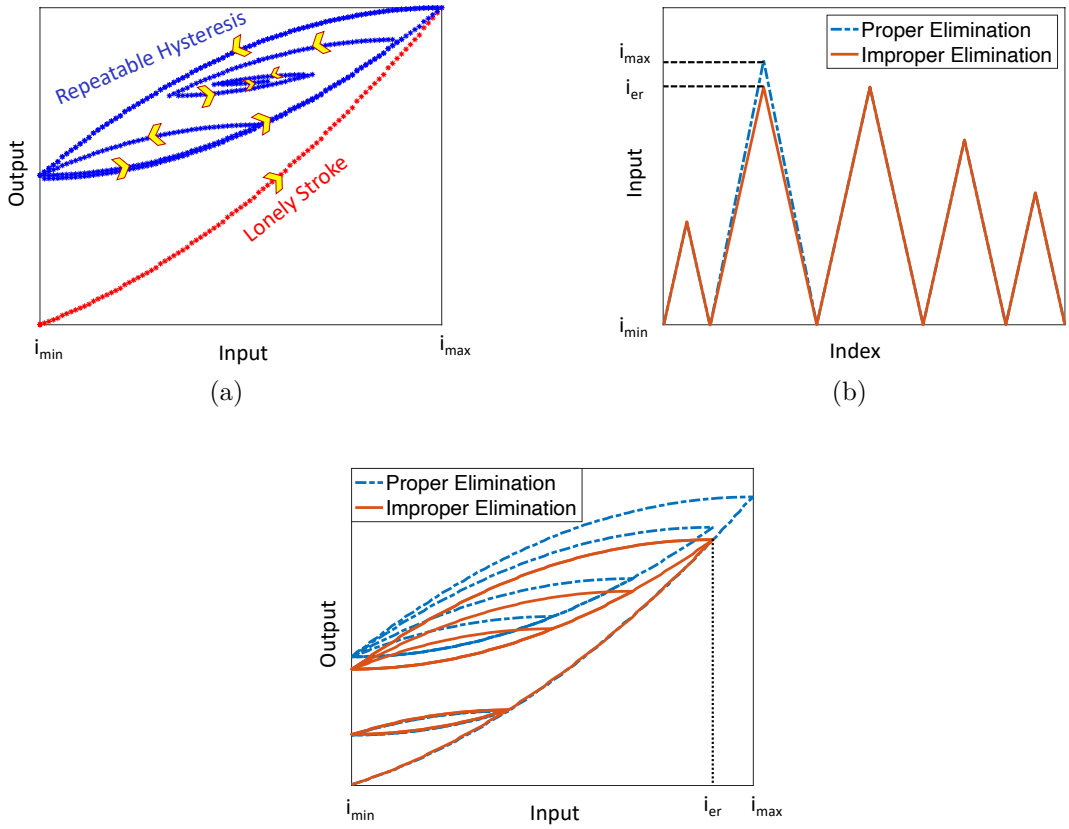

Figure 3.2: (a) Illustration of the hysteresis with lonely stroke behavior. (b) Two input sequences which enable proper elimination and improper elimination of the lonely stroke, respectively. Only one cycle is different. (c) Input-output correlations with proper elimination and improper elimination of the lonely stroke. Note the output with improper lonely stroke elimination exhibits large discrepancies in all cycles.

promising results, these studies exclusively considered the subsequent repeatable hysteresis but neglected the lonely stroke (69). Through elimination of the lonely stroke, hysteretic systems which exhibit lonely stroke may operate in the repeatable region, however, such elimination would require accurate input sequences under specific conditions: start from the minimal input, monotonically increase to the maximum input, then monotonically decrease to the minimum input (Fig. 3.2(a)-(b)). Such elimination procedure might be undesirable or even infeasible due to the following reasons:

Firstly, small errors of the input may result in imperfect elimination and unpredictable behaviors. For example, as illustrated in Fig. 3.2(b)-(c), when the input with a small error in one cycle, i_{er}, is applied to eliminate lonely stroke, all of the repetitive hysteresis cycles consistently exhibit errors with complex patterns, regardless of the history or magnitude of the remaining input sequence. This stringent condition of lonely stroke elimination makes it difficult to predict the behavior of such hysteretic systems, posing additional challenges on precise control of hysteretic systems which exhibit lonely stroke even if the lonely stroke is to be eliminated intentionally. Secondly, using specialized input sequence to eliminate the lonely stroke may be practically infeasible in cases where the external conditions change frequently during normal operation. For example, in an SCP actuator-driven robotic bicep ([69]), when the tension force of the SCP actuator changes to different values continuously during the bicep flexion and extension operation, the lonely stroke will appear between temperature and strain in every cycle. However, specialized input sequence has to be applied whenever the load is changed, which would make it practically infeasible to eliminate the lonely stroke. Thirdly, applying the specialized input sequence to eliminate the lonely stroke may be time-consuming in cases where artificial muscles exhibit slow system dynamics – hysteresis with lonely stroke is a quasi-static nonlinearity and steady-state values need to be obtained. For example, under a step voltage input, SMA and SCP actuators may take 10-30 seconds to reach steady-state temperature ([94]; [69]; [9]). This issue may pose challenges to facilitate wider adoption of artificial muscle-powered intelligent systems where time efficiency is important. Lastly, the exclusion of lonely stroke may significantly decrease the output range of hysteretic systems which exhibit lonely stroke. For example, if the lonely stroke in the stress-strain relationship of an SMP actuator is not considered, the maximum strain output of the actuator would decrease from 100% to around 40% ([93]).

It is desirable but difficult to develop accurate models considering the hysteresis with lonely stroke behavior. Without effective models and compensation schemes, large discrepancies may appear ([90; 91]), especially considering artificial muscle-powered robots, where non-repetitive tasks in unstructured and uncertain environments are often expected ([9]). The outputs of existing hysteresis models, such as the Preisach operator, are fixed and not history-dependent at the minimum and maximum inputs ([71]). However, due to lonely stroke, the output at the minimum input depends on current input and the input history. As illustrated in Fig. 3.2(c), the output of the system may vary significantly at the minimal input, $i_{\min}$. This indicates that conventional hysteresis models would fail to capture the hysteresis with lonely stroke behavior. Another possible approach is to employ a separate model (e.g., a high-order polynomial) to capture the lonely stroke, while using an existing hysteresis model for describing the repeatable hysteresis cycles. However, this approach fails to capture the coupling of the lonely stroke and the repeatable hysteresis cycles. Due to coupling, the input-output hysteresis cycles may vary greatly depending on the magnitude of lonely stroke and the input history, as illustrated in Fig. 3.2(c).

3.2 Review of the Preisach Operator

The Preisach operator, as one of the most popular hysteresis models, has been extensively used in artificial muscles and many other areas ([72; 98; 76; 77]), and is thus adopted in this study. The Preisach operator can be expressed as a weighted integration of delayed relays, called *hysterons*. The output of the hysteron, $\gamma_{\beta,\alpha}$, is written

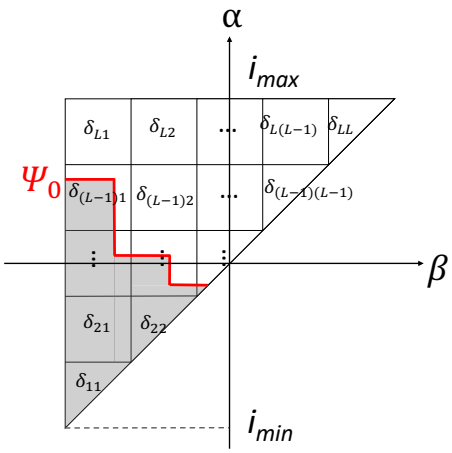

Figure 3.3: Discretization of the Preisach density function.

as

$$\gamma_{\beta,\alpha}[i(\cdot);\zeta_0(\beta,\alpha)] = \begin{cases} +1 & \text{if } i > \alpha \\ -1 & \text{if } i < \beta \\ \zeta_0(\beta,\alpha) & \text{if } \beta \le i \le \alpha \end{cases}, \tag{3.1}$$

where α and β are two thresholds, $\alpha \ge \beta$, $i(\cdot)$ denotes the input, $i_{\min}$ and $i_{\max}$ are the minimum and maximum inputs, respectively, and $\zeta_0(\beta,\alpha) \in \{-1,1\}$ is the initial condition of the hysteron. Through integration of all weighted hysterons with different α and β values, the output of a Preisach operator, Γ, is expressed as

$$o(t) = \Gamma[i(\cdot);\zeta_0](t) = \int_{\mathcal{P}_0} \delta(\beta,\alpha)\gamma_{\beta,\alpha}[i(\cdot);\zeta_0(\beta,\alpha)](t)\mathrm{d}\beta\,\mathrm{d}\alpha, \tag{3.2}$$

where t is time, $\delta(\beta,\alpha)$ is the density function, and $\mathcal{P}_0 = \{(\beta,\alpha) : i_{\min} \le \beta \le \alpha \le i_{\max}\}$ is the *Preisach plane* that defines the region of integration.

For efficient model implementation, the following discretization procedure is employed: the density function, $\delta(\beta,\alpha)$, is discretized into a piecewise constant function – the density value is constant within each lattice cell but varies from cell to cell (99). Fig. 3.3 shows an example of the discretization of the density function into $\frac{L(L+1)}{2}$ cells, where L is the discretization level. Each cell (i,j) is associated with a constant density value, δ_{ij}, where i and j represent the row and column indices, respectively.

With this discretization scheme, the model output at time n is

$$o[n] = \Gamma[i(\cdot); \psi_0][n] = o_c + \sum_{i=1}^{L} \sum_{j=1}^{i} \delta_{ij} s_{ij}[n], \tag{3.3}$$

where o_c is a constant bias, $s_{ij}[n]$ is the *signed* area of the cell (i, j), namely, its area occupied by hysterons with output $+1$ minus that occupied by hysterons with output -1. The boundary of the two regions is the memory curve, which is determined by the input history. As an example, the memory curve shown in Fig. 3.3 is denoted as ψ_0. The outputs of the hysterons below the memory curve in the shaded area are $+1$ and the remaining are -1. When all the densities $\{\delta_{ij}\}$ are greater than or equal to zero, the hysteresis relationship is monotonically increasing; When all the densities $\{\delta_{ij}\}$ are less than or equal to zero, the hysteresis is monotonically decreasing. Efficient model identification for the constant bias, o_c, and the densities, $\{\delta_{ij}\}$, can be realized using least squares method ([72]). Readers are referred to ([100]; [72]) for more details about the Preisach operator.

Proposition 1 *Given a Preisach operator with known density function* $\{\delta_{ij}\}$*, its outputs are fixed and not history-dependent at the minimum and maximum inputs.*

Remark 1 *At* $i_{\min}$ *and* $i_{\max}$*, the outputs of hysterons of all cells on the Preisach plane are* -1 *and* $+1$*, respectively, irrespective of the input history. Thus, the outputs of the Preisach operator at* $i_{\min}$ *and* $i_{\max}$ *are:*

$$\begin{aligned} o(i_{\min}) &= o_c - l^2 \sum_{i=2}^{L} \sum_{j=1}^{i-1} \delta_{ij} - \frac{l^2}{2} \sum_{i=1}^{L} \delta_{ii}, \\ o(i_{\max}) &= o_c + l^2 \sum_{i=2}^{L} \sum_{j=1}^{i-1} \delta_{ij} + \frac{l^2}{2} \sum_{i=1}^{L} \delta_{ii}, \end{aligned} \tag{3.4}$$

respectively, where l *is the edge length of a cell in the Preisach plane expressed as* $l = \frac{i_{\max} - i_{\min}}{L}$*. All cells are squares with the area of* l^2*, except the ones that intercept*

with the $\alpha = \beta$ line, namely the cells associated with densities $\{\delta_{ii}: i = 1, 2, \cdots, L\}$, which are 45°–45°–90° triangles with the area of $\frac{l^2}{2}$. Note uniform discretization of the Preisach density function is assumed. Non-uniform discretization of Preisach operator has been explored in (101) and is beyond the scope of this study.

3.3 Proposed Approach

3.3.1 Model

As discussed, the conventional Preisach operator fails to capture the hysteresis with lonely stroke behavior due to the complex coupling between the lonely stroke and the repeatable cycles, as well as the possible variability of output at $i_{\min}$. To capture the hysteresis with lonely stroke behavior, the *expanded Preisach operator* is proposed by constructing the Preisach plane within the range of i_{ext} and $i_{\max}$, with $i_{\text{ext}} < i_{\min}$, as illustrated in Fig. 3.4(c). This is realized by expanding the minimum input of the Preisach operator from $i_{\min}$ to i_{ext} and assigning densities to the expanded region on the Preisach plane. Note that the actual applied input will never go below $i_{\min}$. Due to the expansion of the input range to i_{ext} and the inclusion of densities $\{\rho_{ij}\}$, the output value of the proposed model at $i_{\min}$ will be dependent on input and the input history.

As shown in Fig. 3.4(c), assume the number of expanded columns to the density function of the proposed expanded Preisach operator is m, then the level of discretization for the repeatable cycles, L_0, can be expressed as $L_0 = L - m$, where L is the total discretization level of the model. Given $i_{\min}$, $i_{\max}$, and L, the relationship between

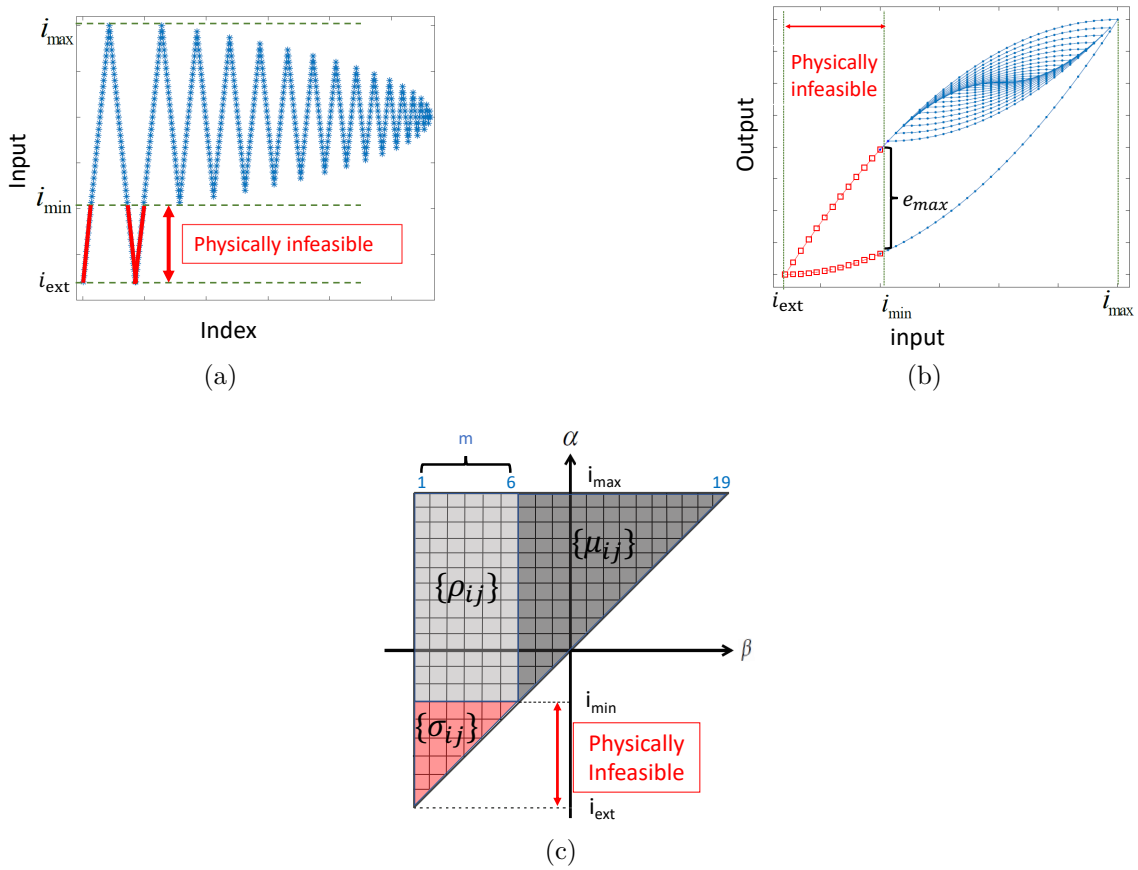

Figure 3.4: (a) An input sequence with an expanded range. (b) The input-output relationship of the proposed expanded Preisach operator under input sequence in (a). (c) The expanded Preisach density function, where m additional columns of densities are added.

i_{ext} and m can be expressed as

$$i_{\text{ext}} = i_{\min} - m\frac{i_{\max} - i_{\min}}{L - m} = i_{\min} - l_e m, \tag{3.5}$$

where l_e is the edge length of a cell in the expanded Preisach plane expressed as $l_e = \frac{i_{\max} - i_{\min}}{L-m} = \frac{i_{\max} - i_{\text{ext}}}{L}$. The output of the proposed model, Λ, can be written as

$$\begin{aligned} u[n] = \Lambda[i(\cdot);\psi_0][n] = \sum_{i=1}^{m}\sum_{j=1}^{i}\sigma_{ij}s_{ij}[n] + \sum_{i=m+1}^{L}\sum_{j=1}^{m}\rho_{ij}s_{ij}[n] \\ + \sum_{i=m+1}^{L}\sum_{j=m+1}^{i}\mu_{ij}s_{ij}[n], \end{aligned} \tag{3.6}$$

The hysterons in the three regions of the *expanded* Preisach density function, namely, $\{\sigma_{ij}\}$, $\{\rho_{ij}\}$, and $\{\mu_{ij}\}$, collectively contribute to the output of the proposed model. The densities of the expanded columns, $\{\sigma_{ij}\}$ and $\{\rho_{ij}\}$, together, are responsible for capturing the lonely stroke and the coupling between the repeatable hysteresis and the lonely stroke. The densities $\{\mu_{ij}\}$ are responsible for describing the repeatable hysteresis cycles. With the proposed approach, the system always starts with the outputs of all hysterons associated with densities $\{\sigma_{ij}\}$ being $+1$ – this is due to the fact that at any physically feasible input $i \geq i_{\min}$, the memory curve will always be above all cells associated with densities $\{\sigma_{ij}\}$. This has two implications: Firstly, unlike the conventional Preisach operator (Eq. (3.3)), no additional constant bias term is required for the proposed model (Eq. (3.6)). The contribution of all hysterons associated with densities $\{\sigma_{ij}\}$ to the model output is equivalent to a constant bias. Secondly, all densities $\{\sigma_{ij}\}$ can have the same value without compromising the modeling performance. This is because all hysterons associated with densities $\{\sigma_{ij}\}$ are always $+1$, and all densities $\{\sigma_{ij}\}$ will be considered as a whole to affect output (Eq. (3.6)).

Note that the number of the expanded columns to the density function of the proposed model, m, is assumed to be a positive integer in this study with the following considerations: When m is selected to be an integer, the density function of the expanded Preisach plane is systematically divided into three regions with density sets $\{\sigma_{ij}\}$, $\{\rho_{ij}\}$, and $\{\mu_{ij}\}$, as shown in Fig. 3.4(c). Each set contributes to the model output in terms of the constant bias, lonely stroke and its coupling with repetitive cycles, and the repetitive hysteresis cycles, respectively. Such clean formulation facilitates model identification and analysis. On the other hand, when m is not an integer, there will be one column of densities divided such that a portion of it contributes toward capturing the repetitive cycles, and the other toward capturing the

lonely stroke. Ideally, different densities exist to the right and left portions of this column for accurate modeling, however, this is not possible as the density in each cell is considered to be a constant (Section 3.3). Regardless, this formulation should still work, although with less predictable modeling performance. Meanwhile, the Preisach density function is often discretized densely for improved modeling accuracy, in the range of 10 to 30 (102; 103). The densely discretized model can still be implemented efficiently. For example, the average computational time of a Preisach operator with $L = 20$ was around 0.35 ms (103). Thus, it is convenient and appropriate to consider m as a positive integer.

The signs of densities $\{\rho_{ij}\}$ and $\{\mu_{ij}\}$ determine the monotonicity and the relative locations of the lonely stroke and the repetitive hysteresis cycles. There is no constraint on the densities $\{\sigma_{ij}\}$ because it acts as a constant bias. Motivated by the existing experimental measurements of the hysteresis with lonely stroke behaviors in a variety of artificial muscles, the following four cases are considered:

- Case 1: The input-output relationship is monotonically increasing and the lonely stroke lies below the repetitive hysteresis cycles. An example of such case is shown in Fig. 3.4(b). In this case, the densities are non-negative:

$$\{\rho_{ij}\} \geq 0, \{\mu_{ij}\} \geq 0.$$

- Case 2: The input-output relationship is monotonically decreasing and the lonely stroke lies above the repetitive hysteresis cycles (more details in Section 3.7.1). In this case, the densities are non-positive:

$$\{\rho_{ij}\} \leq 0, \{\mu_{ij}\} \leq 0.$$

Theorem 1 *(a): When the densities of the proposed expanded Preisach operator satisfy any of the four proposed cases, the largest discrepancy of the output at* $i_{\min}$

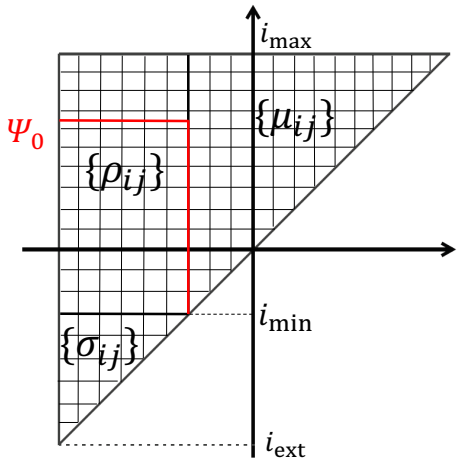

Figure 3.5: Illustration of the expanded Preisach operator with a memory curve ψ_0.

(Fig. 3.4(b)) can be expressed as $e_{\max} = 2l_e^2 \left| \sum_{i=m+1}^{L} \sum_{j=1}^{m} \rho_{ij} \right|$. *(b): When all the densities of the proposed expanded Preisach operator are either non-negative or non-positive (Case 1 or Case 2), elimination of lonely stroke results in a reduction of the output range:* $D = 2l_e^2 | \sum_{i=m+1}^{L} \sum_{j=1}^{m} \rho_{ij} |$.

Proof of Theorem 1 (a): Without loss of generality, consider an expanded Preisach operator with a memory curve ψ_0, as shown in Fig. 3.5. The system starts with all hysterons with densities $\{\sigma_{ij}\}$ activated. Due to the lonely stroke, the output at $i_{\min}$ is not fixed but history-dependent. At $i_{\min}$, the hysterons associated with densities $\{\sigma_{ij}\}$ and $\{\mu_{ij}\}$ will always be $+1$ and -1, respectively, due to the fact that the memory curve will always be above all hysterons associated with $\{\sigma_{ij}\}$ and left of all hysterons associated with $\{\mu_{ij}\}$. The outputs of the hysterons associated with $\{\rho_{ij}\}$ will be dependent on the input history. The largest output discrepancy at $i_{\min}$ would thus occur when all the hysterons associated with $\{\rho_{ij}\}$ are -1 and $+1$, respectively. One way to obtain the largest output discrepancy at $i_{\min}$ is as follows: Consider an input sequence which starts with $i_{\min}$. In the beginning, all hysterons associated with $\{\rho_{ij}\}$ and $\{\mu_{ij}\}$ are -1. After the input monotonically increases from $i_{\min}$ to

$i_{\max}$, all hysterons associated with densities $\{\rho_{ij}\}$ and $\{\mu_{ij}\}$ will be $+1$. When the input monotonically decreases from $i_{\max}$ to $i_{\min}$, all hysterons with densities $\{\mu_{ij}\}$ and $\{\rho_{ij}\}$ will be -1 and $+1$, respectively. The outputs, u_1 and u_2, at the beginning and end of the input cycles, respectively, are:

$$\begin{aligned} u_1 = &\sum_{i=2}^{m}\sum_{j=1}^{i-1} l_e^2\sigma_{ij} + \sum_{i=1}^{m}\frac{l_e^2}{2}\sigma_{ii} - \sum_{i=m+1}^{L}\sum_{j=1}^{m} l_e^2\rho_{ij} \\ &- \sum_{i=m+1}^{L}\sum_{j=m+1}^{i-1} l_e^2\mu_{ij} - \sum_{i=m+1}^{L}\frac{l_e^2}{2}\mu_{ii}, \\ u_2 = &\sum_{i=2}^{m}\sum_{j=1}^{i-1} l_e^2\sigma_{ij} + \sum_{i=1}^{m}\frac{l_e^2}{2}\sigma_{ii} + \sum_{i=m+1}^{L}\sum_{j=1}^{m} l_e^2\rho_{ij} \\ &- \sum_{i=m+1}^{L}\sum_{j=m+1}^{i} l_e^2\mu_{ij} - \sum_{i=m+1}^{L}\frac{l_e^2}{2}\mu_{ii}. \end{aligned}$$

Thus, the largest output discrepancy at $i_{\min}$ is expressed as

$$e_{\max} = |u_2 - u_1| = 2l_e^2\left|\sum_{i=m+1}^{L}\sum_{j=1}^{m}\rho_{ij}\right|. \tag{3.7}$$

(b): Consider the expanded Preisach operator follows Case 1 that the relevant densities are non-negative. Let R_1 and R_2 be its output ranges while considering the lonely stroke and not considering the lonely stroke, respectively. R_1 and R_2 can be expressed by

$$\begin{aligned} R_1 &= 2\left(\sum_{i=m+1}^{L}\sum_{j=1}^{m}\rho_{ij}l_e^2 + \sum_{i=m+1}^{L}\sum_{j=m+1}^{i-1} l_e^2\mu_{ij} + \sum_{i=j=m+1}^{L}\frac{l_e^2}{2}\mu_{ij}\right), \\ R_2 &= 2\left(\sum_{i=m+1}^{L}\sum_{j=m+1}^{i-1} l_e^2\mu_{ij} + \sum_{i=j=m+1}^{L}\frac{l_e^2}{2}\mu_{ij}\right). \end{aligned}$$

The elimination of the lonely stroke results in a reduction of output range expressed as

$$D = |R_1 - R_2| = 2l_e^2\left|\sum_{i=m+1}^{L}\sum_{j=1}^{m}\rho_{ij}\right|.$$

Similar analysis can be applied to Case 2, where all densities are non-positive.

3.3.2 Identification

The densities $\{\sigma_{ij}\}$, $\{\rho_{ij}\}$, and $\{\mu_{ij}\}$ can be identified as a least-squares problem, given the input and output measurements, namely, $i[n]$, $\hat{u}[n]$, $n = 1, ..., N$. N is the total number of measurements. The input sequence $i[n]$ is fed into the expanded Preisach operator and the states of the hysterons $\{s_{ij}: \ i = 1, ..., L; \ j = 1, ..., i\}$ are computed. The output of the model at time instant n is obtained following Eq. (3.6). The least squares method can be used to estimate the parameters such that the model estimation error, $\sum_{n=1}^{N} |\hat{u}[n] - u[n]|^2$, is minimized. This can be written in a more compact form. Let

$$A = \begin{bmatrix} s_{11}[1] & s_{21}[1] & \cdots & s_{LL}[1] \\ s_{11}[2] & s_{21}[2] & \cdots & s_{LL}[2] \\ \vdots & \vdots & \ddots & \vdots \\ s_{11}[N] & s_{21}[N] & \cdots & s_{LL}[N] \end{bmatrix}, b = \begin{bmatrix} \hat{u}[1] \\ \hat{u}[2] \\ \vdots \\ \hat{u}[N] \end{bmatrix}, \theta = \begin{bmatrix} \theta_{11} \\ \theta_{21} \\ \vdots \\ \theta_{LL} \end{bmatrix},$$

where, $\theta = \sigma \cup \rho \cup \mu$: σ, ρ, and μ represent the density sets $\{\sigma_{ij}\}$, $\{\rho_{ij}\}$, and $\{\mu_{ij}\}$, respectively. Each row in matrix A is a $1 \times \frac{L(L+1)}{2}$ vector describing the states of the hysterons such that $A_{(k,n)} = s_{ij}[n], k = 1, 2, ... \frac{L(L+1)}{2}, n = 1, 2, ..., N$ with $i = 1, 2, ...L$ and for each i, $j = 1, 2, ..., i$. Each pair of i and j corresponds to a unique value of k such that $k = \frac{i(i-1)}{2} + j$. For example, $i = 1$, $j = 1$ corresponds to $k = 1$; $i = 2$, $j = 1$ corresponds to $k = 2$. Similar order is followed for the density vector θ. The dimensions of the density sets σ, ρ, and μ are $\frac{m(m+1)}{2} \times 1$, $(L-m)m \times 1$, and $\frac{(L-m)(L-m+1)}{2} \times 1$, respectively. The dimensions of matrix A and vector b are $N \times \frac{L(L+1)}{2}$ and $N \times 1$, respectively. Then the problem becomes finding θ such that

$$||A\theta - b|| \tag{3.8}$$

is minimized, where $||\cdot||$ stands for the Euclidean norm in $\mathbb{R}^N$. The densities can be identified using the *lsqlin* or *lsqnonneg* functions in MATLAB, by describing matrix

A and vector b, and applying the constraints based on monotonicity and relative locations of the hysteresis with lonely stroke measurements in different cases detailed in Section 3.4.2.

Theorem 2 *Assume the discretization level of the proposed expanded Preisach operator, L, is fixed. The minimum modeling error is obtained when the number of expanded columns to the density function of the proposed model, m, is 1.*

Proof of Theorem 2

Firstly, increasing m beyond 1 will not improve the accuracy of the proposed model. Without loss of generality, assume the hysteresis with lonely stroke behavior follows Case 1: the input-output relationship is monotonically increasing with the lonely stroke lying below the repeatable hysteresis cycles. Since the input will never go below $i_{\min}$, the hysterons associated with densities $\{\rho_{ij}\}$ will only get converted from -1 to $+1$ but never from $+1$ to -1. As a result, when the input is increasing, an entire row of hysterons with densities $\{\rho_{ij}\}$ will either convert from -1 to $+1$ or remain the same depending on the input history; When the input is decreasing, all hysterons associated with $\{\rho_{ij}\}$ will not change. Since an entire row of hysterons corresponding to $\{\rho_{ij}\}$ always behave in exactly the same manner, increasing m beyond 1 will not affect the model accuracy. Secondly, when L is fixed, increasing m is equivalent to decreasing $(L-m) = L_0$. In this way, the number of parameters used to estimate the repetitive hysteresis cycles is decreased ([102]; [103]). Therefore, increasing m will not improve the modeling performance. A desirable way to choose L is thus to first determine the level of discretization L_0 required to accurately capture the repeatable cycles. Then L would be L_0+1.

3.3.3 Comparison Models

A polynomial model and a conventional Preisach operator were selected for performance comparison purposes. Details about the Preisach operator are provided in Section 3.3. An n^{th}-order polynomial model was written as

$$O(i) = p_n i^n + \cdots + p_2 i^2 + p_1 i + p_0, \tag{3.9}$$

where O denotes the model output, p_0, p_1, $\cdots$, p_n are constants, and i is the input.

3.3.4 Inverse Compensation

To compensate for the nonlinearity of expanded Preisach operator, an iterative algorithm is obtained by approximately inverting the proposed model. The proposed algorithm is adapted from methods ([72]). The inverse compensation problem can be formulated as follows: given a desired output value u_d and the current memory curve ψ_0, to find a new input i_d, such that when applied, the output approximately reaches the desired value, u_d, namely, $u_d \approx \Lambda[i_d; \psi_0]$. Let the input and output corresponding to the initial input history ψ_0 be $\bar{i}$ and $\bar{u}$, respectively. The proposed algorithm works as follows: Without loss of generality, assume the expanded Preisach operator follows a monotonically increasing input-output correlation (Case 1). The initial input and output, $\bar{i}$ and $\bar{u}$, can be computed from the current memory curve ψ_0. If the desired output u_d is smaller than the previous output $\bar{u}$, then the input is decreased in small steps from the previous input $\bar{i}$. After each step, an output of the expanded Preisach operator is computed and compared with u_d. If the computed output value is very close to u_d, the corresponding input is selected to be i_d at that instant. Similarly, when u_d is greater than $\bar{u}$, the procedure is repeated with the input increasing from $\bar{i}$.

The algorithm is presented as **Algorithm 1**. For a monotonically decreasing input-output correlation (Case 2), the *sign* value in **Algorithm 1** will be 1 if $u_d < \bar{u}$ and will be -1 if $u_d \geq \bar{u}$. Also, Δ_1 and Δ_2 are tolerances of the inverse compensation algorithm and are thus selected based on the required degree of accuracy.

Algorithm 1 Inverse Compensation Algorithm ([72])

$i^{(0)} := \bar{i}$, $u^{(0)} = \bar{u}$, $\psi^{(0)} = \psi_0$, $n = 0$
Choose any ω such that $0 < \omega < (i_{\max} - i_{\text{ext}})/L$
if $u_d > \bar{u}$ **then**
    sign $= 1$
else
    sign $= -1$
Step 1: Calculate ${a_1}^{(n)}$ and ${a_2}^{(n)}$ such that $\Lambda[i^{(n)} + sign \cdot \omega; \psi^{(n)}] - \Lambda[i^{(n)}; \psi^{(n)}] = {a_1}^{(n)}\omega^2 + {a_2}^{(n)}\omega$
Calculate ω_0 such that $u_d - \Lambda[i^{(n)}; \psi^{(n)}] = {a_1}^{(n)}\omega_0^2 + {a_2}^{(n)}\omega_0$
Step 2: $n = n + 1$, $i^{(n)} = i^{(n-1)} + sign \cdot \omega$,
$u^{(n)} = \Lambda[i^{(n)} + sign \cdot \omega; \psi^{(n)}]$
Choose Δ_1 and Δ_2 such that $0 < \Delta_1 < 1$ and $0 < \Delta_2 < 1$
if $||\omega_0 - \omega|| < \Delta_1$ *or* $||u_d - \Lambda[i^{(n)} + \omega; \psi^{(n)}]|| < \Delta_2$ **then**
    $i_d = i^{(n)}$, **end**.
else
    Go back to **Step 1**

3.4 Simulation Results

To obtain the ideal input/output data set used to evaluate the effectiveness of the proposed model, the following procedure was adopted: Firstly, the input oscillation sequence consisting of 12 cycles with increasing maximum magnitudes, was generated, as depicted in Fig. 3.6(a) where the index on the X-axis denotes the numbering of applied input values. The minimum and maximum values of the input sequence, $i_{\min}$ and $i_{\max}$, were 0 and 6, respectively. This input sequence was an appropriate testing input because the corresponding output sequence contained rich information about

the repetitive hysteresis cycles, the lonely stroke, and their coupling. Secondly, the expanded Preisach operator was established, with i_{ext} selected to be -6, to ensure that $i_{\text{ext}} < i_{\min}$. Similar to (104), the values of the density function were generated according to the Gaussian function as follows:

$$\theta_{ij} = \exp\left(-\frac{(i-30)^2+(j-30)^2}{600}\right), \tag{3.10}$$

where $i = 1, 2, ..., L$; $j = 1, 2, ..., i$, as shown in Fig. 3.6(b). The level of discretization L was 60. Finally, by passing the input sequence to the expanded Preisach operator, the output values were obtained. The largest discrepancy due to the lonely stroke behavior at $i_{\min}$ was 31.67, which agreed with the value obtained through Eq. (3.7) in **Theorem 1**.

To test the effectiveness of the proposed model, a number of expanded Preisach operators with different values of discretization level $L < 60$ and i_{ext}, were attempted to capture the constructed complex input-output data set. As an example, the effects of different values of i_{ext}, determined as a function of m according to Eq. (3.5), was tested for $L = 5$, as shown in Figs. 3.6(c)-(e). Fig. 3.6(c) illustrates the modeling results with a conventional Preisach operator which produced a large root mean square (RMS) error of 5.46. The error was 0.24 when the proposed model with $m = 1$ was adopted (Fig. 3.6(d)). Beyond that, the RMS error further increased. The case where $m = 4$ resulted in an RMS error of 2.23 (Fig. 3.6(e)). To more systematically examine the effects of different values of L and i_{ext} on the modeling performance, the expanded Preisach operator was tested with different values of L, namely 2, 4, 6, and 8. For each L value, the i_{ext} value was determined such that $m = 1, 2..., L$. As shown in Fig. 3.7(a), for any given value of L, the modeling RMS error reached the minimum when m was equal to 1. The RMS error further increased as m increased and approached the maximum value as m approached L. In the case with $m = L$,

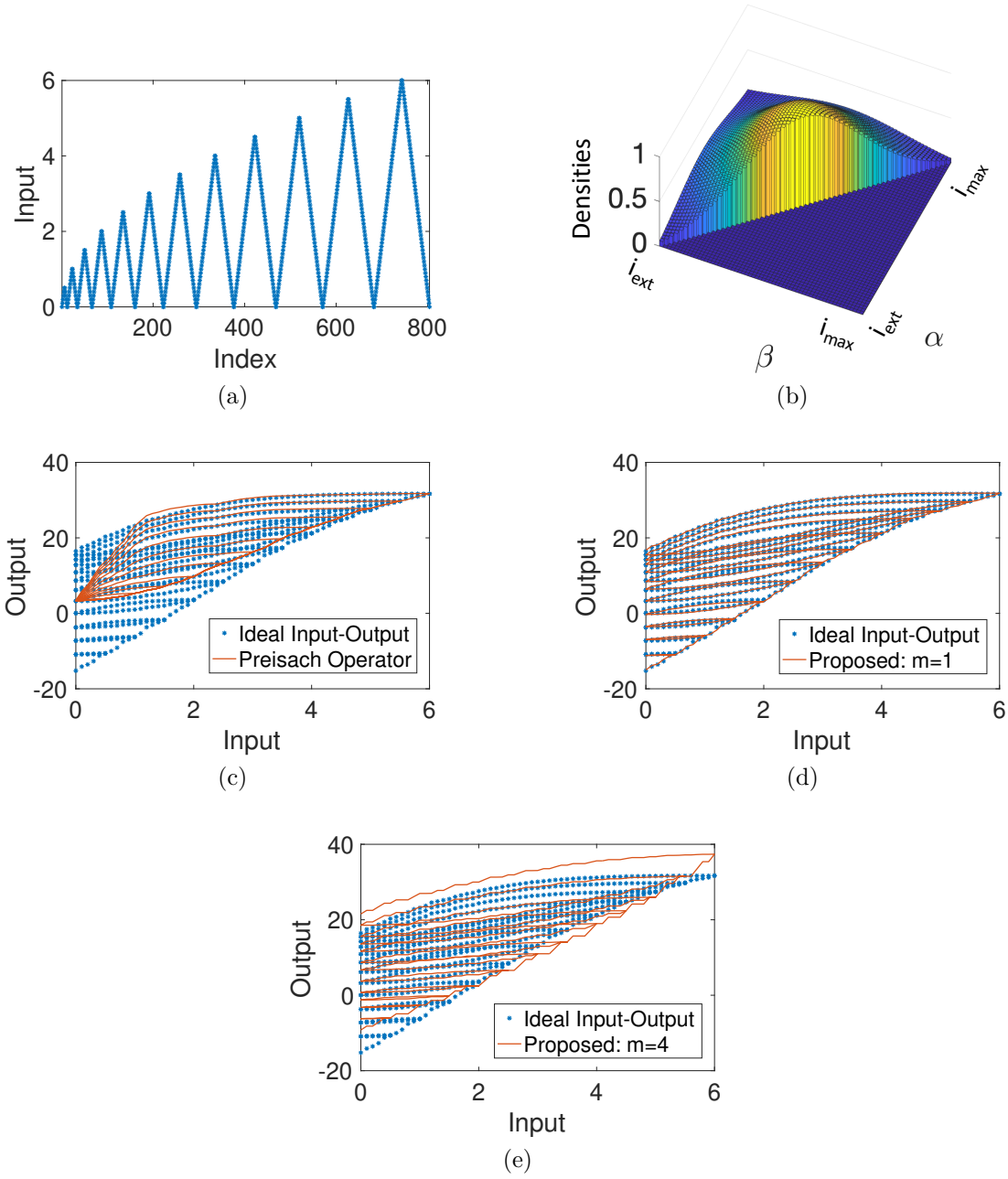

Figure 3.6: (a) An input sequence with 12 cycles. (b) Density function generated using Eq. (3.10). For $L = 5$, model identification results with (c) Preisach operator, and proposed approach with m equals to (d) 1 and (e) 4.

all the densities played the role of $\{\sigma_{ij}\}$, which was degenerated to a constant bias, thereby resulting in maximum error. Furthermore, for a fixed $m \geq 1$, the modeling

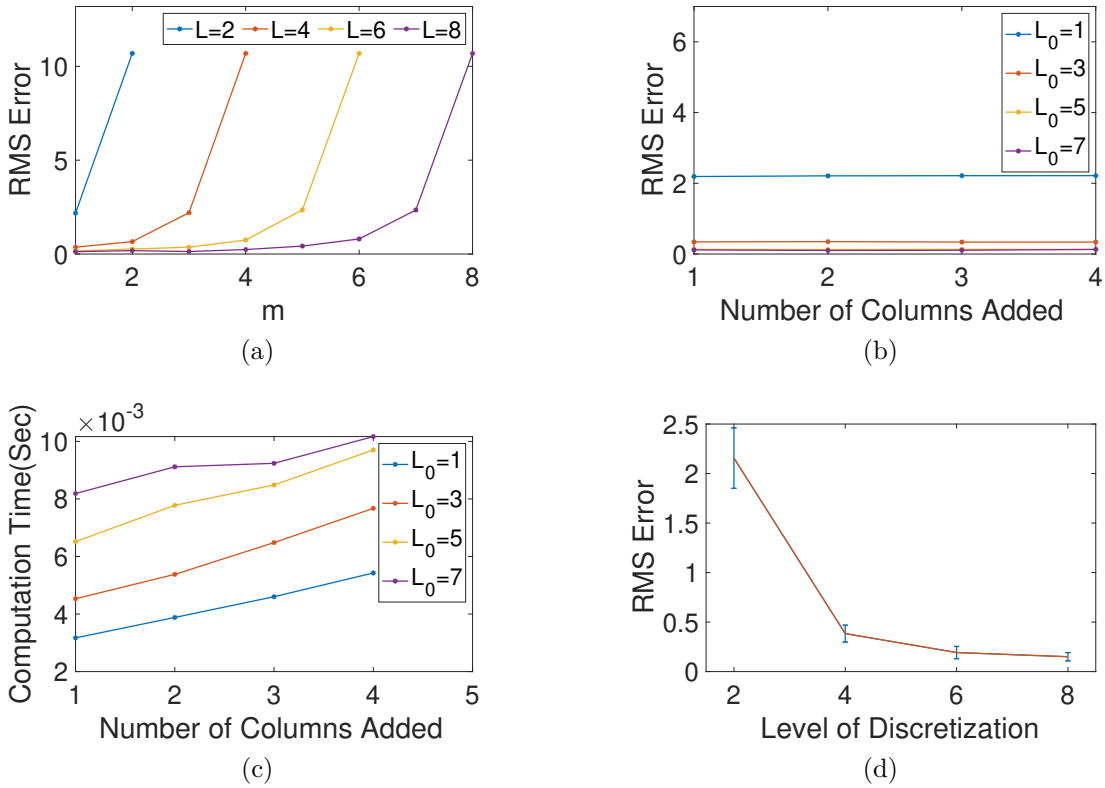

Figure 3.7: (a) Root mean square (RMS) error for different values of L and m. (b) Modeling Error for different number of additional columns for fixed values of L_0. (c) Computational time for different number of additional columns for fixed values of L_0. (d) Statistical analysis of the proposed model with different levels of discretization L.

error decreased when L is increased. The results agree well with **Theorem 2**.

It was also verified that, after fixing L_0, the level of discretization to capture the repeatable hysteresis, expanding one extra column for capturing the lonely stroke ($m = 1$) resulted in the most satisfactory modeling performance when the model accuracy and computational time are both considered, as stated in Section 3.4.3. The expanded Preisach operator was constructed with different values of L_0, namely 1, 3, 5, and 7 and for each case, different values of m, namely 1, 2, 3, and 4, were used. Expanding the operator by more than one column ($m > 1$) resulted in RMS error with no difference when compared to the RMS error obtained using the operator

with one additional column, as shown in Fig. 3.7(b). However, increasing m resulted in higher computational time as shown in Fig. 3.7(c). This result was in agreement with the **Theorem 2**. Also, as expected, both the accuracy and the computational time of the model increased as L_0 increased with a fixed m. The simulations were performed on a computer with 32 GB RAM, which runs at 2.9 GHz speed.

Lastly, a statistical analysis was performed to study the robustness of the proposed modeling approach for different hysteresis with lonely stroke behaviors. The proposed approach was used to estimate 100 sets of input-output sequences that were generated using different densities, L, and m values. By assigning different values of densities manually to different cells of the extended columns, different shapes of lonely stroke behaviors were obtained. These data sets were captured using extended Preisach operators with different L values and fixed $m = 1$. Fig. 3.7(d) shows the effect of L on the modeling RMS error – the modeling error decreased when the discretization level was increased. For example, the average modeling error for $L = 6$ was 0.19 for an output range of around 45. It indicated that the proposed approach was robust to different hysteresis with lonely stroke behaviors.

3.5 Experimental Results

For the purpose of validating the proposed modeling strategy, the input–output correlation of the TSA-driven soft robotic finger which was part of the TSA-driven soft gripper (43) is utilized. This was done because the input–output correlations of the soft finger exhibited significantly large lonely stroke as compared to the input–output correlations of the proposed TSA-driven soft robotic manipulator (presented in Chapter 2). The input–output correlation of the soft finger can be categorized as Case 1

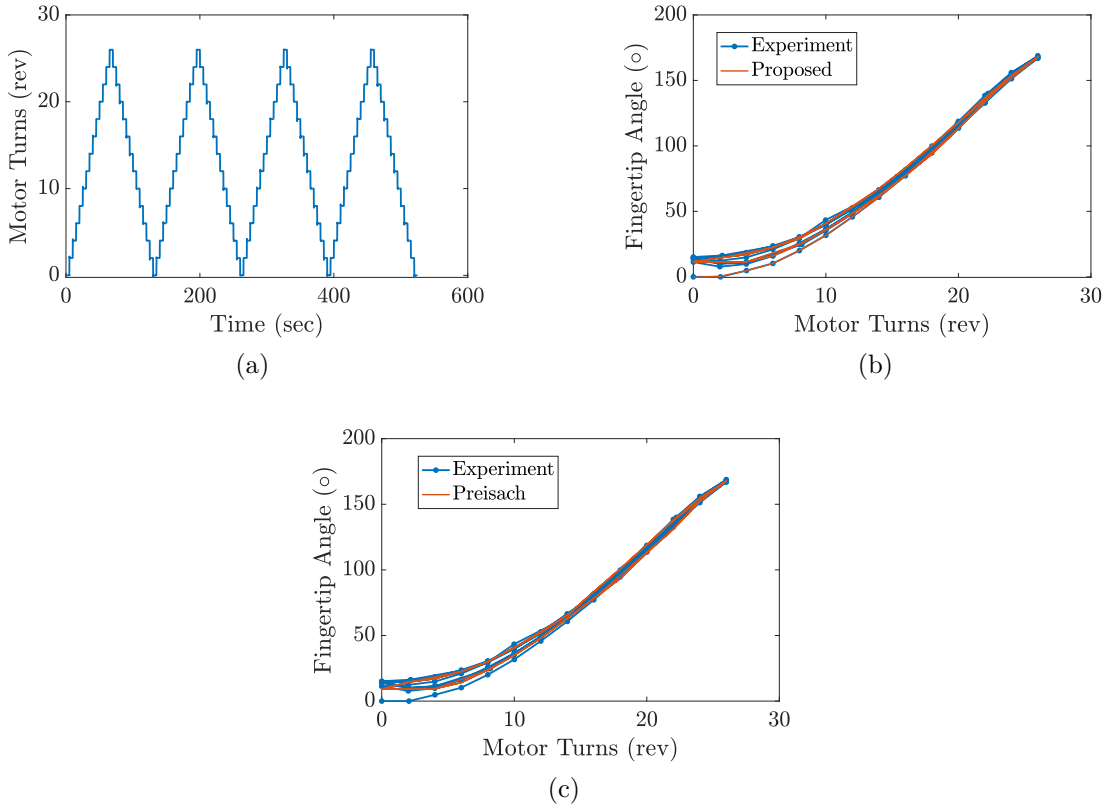

Figure 3.8: (a) Input sequence for model identification. Model identification results with (b) the proposed approach, and (c) a conventional Preisach operator.

of the hysteresis with lonely stroke behavior. In addition, for further validating the proposed modeling and inverse compensation strategies quasi-static voltage-strain relationship of an SCP actuator are considered. This was done for same reasons as described above. The input–output correlation of the SCP actuators can be considered as Case 2 of the hysteresis with lonely stroke behavior.

3.5.1 TSA-Driven Soft Robotic Finger

The model identification results of the quasi-static motor turns–fingertip angle correlation of a TSA-driven soft finger are presented. A motor turns input sequence

ranging from 0 rev to 25 rev was applied with a step size of 2 rev, as shown in Fig. 3.8(a). The wait time for each applied motor turns was 2 seconds. This value ensured that a quasi-static strain value was obtained. The density function of the proposed model is identified such that all the densities are more than or equal to 0, since fingertip angle output increases monotonically with motor turns input. The L value was chosen to be 15, and the Preisach plane was constructed with i_{ext} and $i_{\max}$ as -1.86 and 26, respectively. This choice of i_{ext} ensured that $m = 1$. The results obtained through the proposed model are compared with a conventional Preisach operator. The model identification results are presented in Figs. 3.8(b)-(c). As it can be seen, only the proposed approach captures the lonely stroke phenomenon with high degree of accuracy. The modeling error with the proposed approach and the traditional approach are 2.13°, and 3.12° respectively.

3.5.2 Supercoiled Polymer (SCP) Actuators

The model identification and validation results of the quasi-static voltage-strain relationship of an SCP actuator are presented, when the load is switched from a higher value to a lower value. A voltage input sequence ranging from 0 V to 11.5 V was applied with a step size of 0.23 V, as shown in Fig. 3.9(a). The wait time for each applied voltage was 10 seconds. This value ensured that a quasi-static strain value was obtained. The voltage input sequence was applied after waiting for approximately 60 seconds once the load was switched. Note that this wait time is for mechanical load input, in contrast to the 10 seconds wait time for the voltage input. This was done to ensure that the SCP actuator settled at a quasi-static value as a result of the change in loads. The step size was selected to obtain smooth output curves. The load was switched from 400 g to 200 g.

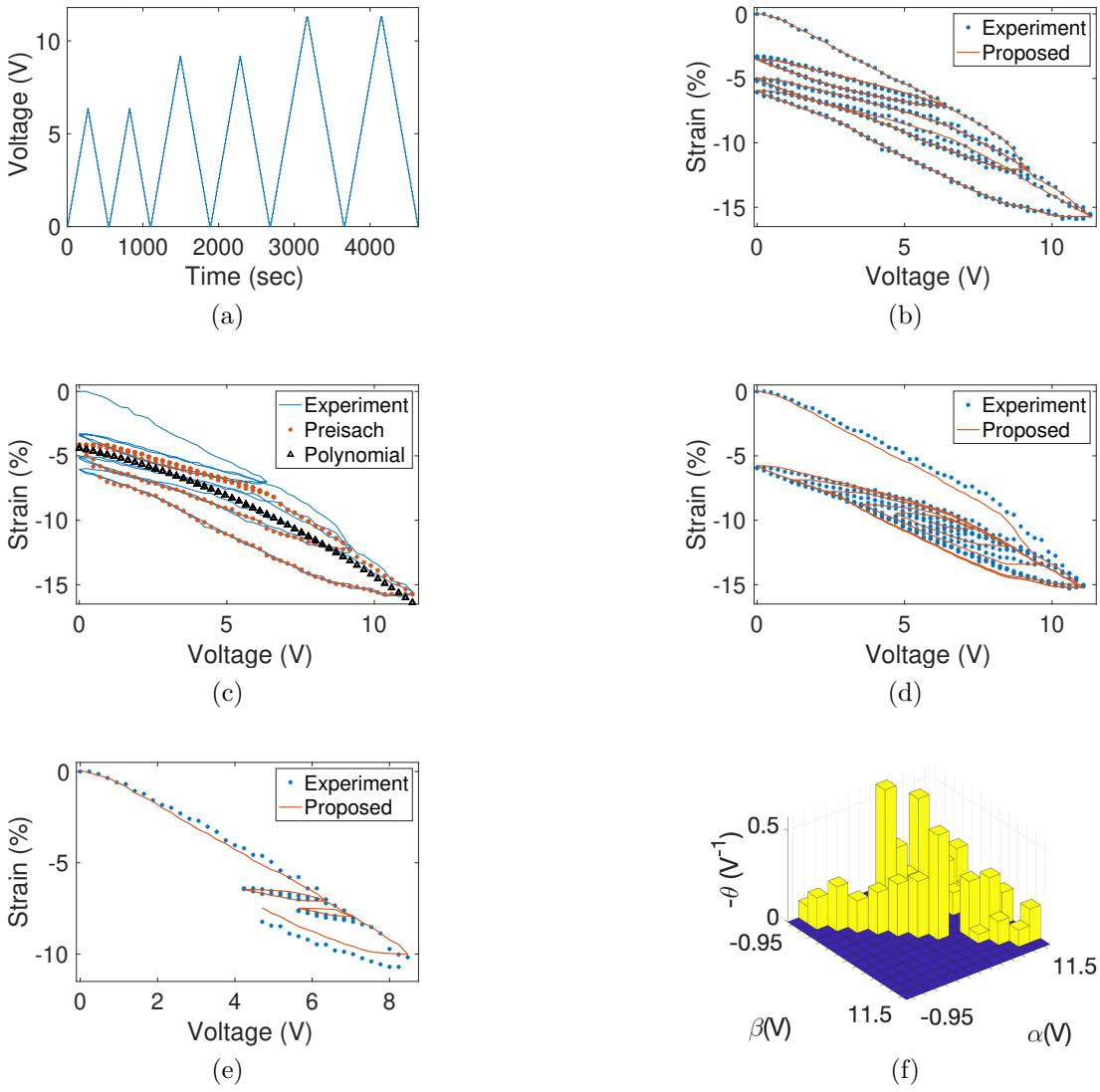

Figure 3.9: (a) Input sequence for model identification. Model identification results with (b) the proposed approach, (c) a conventional Preisach operator, and a second-order polynomial model. Validation results under (d) input sequence #1. (e) input sequence #2. (f) Preisach plane with densities.

The density function of the proposed model is identified such that all the densities are less than or equal to 0, since strain output decreases monotonically with voltage input. The L value was chosen to be 13, and the Preisach plane was constructed with i_{ext} and $i_{\max}$ as -0.95 and 11.5, respectively. This choice of i_{ext} ensured that $m = 1$.

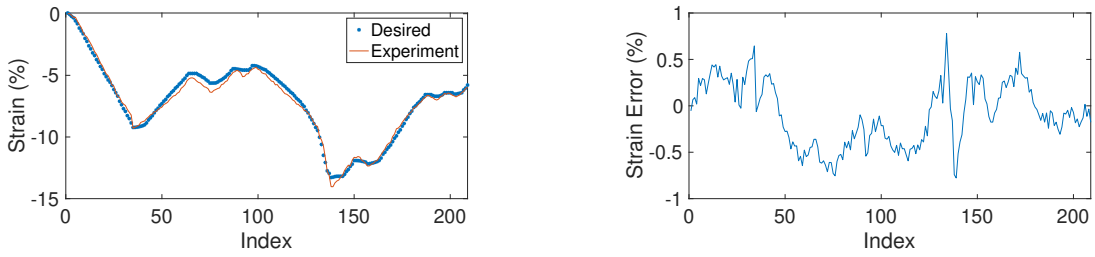

(a) (b)

Figure 3.10: (a) Open-loop control performance for the presented inverse compensation algorithm. (b) Strain control error.

The results obtained through the proposed model are compared with a conventional Preisach operator and a second-order polynomial model. The model identification results are presented in Figs. 3.9(b)-(c). As it can be seen, only the proposed approach captures the lonely stroke phenomenon with high degree of accuracy. The modeling error with the proposed approach, the traditional approach and the polynomial model are 0.09%, 0.59%, and 1.36% respectively.

The proposed model is further validated by applying two different voltage sequences to the SCP actuator. The strain estimates for the two verification correlations are presented in Figs. 3.9(d)-(e). The model verification errors were slightly higher than the model identification error. The validation error with the proposed approach for the correlations presented in Figs. 3.9(d) and (e) are 0.29% and 0.20%, respectively. The errors with traditional approach are 0.71% and 1.18% while with the polynomial model are 1.53% and 2.09% respectively. Also, as suggested in Section 3.3.B, the density of the first cell in the Preisach plane is not comparable to the remaining densities, and is thus not plotted in Fig. 3.9(f). The value of the density of the first cell was $-9.93V^{-1}$. The model validation further confirms the effectiveness of the proposed modeling approach.

The performance of the presented inversion algorithm is examined through an open-loop strain-tracking experiment. The values of Δ_1 and Δ_2 are selected to be 0.04 and 0.12, respectively. These values are determined experimentally and ensured maximum accuracy while not consuming large computational times. A randomly chosen sequence of the desired steady-state strains is generated, as shown in Fig. 3.10(a). Fig. 3.10(a) shows the experimental strain output measurements obtained under the proposed inverse compensation scheme. Fig. 3.10(b) shows the corresponding control error between the desired output and actual output. The inverse compensation scheme is proven to be effective, with the mean error of 0.34% strain.

CHAPTER 4

PARAMETER ESTIMATION AND ADAPTIVE CONTROL OF TWISTED STRING ACTUATORS

In this chapter, we present adaptive parameter estimation and control strategies to accurately estimate the TSA system parameters and control the TSA with high performance. The aforementioned strategies will be developed by assuming that the external force and the system parameters are unknown. The parameter estimation algorithm consists of two stages: 1) the kinetostatic model of the TSA will be used to estimate a term which is a combination of the applied force and the longitudinal stiffness of the strings. 2) The remaining systems parameters will be estimated in the second stage, where the estimated quantity from the first stage will be used as a measurable quantity. The proposed control strategy utilizes direct model reference adaptive control (MRAC) and adaptive feedback linearization. The developed estimation and control strategies were validated through a detailed simulation study. The performance of the proposed control strategy was compared with a proportional controller (PC) and a proportional controller with a feedforward term (PCFF). The contents of this chapter are based on the findings presented in (105).

4.1 Motivation

Previous studies have presented highly accurate TSA models by considering different phenomena such as varying radius of the strings along the range of actuation, friction in different parts of the system, and finite string stiffness (49; 27; 65). However, limited studies have been conducted on TSAs considering time-varying properties. While existing modeling and control strategies show strong promise (49; 31; 106; 59), they exhibit a few limitations. Firstly, the external force applied to the TSAs is

assumed to be measurable or predictable. Secondly, it is assumed that all the system parameters are accurately known. Existing studies do not consider the effects of wear and tear and long term usage on the system parameters. However, in practical scenarios these assumptions may not be valid, especially during long-term operation of TSA-driven systems. For example, in most robotic and mechatronic applications, the external force can be complex, highly dynamic, and difficult to predict or measure. In addition, the system parameters such as the string stiffnesses could change over time due to general wear and tear, creep, and when used over long durations of time ([85]; [107]). Furthermore, TSAs have also shown load-dependent hysteretic behavior ([41]; [40]; [27]). These behaviors could be difficult to predict accurately. Similarly, while most motor parameters can be obtained from the data provided by the manufacturer, in inexpensive motors, the effect of wear and tear might not be negligible when used in practical applications ([86]). Under such circumstances, control strategies that employ adaptive laws to estimate system or control parameters could be highly suitable.

A previous study on TSA control employed adaptive parameter estimation to estimate the changing radius of the strings across the actuation range ([108]). However, it was assumed that the external force was constant and all the system parameters besides the string radius were accurately known. Similarly, in ([86]), an adaptive robust control strategy was developed to handle the synchronization of two antagonistic TSAs in an assistive robotic device. However, string compliance, finite string stiffnesses, varying external forces, and their effects on the system dynamics were not considered.

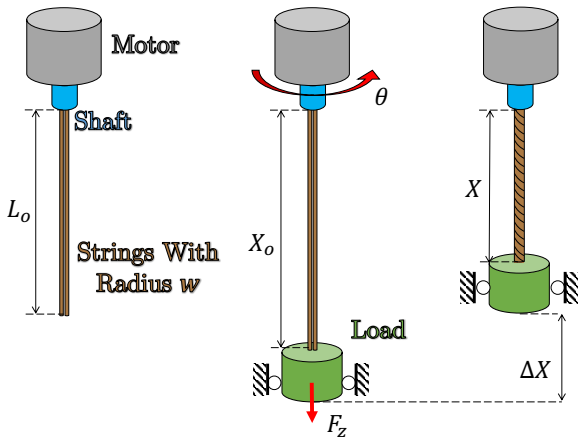

Figure 4.1: The schematic of a TSA with system parameters labelled.

4.2 Model Overview

In this section, an overview of the kinetostatic and dynamic models of the TSA (Fig. 4.1) will be presented. The models presented in this chapter differ from the models presented in Chapter 2 as string compliance and finite string stiffnesses are considered in this chapter. Models presented in chapter 2 can be considered as simplified versions of the models presented in this chapter.

Kinetostatic Model

The length X of the TSA can be expressed as

$$X = \sqrt{L_0^2 \left(1 + \frac{F_s}{K_L}\right)^2 - \theta^2 w^2}, \tag{4.1}$$

where L_0 is the unloaded and untwisted string length, F_s is the fiber tension in the strings, K_L is the longitudinal stiffness of a single string normalized to its unit length, θ is the rotation angle of the motor's shaft, and w is the radius of the TSA (49). w depends on the number of strings N in the TSA. In this work, N is chosen to be 2 because 2-string-TSA is the most common configuration (9; 33; 65; 49). Previous

work also accounted for the initial gap between the parallel strings in the computation of X ([109]), but in this work we assume that the TSA's initial gap is negligible. This assumption is valid since in practice, the gap between the strings can be made very small. The fiber tension F_s is computed as

$$F_s = \frac{K_L}{L_0}(X - L_0) = \frac{F_z X_0}{NX}, \tag{4.2}$$

where X_0 is the untwisted and loaded length of the TSA ([49]). F_z is the total opposing force from the payload ([49]). For simplicity purposes, the TSA's radius is assumed to be constant across the actuation range. This assumption has been shown to produce satisfactory results ([33; 65; 109]).

Dynamic Model

The dynamic model of the TSA can be described by the following equation:

$$\tau_m = J\ddot{\theta} + \left(H + \frac{1}{2}\frac{\partial C_x}{\partial \theta}F_z\right)F_z + b_\theta\dot{\theta} + \tau_c \text{sgn}(\dot{\theta}), \tag{4.3}$$

where J is the motor's moment of inertia, H is the Jacobian of the TSA, $\partial C_x/\partial\theta$ is the partial derivative of the strings' compliance, b_θ is the motor's viscous friction coefficient, τ_m is the torque output of the motor, and τ_c is the Coulombic friction constant of the motor ([65]). Similar to previous studies, in this work, it is assumed that the electrical dynamics of the system are much faster than the mechanical dynamics ([65; 59]). Therefore, τ_m can be written as $\tau_m = \frac{K_t}{R}v$, where K_t is the motor constant, R is the terminal resistance of the motor, and v is the input voltage. In ([27; 49]), the Jacobian of the TSA is $H = (\theta w^2)/X$. $\partial C_x/\partial\theta$ is modeled as

$$\frac{\partial C_x}{\partial \theta} = 2\left(\frac{w}{X^2}\right)^2\left(\frac{2L_0^2 - w^2\theta^2}{K_w}w\theta^3 + \frac{L_0^3}{K_L}\theta\right), \tag{4.4}$$

where K_w is the normalized radial stiffness of the strings ([65]). For the purpose of this study, it is assumed that $\tau_c = 0$ and all the system parameters, namely, J, b_θ,

F_z, K_t, R, K_L, and K_w are unknown. It is assumed that the motor angle θ and the TSA contraction X are directly measurable. Previous studies have shown that τ_c is a constant which needs to be determined experimentally (65). To maintain simplicity, it is assumed that $\tau_c = 0$.

4.3 Parameter Estimation

The first step in the estimation algorithm is to estimate $\frac{F_s}{K_L}$ in Eq. (4.1). The parametric form of Eq. (4.1) can be written as $z_1 = \psi_1^{*T}\phi_1$, where $z_1 = X^2 + \theta^2 w^2$, $\psi_1^* = \left(1 + \frac{F_s}{K_L}\right)^2$, and $\phi_1 = L_0^2$. Let $\psi_1(t)$ be the estimate of ψ_1^*, and $\hat{z}_1$ be the estimated output using the estimated $\psi_1(t)$. The gradient algorithm to estimate $\psi_1(t)$ is expressed as

$$\dot{\psi_1} = \gamma_1 \epsilon_1 \phi_1, \tag{4.5}$$

where γ_1 is a positive constant, and $\epsilon_1 = z_1 - \hat{z}_1$. From $\psi_1(t)$, the estimated F_s/K_L, termed as $\hat{F}_s/\hat{K}_L$, can be obtained.

To formulate the algorithm to estimate the system parameters, Eq. (4.3) needs to be expressed in the parametric form. For this purpose, Eq. (4.3) can be written as follows:

$$v = \frac{RJ}{K_t}\ddot{\theta} + \frac{Rb_\theta}{K_t}\dot{\theta} + \frac{RK_L}{K_t} f_1(\theta) + \frac{RK_L^2}{K_t K_w} f_2(\theta), \tag{4.6}$$

where

$$f_1(\theta) = (F_z/K_L)^2 \left(\frac{w}{X^2}\right)^2 L_0^3 \theta + F_z/K_L \frac{\theta w^2}{X}, \tag{4.7}$$

$$f_2(\theta) = (F_z/K_L)^2 \left(\frac{w}{X^2}\right)^2 (L_0^2 + X^2) w \theta^3. \tag{4.8}$$

The parametric form of Eq. (4.6) can then be written as $z_2 = \psi_2^{*T}\phi_2$, where,

$$z_2 = \frac{V}{\Lambda(s)},\ \psi_2^* = \left[\frac{RJ}{K_t}\ \frac{Rb_\theta}{K_t}\ \frac{RK_L}{K_t}\ \frac{RK_L^2}{K_tK_w}\right]^T,$$

$$\phi_2 = \left[\frac{s^2\Theta}{\Lambda(s)}\ \frac{s\Theta}{\Lambda(s)}\ \frac{F_1}{\Lambda(s)}\ \frac{F_2}{\Lambda(s)}\right]^T,$$

where, V, Θ, F_1, and F_2 are the Laplace transforms of v, θ, f_1, and f_2, respectively. $\Lambda(s)$ is a second order polynomial with negative real roots. Let $\psi_2(t)$ be the parameter vector which needs to be estimated and $\hat{z}_2$ be the estimated output using $\psi_2(t)$. Then, the least squares estimation algorithm can be written as

$$\dot{\psi}_2 = P_2\epsilon_2\phi_2,\ \ \dot{P}_2 = \beta_2 P_2 - P_2\phi_2\phi_2^T P_2, \tag{4.9}$$

where $\beta_2 > 0$, and $\epsilon_2 = z_2 - \hat{z}_2$. The elements in ϕ_2 must be measurable. However, the $f_1(\theta)$ and $f_2(\theta)$ terms in ϕ_2 are not directly measurable because they consist of the F_z/K_L term, which is unknown. To make the algorithm work, $\hat{F}_z/\hat{K}_L$ is determined using $\hat{F}_s/\hat{K_L}$ according to Eq. (4.2). Then, $\hat{F}_z/\hat{K}_L$ is used to compute $\hat{f}_1$ and $\hat{f}_2$, which are the estimated values of f_1 and f_2, respectively. Therefore, ϕ_2 is assumed to be measurable. This is valid because, convergence of F_z/K_L can be ensured. Thus, $\hat{f}_1$ and $\hat{f}_2$ will become measurable quantities. It is noted that for $\psi_2(t)$ to converge to its true value of ψ_2^*, ϕ_2 must be persistently exciting (PE). Since the system is nonlinear in nature, it is difficult to analytically determine the PE condition of ϕ_2. The PE condition of ϕ_2 was numerically demonstrated in simulation (Section V).

4.4 Adaptive Control

4.4.1 Derivation of Control Input

The block diagram of the system with the adaptive control law is presented in Fig.

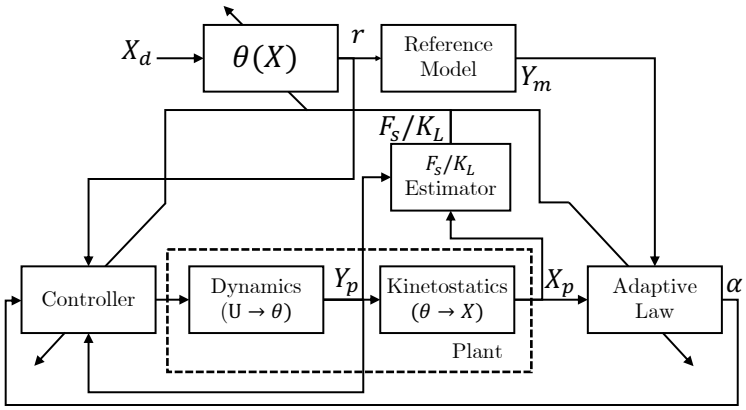

Figure 4.2: Block diagram for the model reference adaptive control (MRAC) with feedback linearization. For the controller, only the estimated value of F_s/K_L is required. The estimation of other system parameters is not required.

4.2. The Laplace transform of the reference model, which the system (Eq. (4.6)) will track, is written as

$$\Theta_m = \frac{d_1}{s+d_2} r, \tag{4.10}$$

where Θ_m is the Laplace transform of the model output θ_m, d_1 and d_2 are positive real numbers, and r is the reference signal. The proposed control input v is designed to be a summation of an MRAC term v_{MRAC} and an adaptive feedback linearization term v_{fl}. The adaptive feedback linearization term is to counter the effects of the nonlinear terms on the behavior of θ, and the MRAC term is selected to drive the control system to match a linear reference model.

Assume all the parameters of the system are accurately known. The proposed control input would be as follows ([110]):

$$\begin{aligned} v^* =& v^*_{\text{MRAC}} + v^*_{fl} \\ =& \alpha^*_1\omega_1 + \alpha^*_2\omega_2 + \alpha^*_3\theta + \\ & C^*_0 r + \alpha^*_4 f_1(\theta) + \alpha^*_5 f_2(\theta), \\ \dot{\omega^*_1} =& -\lambda_0\omega_1 + v^*, \;\; \dot{\omega^*_2} = -\lambda_0\omega_2 + \theta, \end{aligned} \tag{4.11}$$

where α^*_1, α^*_2, α^*_3, C^*_0, α^*_4, and α^*_5 are the control parameters computed using the

system parameters, and $\lambda_0 > 0$ is a design parameter (110). It is noted that α_4^* and α_5^* would be determined such that the $f_1(\theta)$ and $f_2(\theta)$ terms in Eq. (4.6) could be canceled out. The remaining control parameters would be computed such that the system behaves similar to the reference model presented in Eq. (4.10).

When the system parameters are not known, the control parameters in Eq. (4.11) must be estimated using adaptive laws. To derive the adaptive laws, the system model must be represented in state-space form as follows:

$$\dot{Y} = AY + BU + Lf, \;\; Y_p = C_c^T Y, \tag{4.12}$$

where

$$Y = \begin{bmatrix} \theta \\ \dot{\theta} \\ \omega_1 \\ \omega_2 \end{bmatrix}, A = \begin{bmatrix} 0 & 1 & 0 & 0 \\ 0 & \frac{-b_\theta}{J} & 0 & 0 \\ 0 & 0 & -\lambda_0 & 0 \\ 1 & 0 & 0 & -\lambda_0 \end{bmatrix}, B = \begin{bmatrix} 0 & 0 \\ \frac{K_t}{RJ} & \frac{K_t}{RJ} \\ 1 & 0 \\ 0 & 0 \end{bmatrix},$$

$$U = \begin{bmatrix} v_{\text{MRAC}} \\ v_{fl} \end{bmatrix}, L = \begin{bmatrix} 0 & 0 \\ \frac{K_L}{J} & \frac{K_L^2}{K_w J} \\ 0 & 0 \\ 0 & 0 \end{bmatrix}, f = \begin{bmatrix} f_1(\theta) \\ f_2(\theta) \end{bmatrix}, C_c = \begin{bmatrix} 1 & 1 \\ 0 & 0 \\ 0 & 0 \\ 0 & 0 \end{bmatrix}.$$

Addition and subtraction of the term BU^* with $U^* = [v_{\text{MRAC}}^* \; v_{fl}^*]^T$ to the differential equation in Eq. (4.12) yields

$$\dot{Y} = A_c Y + B_c C_0^* r + B(U - U^*), \tag{4.13}$$

where

$$A_c = \begin{bmatrix} 0 & 1 & 0 & 0 \\ \frac{K_t}{J}\alpha_3^* & \frac{-b_\theta}{J} & \frac{K_t}{J}\alpha_1^* & \frac{K_t}{J}\alpha_2^* \\ \alpha_3^* & 0 & \alpha_1^* - \lambda_0 & \alpha_2^* \\ 1 & 0 & 0 & -\lambda_0 \end{bmatrix}, B_c = \begin{bmatrix} 0 \\ \frac{K_t}{RJ} \\ 1 \\ 0 \end{bmatrix}.$$

It is noted that the Lf term disappears in Eq. (4.13) because, as stated earlier, U^* is designed such that it cancels out the Lf term. The state space equation of the reference model can be written as

$$\dot{Y}_m = A_c Y_m + B_c C_0^* r. \tag{4.14}$$

Based on Eqs. (4.13) and (4.14), the error dynamics become

$$\dot{e} = A_c e + B(U - U^*), \;\; e_1 = C_c^T e, \tag{4.15}$$

where e_1 is the measured error. Let $U - U^* = \tilde{U}$. Since $\tilde{U}$ has two components: $\tilde{v}_{\text{MRAC}} = v_{\text{MRAC}} - v^*_{\text{MRAC}}$ and $\tilde{v}_{fl} = v_{fl} - v^*_{fl}$, the transfer function of the system presented in Eq. (4.15) will be a 2×2 diagonal matrix, with the {1,1} element being the transfer function between e and $\tilde{v}_{\text{MRAC}}$ and the {2,2} element being the transfer function between e and $\tilde{v}_{fl}$. To make the transfer function between e and $\tilde{v}_{\text{MRAC}}$ equivalent to the transfer function of the reference model, the matrix B in Eq. (4.15) must be transformed such that $B = \rho^* \bar{B}$, where $\rho^* = K_t/RJ$. Eq. (4.15) can be rewritten as

$$\dot{e} = A_c e + \rho^* \bar{B} \tilde{U}, \;\; e_1 = C_c^T e. \tag{4.16}$$

The transfer function $G(s)$ of the system is written as

$$G(s) = \rho^* C_c^T (A_c - Is)^{-1} \bar{B} = \begin{bmatrix} w_m & 0 \\ 0 & w_f \end{bmatrix}, \tag{4.17}$$

where w_m is the transfer function between e and $\tilde{v}_{\text{MRAC}}$, which is also equivalent to the transfer function of the reference model. w_f is the transfer function between e and $\tilde{v}_{fl}$, and is assumed to be stable. If this assumption is not satisfied, it could cause plant stability issues. Denote $\tilde{\alpha}$ as

$$\tilde{\alpha} = [\alpha_1 - \alpha_1^*, \alpha_2 - \alpha_2^*, \alpha_3 - \alpha_3^*, C_0 - C_0^*, \alpha_4 - \alpha_4^*, \alpha_5 - \alpha_5^*]^T, \tag{4.18}$$

where α_1, α_2, α_3, C_0, α_4 and α_5 are the control variables to be estimated. Define a Lyapunov function $\Omega(e,\tilde{\alpha})$ as

$$\Omega(e,\tilde{\alpha}) = \frac{e^T P_C e}{2} + |\rho^*| \frac{\tilde{\alpha}^T \Gamma^{-1} \tilde{\alpha}}{2}, \tag{4.19}$$

where Γ is a diagonal matrix with positive real elements. Assume P_c is a positive definite matrix and satisfies

$$P_c A_c + A_c^T P_c^T = -qq^T - v_c L_c, \;\; P_c \bar{B} = C_c, \tag{4.20}$$

where q is a vector, L_c is a positive definite matrix and $v_c > 0$ is a small constant. The time derivative of $\Omega(e,\tilde{\alpha})$ along the solutions of Eq. (4.16) is computed as follows:

$$\dot{\Omega} = -\frac{e^T qq^T e}{2} - \frac{v_c e^T L_c e}{2} + e_1^T \rho^* \tilde{U} + \tilde{\alpha}^T \Gamma^{-1} \dot{\tilde{\alpha}} |\rho^*|. \tag{4.21}$$

To make $\dot{\Omega}$ negative semi-definite, $\dot{\tilde{\alpha}}$ is chosen to be

$$\dot{\tilde{\alpha}} = \dot{\alpha} = -\Gamma \bar{e} \omega \text{sgn}(\rho^*), \tag{4.22}$$

where $\alpha = [\alpha_1, \alpha_2, \alpha_3, C_0, \alpha_4, \alpha_5]^T$, $\omega = [\omega_1, \omega_2, \theta, r, f_1, f_2]^T$, $\tilde{e} = \theta - \theta_m$. This approach was inspired by the Meyer-Kalman-Yakubovich (MKY) lemma (110). The overall control strategy is summarized below:

$$\begin{aligned} U = \alpha^T \omega, \;\; \dot{\omega}_1 = -\lambda_0 \omega_1 + i_{\text{MRAC}}, \\ \dot{\omega}_2 = -\lambda_0 \omega_2 + \theta, \;\; \dot{\alpha} = -\Gamma \bar{e} \omega \text{sgn}(\rho^*), \end{aligned} \tag{4.23}$$

where $i_{\text{MRAC}} = \alpha_{\text{MRAC}}^T \omega_{\text{MRAC}}$, $\alpha_{\text{MRAC}} = [\alpha_1, \alpha_2, \alpha_3, C_0]^T$, and $\omega_{\text{MRAC}} = [\omega_1, \omega_2, \theta, r]^T$.

If some parameters are known, then the above analysis becomes less complex, and the convergence rate would be faster.

4.4.2 Choice of Reference Signal r

The plant output θ would track the reference model output θ_m. However, the user can only select the reference signal r (108). The parameter of interest of the system

is the desired length of the TSA X, namely X_d. The reference input r should be designed such that it is a function of X_d. This can be accomplished in the following fashion: Firstly, θ_m is computed as a function of X_d using

$$\theta_m = \frac{\sqrt{L_0^2\left(1+\frac{\hat{F}_s}{\hat{K}_L}\right)^2 - X_d^2}}{w}. \tag{4.24}$$

Secondly, r is correlated to θ_m as follows:

$$r = \frac{1}{d_1}\dot{\theta}_m + \frac{d_2}{d_1}\theta_m. \tag{4.25}$$

It is noted that Eq. (4.25) works only when X_d is a smooth and continuous function. When X_d is not a smooth and continuous function (e.g., a step function), then r from Eq. (4.25) can be approximated as its value at steady state:

$$r \approx \frac{d_2}{d_1}\theta_m. \tag{4.26}$$

4.5 Simulation Results

4.5.1 Simulation Procedure

As a case study, the values of the motor parameters J, b_θ, L, R, K_t were selected as $9.7\times10^{-8}\,\text{kg.m}^2$, $7.6\times10^{-6}\,\text{kg.m}^2/\text{sec}$, $4.3\times10^{-4}\,\text{H}$, $9.21\,\Omega$, $14.6\times10^{-3}\,\text{N.m/A}$, respectively. The values of the string parameters K_L, K_w, L_0, w were selected as $9.98\times10^3\,\text{N}$, $11.7\times10^3\,\text{N}$, $0.2\,\text{m}$, $4\times10^{-4}\,\text{m}$, respectively (65). During simulation, the output voltage of the motor was limited to ±18 V. This was done to perform simulations close to practical scenarios. In addition, the following bounds were imposed on the parameter estimates to improve the performance of the estimation and control: $-50 \le \alpha_1 \le 50$, $-50 \le \alpha_2 \le 50$, $0 \le \alpha_3 \le 50$, $-50 \le \alpha_4 \le 50$, $-50 \le \alpha_5 \le 50$, $0 \le C_0 \le 50$.

4.5.2 Parameter Estimation

The following input voltage was applied to the system,

$$v(t) = 0.01\sin(0.5t) + 0.01\sin(t). \tag{4.27}$$

This input was chosen because it was sufficiently rich of order 4. To test the performance of the force estimator, the following axial force F_z was simulated:

$$F_z(t) = (5\sin(0.5t - \pi/2) + 5)\ \text{N}, \tag{4.28}$$

which implies that $\max(F_z(t)) = 10$ N and $F_z(t=0) = 5$ N. A sinusoidally varying force was chosen to demonstrate the estimator's ability to track varying unknown forces. In practical applications, it is common for the payload to be complex and difficult to predict or measure. The estimated and true axial force are shown in Fig. 4.3(a). The initial condition for the force estimate was $F_s/K_L(t=0) = 0$. γ_1 was selected to be a high value of 10^{10} to ensure fast convergence of $\hat{F}_s/\hat{K}_L$. Selecting a lower γ_1 value might slow down the estimation of $\hat{F}_s/\hat{K}_L$ and other system parameters. The force estimation error (Fig. 4.3(a)) was satisfactory because the error was small enough to have a negligible effect on the estimation of the other system parameters.

ϕ_2 was assumed to be measurable and was computed using $\hat{f}_1$ and $\hat{f}_2$. The estimates of the elements in ψ_2 converged to their true values, ψ_2^*, in around one minute. ψ_{2i} denotes the i^{th} element in the vector ψ_2. The estimation results for ψ_{21}, ψ_{22}, ψ_{23}, and ψ_{24} are shown in Fig. 4.3(b)-(c). In this simulation, the initial condition was $\psi_2(t=0) = 0$. As shown in Fig. 4.3(b), ψ_{21} and ψ_{22} oscillated around their true values before converging. ψ_{23} and ψ_{24} did not oscillate before reaching ψ_{23}^* and ψ_{24}^*, respectively. This was likely due to the choices of the initial condition of the adaptive gain matrix $P_2(0) = 10^{10} * diag[1,1,1,1]$, and the forgetting factor $\beta_2 = 1$. Another potential reason could be the fact that the magnitudes of $\hat{f}_1$ and $\hat{f}_2$ which

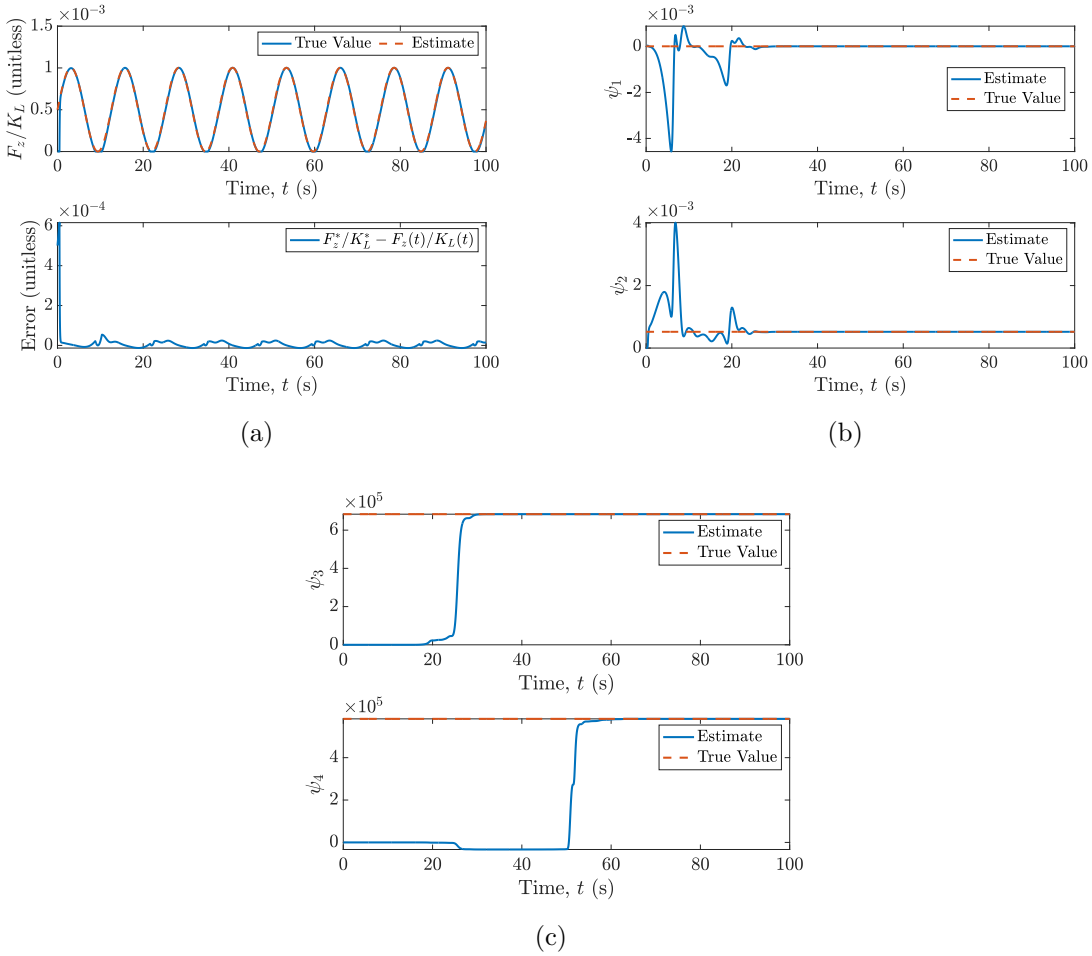

Figure 4.3: Estimation Results: (a) The time-varying estimate and true value of F_z/K, and the estimation error for F_z/K. (b) The convergence of ψ_{21} and ψ_{22}, which initially oscillate around the true values of ψ_{21}^* and ψ_{22}^*, respectively. (c) The convergence of ψ_{23} and ψ_{24} to ψ_{23}^* and ψ_{24}^*, respectively.

correspond to ψ_{23} and ψ_{24} were very low in comparison to the other two elements of ϕ_2. Therefore, ψ_{23} and ψ_{24} converged to their respective true values only after ψ_{21} and ψ_{22} converged. The convergence performance might vary based on $P_2(0)$.

4.5.3 Model Reference Adaptive Control

The parameters of the reference model were chosen so that the first-order transfer function would have a low time constant relative to the step response of the plant. This will not have adverse effects on the control performance for any choice of the reference signal. This was accomplished by setting high values for d_1 and d_2. In this work, $d_1 = d_2 = 1000$. This selection is based on the reasons mentioned in Section 4.4.1: To make the reference input equal the reference output at steady state, according to Eq. (4.26).

Without loss of generality, a force describe by Eq. (4.28) was applied to the TSA. A sinusoidal reference signal was selected to investigate the MRAC performance. The reference signal was defined in terms on the TSA's length. From the reference length, a reference motor angle was computed according to Eqs. (4.26) and (4.25), respectively. The sine wave was described as follows:

$$X_d = \frac{L_0 c}{2} \sin\left(15t - \pi/2\right) + L_0 \left(1 - \frac{c}{2}\right), \tag{4.29}$$

where X_d is the desired sinusoidally varying length, c is the desired maximum contraction, which is expressed as a ratio between 0 and 1. TSAs are typically able to achieve up to 30–40% contraction. Therefore, c was chosen to be $c = 0.3$. The phase offset of $\pi/2$ ensured that $X_d = 0$ when $t = 0$. λ_0 was chosen as 10^6 because it led to faster convergence of both the parameters and plant output during simulation. The adaptive gain $\Gamma = 0.2 * diag[1,1,1,1,1,1]$ was chosen to be a relatively low value because the scale of most of the parameters were small. α_4, for example, was on the order of 10^{-7}.

Fig. 4.4(a) shows r, θ_m, and θ_p. The plant converged to its reference signal in approximately 0.3 s. The fast convergence came at the cost of high disturbance in

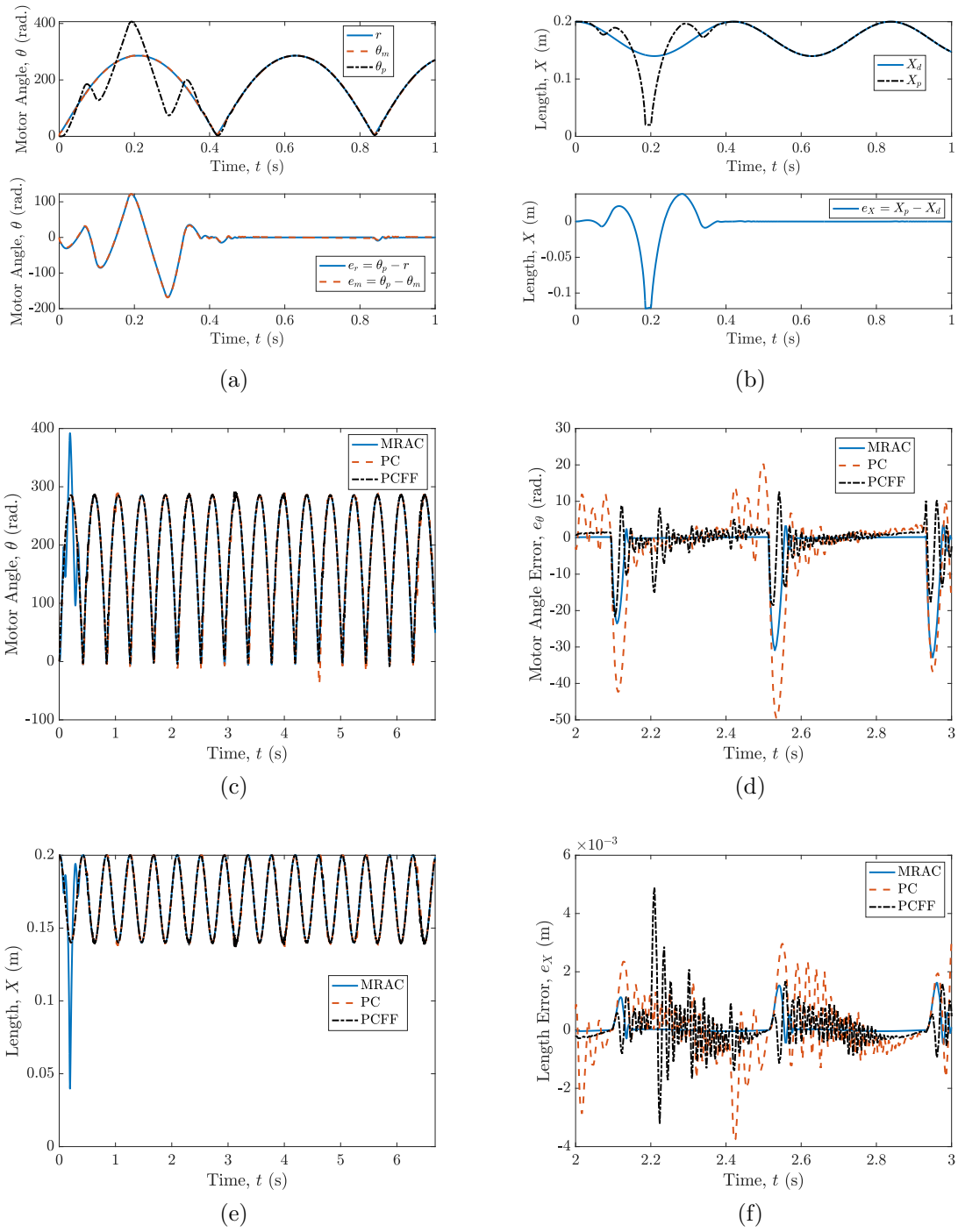

Figure 4.4: MRAC results with time-independent system parameters: (a) Motor angle results: desired versus simulated output and Motor angle control error. (b) The reference TSA length, output TSA length, and length control error. Comparison of (c) the motor angle results and (d) the corresponding control error with MRAC, proportional control (PC), and proportional control with feedforward (PCFF) strategies. Comparison of (e) the TSA length results and (f) the corresponding control error with MRAC, PC, and PCFF control strategies.

the initial stages. The tracking error for θ is provided in Fig. 4.4(a). Note that two signals are plotted in Fig. 4.4(a). The first signal, $e_r = \theta_p - r$, is the difference between the plant output and the reference model *input*. The second signal, $e_m = \theta_p - \theta_m$, is the difference between the plant output and reference model *output*. Because the dynamics of the reference model were fast, the differences between e_r and e_m were negligible.

The output TSA length, X_p and X_d, and the control error in terms of the TSA contraction are shown in Fig. 4.4(b). The high overshoot during $t < 0.3$ s was because the parameters of the controller had not yet converged. Because the relation between θ and X is static (not dynamic), the length converged to its setpoint at the exact same time that the motor angle converged to its setpoint. All parameters converged in approximately 2 s or less. The quick convergence of all six parameters led to accurate control performance. Similar results were obtained when a step reference signal was selected.

In addition, the performance of the MRAC when the system parameters, namely, K_L, K_r, J, and b_θ, varied linearly with time, was also examined. The aforementioned parameters varied according to the following equations:

$$\begin{aligned} K_L(t) = K_L(0) - 100 \times t, \;\; K_r(t) = K_r(0) - 100 \times t, \\ J(t) = J(0) + 10^{-8} \times t, \;\; b_\theta(t) = b_\theta(0) + 10^{-8} \times t, \end{aligned} \tag{4.30}$$

where, $K_L(0)$, $K_r(0)$, $J(0)$, $b_\theta(0)$, the initial values of the respective parameters, were the same as in Section 4.5.1. The respective rates of change were selected to simulate a slow variation with respect to time. The parameters varied for the first 10 sec of the simulation after which they remained constant. By varying the value of the stiffnesses K_L, and K_r, the value of the loaded untwisted length X_0 can be varied, which would help in simulating the effects of creep. Previous studies on TSAs have indicated the

existence of creep in their behavior (85). Furthermore, to simulate the effects of wear and tear in the motor, the motor parameters namely the inertia of the motor J and the motor's viscous coefficient b_θ were varied over time. Similar results were obtained, as shown in Fig. 4.4(c)–(f). Due the constraints on the control input in practical applications, varying the control parameters and system parameters might have a non-negligible effect on the performance of the system. This effect could be in the form of either unwanted oscillations in the system output or even instability of the system.

Furthermore, the controller performance was compared to PC and PCFF. These controllers were selected based on their prior selection in (108), and also due to their common usage. The PC was defined as $v_P = -K_p e_m$, where, v_P is the input using PC, and K_p is the proportional gain. The PCFF was defined as $v_{PCFF} = -K_p e_m + K_{FF}\dot{\theta}_m$, where, v_{PCFF} is the input using PCFF, K_p is the proportional gain, and K_{FF} is the gain for the feedforward. The gains of the aforementioned controllers were selected based on the initial guesses of the system parameters. The reference signal for this comparison is described by Eq. (4.29). The parameters of the system namely, K_L, K_r, J, and b_θ, varied linearly with time according to Eq. (4.30). In Figs. 4.4(c) and (e), the variation of θ_p and X_p are shown during the first 6.8 secs, respectively. As shown in Fig. 4.4(c)–(f), the system exhibited superior performance with MRAC as compared to PC and PCFF. The average TSA length control errors for MRAC, PC, and PCFF were 2.6×10^{-4} m, 0.0014 m, and 7.8×10^{-4} m, respectively.

CHAPTER 5

TWISTED AND COILED STRING ACTUATORS FOR LARGE STRAIN GENERATION

In this chapter, a novel actuation mechanism which enables TSAs to generate very high strains predictably and repeatably is presented. By applying the proposed actuation mechanism, uniform coil formation was obtained. The TSAs capable of generating additional actuation through coiling were named as twisted and coiled string (TCS) actuators. Furthermore, a procedure to systematically "train" the strings to ensure they achieve uniform coil formation was proposed. Experimental characterization of the proposed actuation mechanism in terms of output contraction, output contraction speed, input torque, and resistance-based self-sensing properties (for SCP-based TCS actuators). Experiments confirm that both stiff and compliant TCS actuators can achieve uniform coils at a wide range of loading conditions are presented. The chapter is concluded with discussions on the behavior of TCS actuators in the coiling phase and a robotic demonstration to show the effectiveness of the TCS actuators. The contents of this chapter are based on the findings presented in (111).

5.1 Motivation

The important performance metrics of a TSA are the contraction range, contraction speed, force output, torque input, bandwidth, and compliance. By utilizing a suitable pair of motor and strings, a TSA can be constructed to satisfy a given force output, bandwidth, and compliance requirement (9). However, one area that is independent of the components of a TSA and needs further improvement is the strain generation (relative to the initial string length). Compliance is essential in areas where safe

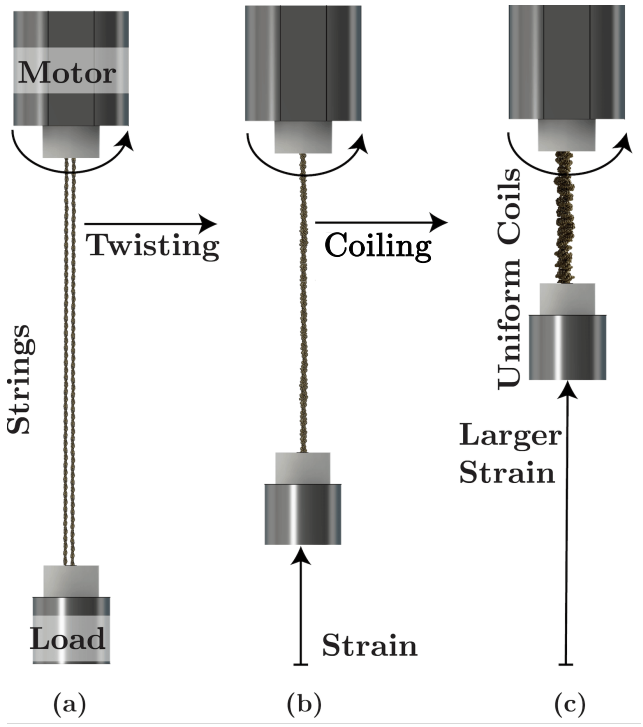

Figure 5.1: The (a) untwisted twisted and coiled string (TCS) actuator, (b) TCS actuator in the twisting phase, and (c) fully coiled phase.

interaction with human beings is demanded. Previous work used elastic strings in a TSA-driven robotic joint ([112]), whereas other work employed elastic SCP strings in TSAs ([41]; [40]). The inclusion of SCP strings in TSAs has the major advantage of resistance based self-sensing behavior ([41]; [40]). SCP strings have attracted much attention because they are compliant, lightweight, elastic, and often electrically conductive ([10]; [113]). The electrical resistance in SCP strings has been found to vary according to the strings' elastic deformation ([114]).

In sensing of the TSA, it is desirable to estimate its strain based on an electrical signal of the actuator. Unlike many other soft actuators, TSAs are unique in that the actuator only consists of two or more strings connected to a motor with no constraints on the type or material of strings. Therefore, replacing the typically adopted strings with conductive SCP strings could enable self-sensing TSAs. However, the

inclusion of SCP strings resulted in less strain compared to stiff strings: stiff string-based TSAs generate strain of up to 30–35% strain of their initial length, whereas SCP-based TSAs produce strains of around 20% of their initial length (40; 41). Although compliance and self-sensing are desirable, large strain generation is equally critical. Heating the SCP strings could result in additional strain of approximately 15% after they are fully twisted (making the total output strain around 35%) (41), but self-sensing while heating the strings has not been sufficiently studied because the electrical resistance is likely coupled with temperature, making the self-sensing behavior significantly difficult to characterize and model. Due to these reasons, the need for an alternative actuation mechanism which increases the strain output of the SCP-based TSAs, while not affecting their self-sensing capabilities, is strongly desirable.

In past studies, larger strains were obtained by "overtwisting" the strings—twisting beyond the regular twisting stage (Fig. 5.1(c)). In a study by Tavakoli et al., (107) with a two-string configuration, up to 72%-strains were obtained by overtwisting strings at loads between 2-kg to 5-kg (107). Although Tavakoli et al. claimed overtwisting to be advantageous, existing studies predominantly considered overtwisting to be undesirable (115; 116; 117; 35). This could be due to (1) increased nonlinearity and (2) the formation of non-uniform and unpredictable knots, entanglements, and coils in the overtwisted strings (39; 116; 117). In the study by Tavakoli et al., although large strains were generated using overtwisting, the formation of coils was considered to be undesirable: they were neither uniform nor consistent. Whereas the increased nonlinearity could be handled using advanced modeling techniques, the unpredictable non-uniform coil formation is most detrimental and undesirable. Firstly, the non-uniform coil formation accelerates the actuator's failure and causes unpredictable behaviors. Secondly, non-uniform coils occupy more space in the direction

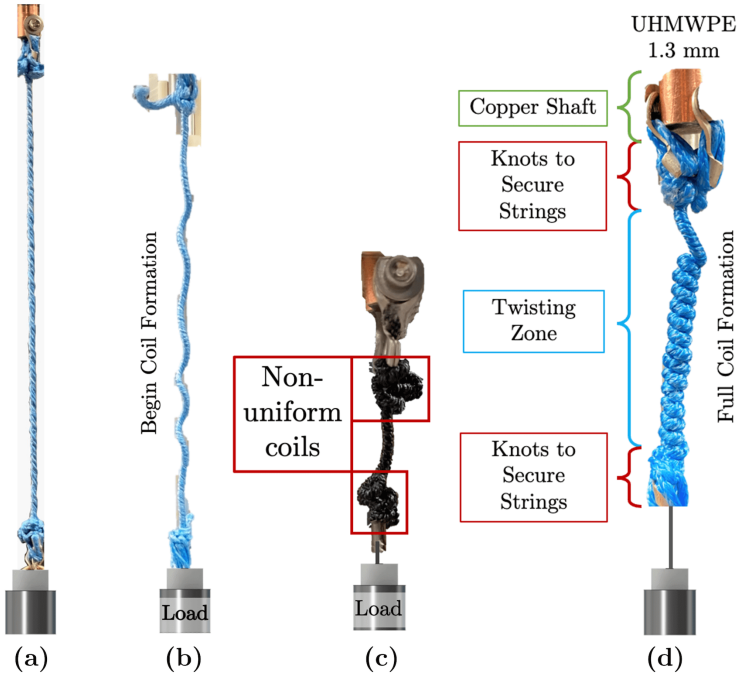

Figure 5.2: (a) The twisting phase. (b) The transition of the strings from the fully twisted state to the coiled state. (c) The non-uniform knots, entanglements, and coils that were formed in stiff TCS actuators when the TCS actuator was not pre-trained. (d) The uniform coils that were obtained by coiling trained TCS actuators.

perpendicular to the actuation direction relative to uniform coils. This could result in unwanted interaction of the strings with other system components (107). In the meantime, TSAs in general have attracted much attention in the robotics community, resulting in increased usage to power multiple advanced robotic and mechatronic devices (117; 35; 30; 36). It is thus strongly desirable to develop novel TSAs with increased strains. Overtwisting could be an efficient mechanism for large strain generation for TSAs when uniform coils are consistently obtained. However, no detailed studies have been conducted to realize uniform coils in overtwisted strings with high repeatability.

5.2 Fabrication of Twisted and Coiled String (TCS) Actuators

The proposed twisted and coiled string (TCS) actuator generates actuation in two phases of twisting: the twisting phase and coiling phase. In the twisting phase ([49; 27]), the two strings were twisted together such that they formed a tightly packed double helical structure. In the coiling phase, the tightly packed double helical structure then twisted to coil-like single (thicker) string. Uniform coils formed along its length, resulting in the formation of a tightly packed helical structure ([118]). It is noted that the proposed method is based on uniform coil formation upon coiling. The transition of the strings from a fully twisted state to the coiling state and an example of non-uniform coils are presented in Fig. 5.2.

5.2.1 Training Procedure

Experiments demonstrated that TCS actuators with unused SCP strings consistently produced uniform coils during coiling, but TCS actuators with unused stiff strings did not. Initially it was found that uniform coil formation in TCS actuators with stiff strings could be obtained only at sufficiently high loading conditions. This observation was consistent with previous studies on coil formation in artificial muscles ([42; 119]). However, uniform coil formation at lower loads—and thus a wider loading range—is desirable. Upon further investigation, the strings were found to exhibit repeatable and uniform coil formation through sufficient "training" at low loads.

The training procedure consisted of the following steps: Firstly, based on the strings' diameter, a physically feasible minimum load that ensured the strings to

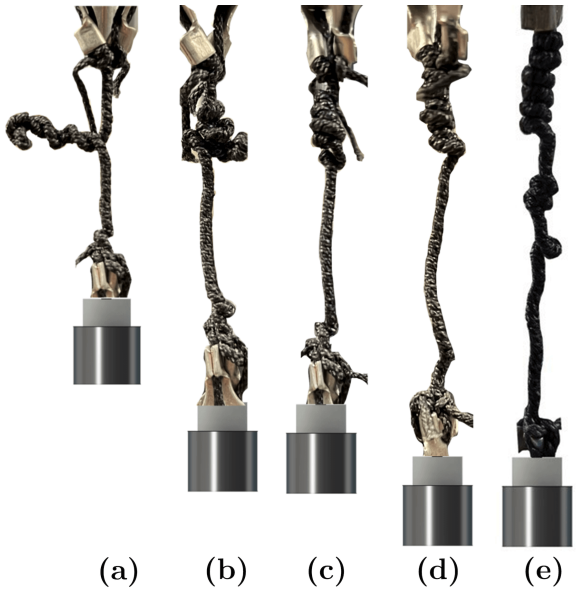

Figure 5.3: The evolution of the coiling structure of 1-mm UHMWPE strings during training. The coiling structure of the TCS actuator during the (a) 1^{st}, (b) 6^{th}, (c) 11^{th}, (d) 18^{th}, and (e) 50^{th} cycle.

be sufficiently taut was chosen. "Sufficiently taut" is a condition where, after fully twisted in the normal twisting phase, the strings can return to their initial state upon untwisting without requiring any additional external force besides the applied payload. In this study, it is assumed that if a particular load ensured that the strings were sufficiently taut during the normal twisting phase, then the load would also ensure sufficient tautness for the coiling phase. Secondly, at this load, the strings underwent twisting and untwisting cycles until uniform coils formed. 50 cycles were often sufficient to train the TCS actuator with stiff strings to generate uniform coils during coiling. As an example, the evolution of coil structure is shown in Fig. 5.3, for the TCS actuator with 1-mm UHMWPE strings under 200-g load. This evolution is described as follows: In the first stage, the coiling took place in the direction perpendicular to the linear actuation (Fig. 5.3(a)). In the second stage, some coils were formed along the length of the strings and remaining coils projected in the perpendicular direction (Fig. 5.3(b)). In the third stage, the coil formation started

taking place along the length of the strings, however, the coils' diameters were uneven (Figs. 5.3(c)-(d)). In the final stage, uniform coils formed inline with the strings of the TCS actuator (Fig. 5.3(e)). This procedure caused mild softening and gradual deformation of the strings into a helical shape. Although this deformation caused a slight decrease of the TCS actuator's operating length, it enabled the strings in each TCS actuator to consistently form uniform coils. Since the strings in TCS actuators were trained at the physically feasible minimum load, they were able to form uniform coils at higher loads as well. The training process is critical for stiff strings as it enabled them to achieve uniform coil formation upon coiling and consequently enabled stiff TCS actuators to attain high strains at wide ranges of loads.

Selection Physically Feasible Minimum Load:

In order to train a stiff TCS actuator, the strings should be loaded with a physically feasible minimum load that maintained the strings in a sufficiently taut state 'Sufficiently taut' is a condition where, after fully twisted in the normal twisting phase, the strings are able to return to their initial state upon untwisting without requiring any additional external force besides the applied payload. In this study it is assumed that if a particular load ensured that the strings were sufficiently taut for the normal twisting phase, then the load would also ensure sufficiently taut condition for coiling phase. The payload to ensure the strings to be taut is based on: 1) the inherent properties of the strings such as stiffness and braided structure (which causes friction between the twisted strings) and 2) the friction between the payload and slider. These factors affect the minimum load that ensures the strings to be sufficiently taut. The minimum payload was selected based on the following procedure: Firstly, for a given TCS actuator, a load of 100 g was initially used as payload. Secondly, the TCS

actuator was fully twisted in the normal twisting phase, then untwisted. Thirdly, if the attached payload ensured that the TCS actuator returned to its initial length after untwisting without requiring any additional external force, then this payload was labeled as the minimum payload. On the other hand, if an additional external force was required to make to the TCS actuator return to its initial length, then the payload was increased by 100 g and the process was repeated. For the purpose of this work, we used a load of 200 g for TCS actuators with 1-mm and 1.3-mm UHMWPE strings, and a load of 400 g for TCS actuators with 2-mm UHMWPE strings.

Determination of Maximum Number of Turns:

The angle was determined experimentally through trial and error process, not for each string-payload combination, but based on the string radius. The trial and error procedure was applied on the untrained strings, since even for training, the knowledge of maximum number of rotations was required. Each TCS actuator was loaded with a corresponding minimum payload which ensured the strings were sufficiently taut. Then, for each TCS actuator, to start with, 20 rotations were induced. From that point, the rotations were increased with a step size of 2 to determine the maximum number of turns such that 80% of the length of the contracted TCS actuator consisted of coils. The corresponding motor angle was recorded.

5.2.2 Uniformity of Coils

In this chapter, for stiff strings, uniformity of coils implied homogeneity of the coils. Homogeneity of coils suggests that all the coils have approximately the same size and shape. Although regularity of the coils is also an important criterion, it was relaxed

because during training of stiff strings, it was observed that while most coils were regular, there were few coils which formed at slightly irregular intervals (Fig. 5.3(e)). TCS actuators with compliant SCP strings did not require training to achieve uniform coil formation. This is likely due to their low stiffness and their supercoiled structure. However, even in SCP strings, while homogeneity of coils was observed, some coils formed with irregular spacing between them, similar to stiff strings.

5.2.3 Performance Metrics

In this work, the strain S of the TCS actuator is defined to be negative when the TCS actuator's length decreased, whereas the contraction C is the negative of the strain. The strain is expressed as

$$S = -C = \frac{(L - L_0)}{L_0} \times 100\%, \tag{5.1}$$

where L is the current length of the TCS actuator and L0 is the initial loaded length. For stiff TCS actuators, L_0 corresponded to zero motor rotations. Since the experiments with compliant TCS actuators began with the TCS actuator under 10 rotations, L_0 corresponded to 10 rotations.

5.3 Performance Characterization

5.3.1 Experimental Setup

The experimental setup used in this study is shown in Fig. 5.4. The TCS actuator was mounted vertically with a motor at the top, strings in the middle, and the load

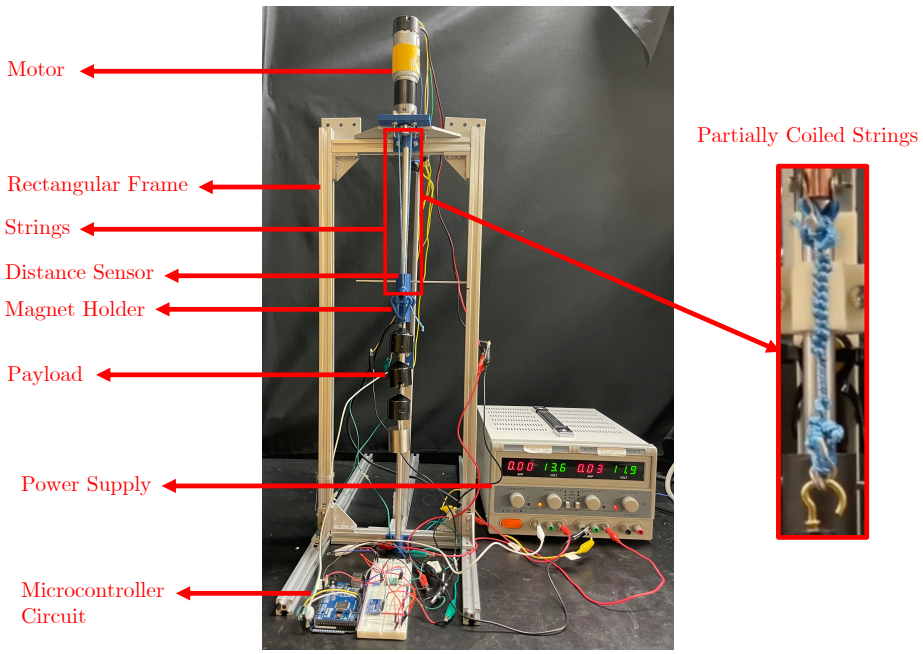

Figure 5.4: Experimental setup with the strings highlighted in the red box. The strings in their partially coiled state are also shown.

at the bottom. A DC motor (5202 Series Yellow Jacket Planetary Gear Motor with 50.9:1 Ratio, ServoCity) and driver (G2 High-Power Motor Driver 24v13, Pololu) were used. A carbon-fiber rod slid along the aluminum extrusions to constrain the bottom of the TCS actuator to vertical motion. A microcontroller (MEGA 2560 R3 Board, Elegoo) controlled the actuation and length sensing of the TCS actuator. The length of the TCS actuator was measured with an analog magnetoresistive position sensor (SPS-L225-HALS, Honeywell) with a resolution of 0.14 mm and sensing range of 225 mm. A 16-bit analog-digital converter (ADC) (ADS1115, Adafruit) digitized the analog signal of the sensor.

5.3.2 Procedure

Depending on the experiment, the input sequence was multiple cycles of twisting and untwisting. The motor rotated in steps of two rotations and paused for 2 s between each rotation. The maximum motor angle was determined experimentally depending on the TCS actuator's length and diameter. This angle was chosen as the angle at which approximately 80% of the TCS actuator was fully coiled; 100% coil formation increased the chance of breakage if the TCS actuator twisted additionally. The coil formation percentage denotes the percentage of length of the contracted TCS actuator that consisted of coils. In that sense, close to 100% coil formation refers to the scenario where coils are present along almost the entire length of the contracted TCS actuator. The TCS actuator cannot twist beyond the point where close to 100% of the length of the contracted TCS actuator consists of coils. This is why inducing additional twists at this point would result in the failure of the TCS actuator. When close to 100% of the length of the contracted TCS actuator consisted of coils, the strains generated by the TCS actuators were around 80% of their initial lengths. Twisting of the strings was achieved through clockwise motor rotations whereas untwisting was realized through counterclockwise motor rotations.

Experiments with stiff TCS actuators began at 0 rotations because length changes were evidently observed at any rotations greater than 0. However, experiments with compliant TCS actuators began with the TCS actuator twisted at 10 rotations: the corresponding length was nearly identical to the length of the TCS actuator at 0 rotations. This was because of the compliance and coiled structure of the SCP strings. With the space among adjacent coils of each SCP string, initial twisting of the two SCP strings around each other mostly filled the space between coils, but produced negligible contraction.

5.3.3 Stiff TCS Actuators

The TCS actuator with 1.0 mm, 1.3 mm, and 2.0 mm UHMWPE strings, which were loaded with 2000 g, 2900 g, and 3400 g, respectively, were used to experimentally study multiple properties of the coiling actuation mode. Beyond these loads, the TCS actuators were likely to fail, or the motor was likely to stall. Firstly, the strain generation was characterized for the stiff TCS actuators. The input sequence applied to the TCS actuator is presented in Fig. 5.5(a) and the corresponding strain of the stiff TCS actuator with 1.3 mm-diameter strings is presented in Figs. 5.5(b)–(c). The motor angle–strain relationship was mildly hysteretic, but the hysteresis was negligible in the twisting phase. This could be because of the strings' high stiffness and load. Similar trends were found for other stiff TCS actuators. In all cases, around 70% contraction was observed consistently (Figs. 5.5(b)–(c)).

Secondly, the actuation velocity of stiff TCS actuators was obtained. The actuation velocity of the stiff TCS actuator with 1.3 mm strings was calculated from the strain–motor rotations correlation in Fig. 5.5(b) and the velocity is presented in Fig. 5.5(d). For all the stiff TCS actuators, the actuation speed was significantly greater in the coiling phase than in the twisting phase. This implies that the bandwidth of the TCS actuator's strain is greater during coiling than during twisting.

Thirdly, the motor torque of the stiff TCS actuators was studied. This torque was computed by multiplying the current of the DC motor by the motor torque constant. The results of stiff TCS actuator with 1.3 mm-diameter strings are presented in Fig. 5.5(e). The results indicated that coiling in stiff TCS actuators required more torque than the twisting phase. A summary of the maximum contractions, actuation speeds, and required torques of different stiff TCS actuators are presented in Figs. 5.6(a)-(c), respectively. Numerical results are also presented in Table 1. Finally, a

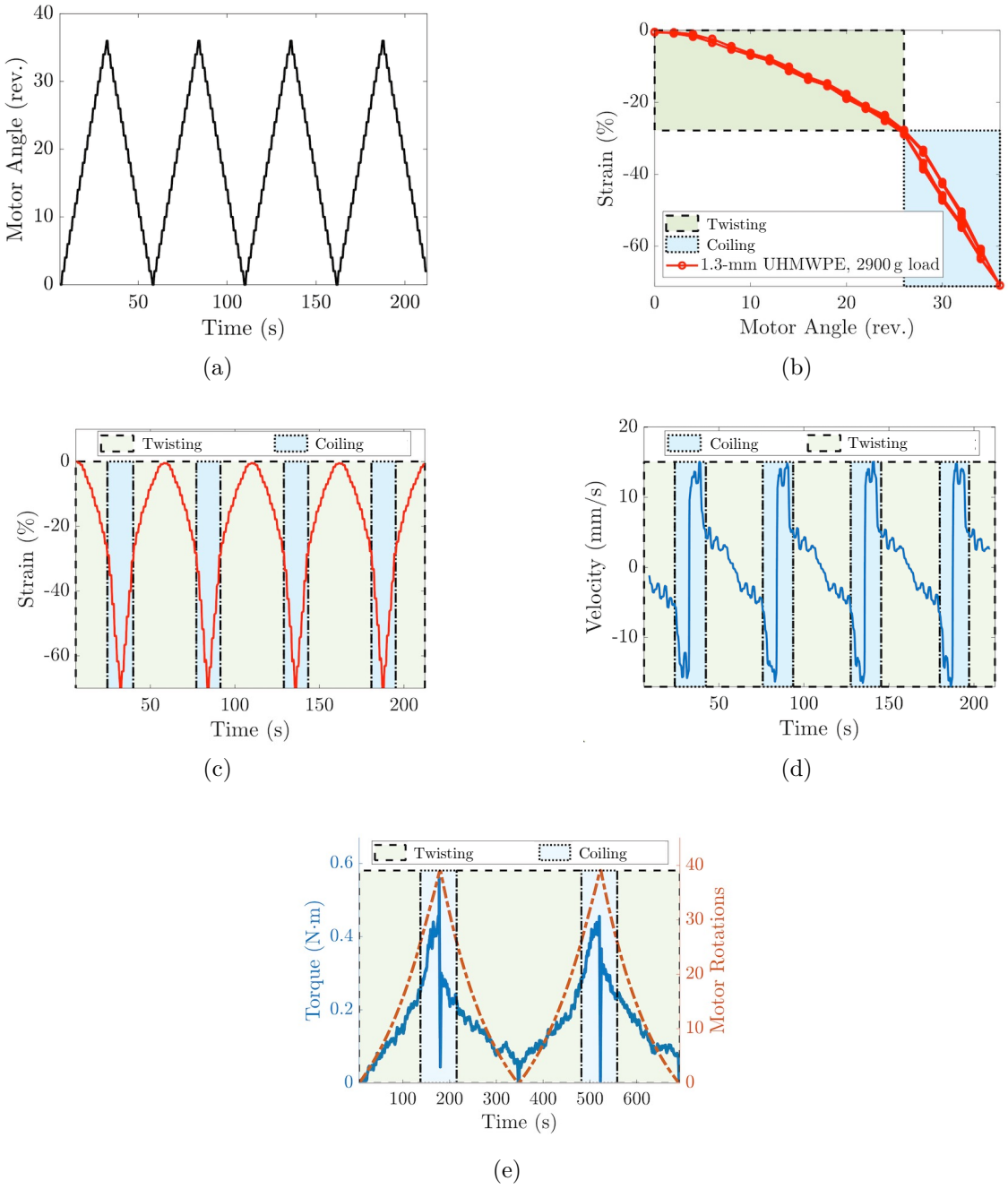

Figure 5.5: (a)—(e): Results obtained with 1.3-mm UHMWPE strings loaded with 2900-g. The areas of the twisting phase and the coiling phase are highlighted accordingly. (a) The motor angle input sequence versus time. (b) The correlation between strain and motor angle. The (c) strain, (d) velocity, and (e) input torque of the TCS actuator versus time. Note that in (e), a motor angle input sequence with low angular velocity was utilized to decrease the noise in the torque measurement.

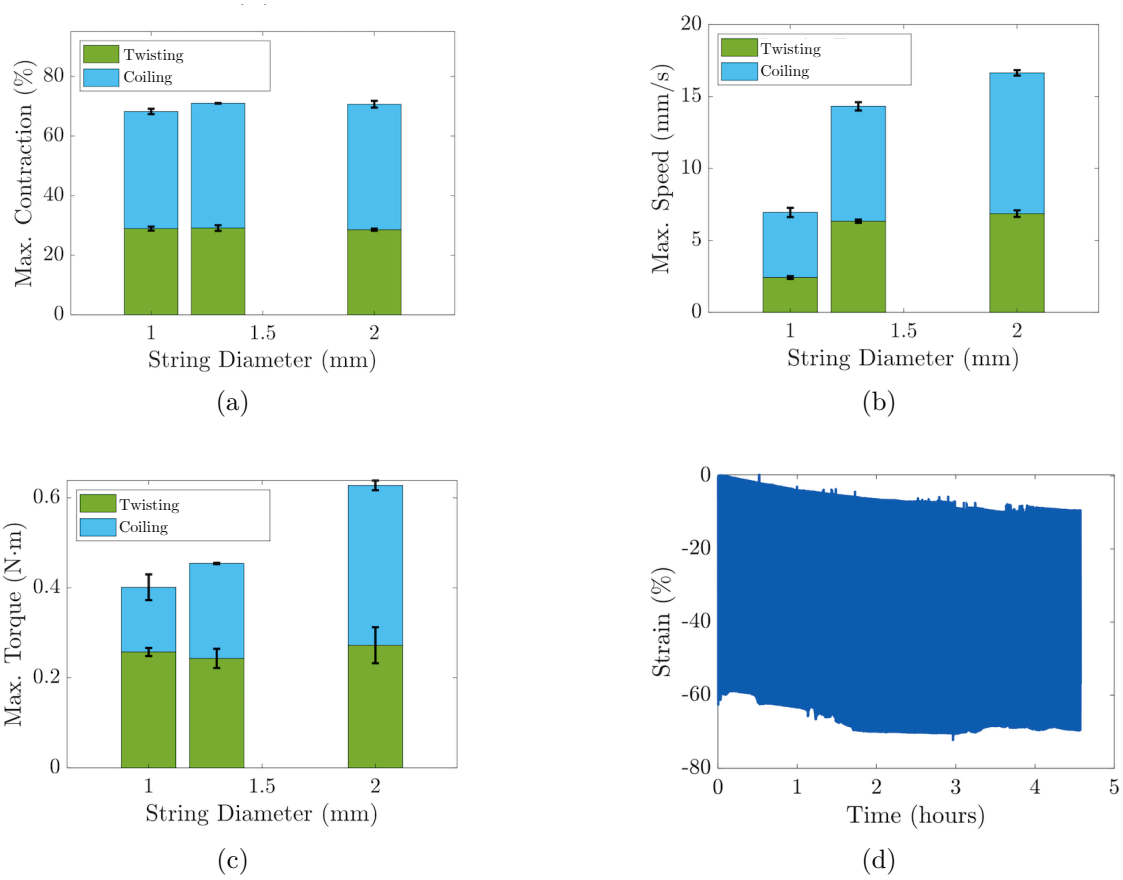

Figure 5.6: (a)—(c): The comparison of results for UHMWPE strings with different diameters. Error bars are shown in black in each plot. The error bars represent the standard deviation of the maximum attained values over four cycles. The heights of the bars denote the maximum values that were averaged over four cycles. The (a) maximum contraction, (b) maximum speed, and (c) maximum input torque of the TCS actuators in the twisting and coiling phases. (d) A test of the TCS actuator's lifetime by measuring the strain versus time for 1.3-mm UHMWPE strings.

test of the TCS actuator's lifetime was conducted (Fig. 5.6(d)). A TCS actuator with 1.3 mm-diameter UHMWPE strings under 2900 g of load was used. The motor rotated with five-rotation steps and a 200 ms pause between each rotation. The TCS actuator lasted for 1030 cycles without breaking. The TCS actuator consistently achieved approximately 60% contraction. Although the overall length of the TCS actuator slightly decreased over time, the linear actuation range remained approximately constant between all cycles. The strings also gradually deformed into a

helical shape. Consequently, the length of the TCS actuator decreased, as verified by the creep-like behavior in Fig. 5.6(d). As the experiment ran, the number of coils that formed along the length of the strings also increased. Furthermore, while the generated strain changed initially due to the decrease in length of the strings, after approximately 2 hours from the beginning of the test, the strain did not further increase and was consistent.

5.3.4 Compliant TCS Actuators

As an example, the strain and self-sensing of 6-ply SCP based-TCS actuator under a 200 g load is considered. As shown in Figs. 5.7(a)–(b), the TCS actuator repeatably achieved 11.25% strain in the twisting phase, then an additional 46.89% in the coiling phase. The relationship between twists and strain distinctly revealed the twisting and coiling phases of the TCS actuator, as shown in the two hysteresis loops in Fig. 5.7(b). Compliant TCS actuators demonstrated greater hysteresis than the stiff TCS actuators in both the twisting and coiling phases, mainly due to the friction and material properties of SCP strings. Because the TCS actuator was fabricated from conductive SCP strings, the electrical resistance of the strings was measured. Transient decays in the electrical resistance were observed (Fig. 5.7(c)), similar to transient resistance behaviors in other materials (90; 91). The results suggest a correlation between the strain and resistance of the TCS actuators, which could be used for strain self-sensing. The resistance experienced mild creep as time increased, which was likely due to the friction between the strings that rubbed the silver coating off of them (40).

A summary of the maximum repeatable contractions for the compliant SCP-based TCS actuators is shown in Fig. 5.7(d). The strains achieved by SCP-based TCS

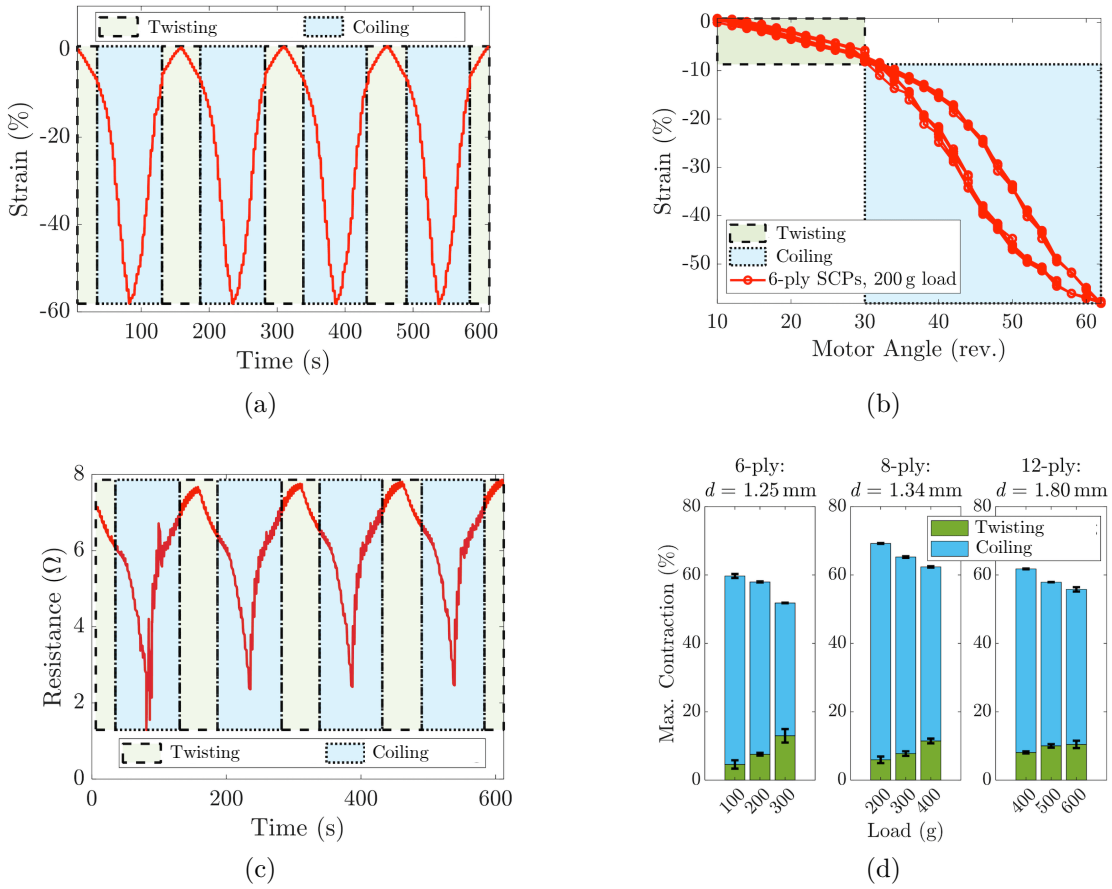

Figure 5.7: The experimental results for the compliant SCP-based TCS actuators. The data presented in (a)–(c) was for 6-ply SCP-based TCS actuator with a 200-g load. (a) The variation of strain in time. (b) The length-motor angle (turns) correlation. (c) The variation of resistance in time. (d) The maximum repeatable contractions obtained in compliant SCP-based TCS actuators.

actuators in twisting phase were less than those achieved by stiff TCS actuators mainly because the SCP strings are compliant and stretchable.15 Increased loads generally decreased the maximum attainable contraction (Fig. 5.7(d)). Furthermore, as the load increased, the contraction obtained through twisting increased but the contraction obtained through coiling decreased.

The lifetime endurance was also examined in the compliant TCS actuator. Two tests were conducted with different pairs of 6-ply SCPs loaded with 100 g. On the

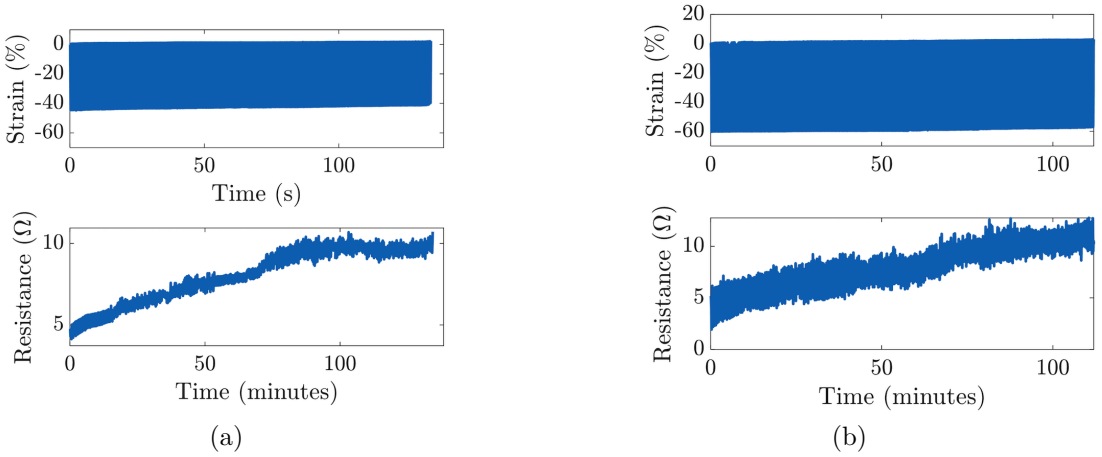

Figure 5.8: (a)–(b) The strain and electrical resistance of the compliant SCP-based TCS actuator over time. (a) For 428 complete cycles, the maximum contraction consistently reached approximately 45%. (b) For 285 cycles, the TCS actuator achieved consistent strains of approximately 60%

first test, the TCS actuator lasted for 285 cycles with consistent 60% contractions but broke on the 286th cycle (Fig. 5.8(a)). On the second test, the TCS actuator lasted for 428 cycles and achieved consistent contractions of 45% (Fig. 5.8(b)). For both tests, the resistance demonstrated creep over time. This could be due to the friction between the strings that rubbed the silver coating off them. The TCS actuator in the second test achieved less contraction and less resistance change because the maximum twisting angle was smaller.

5.4 Robotic Demonstration

TCS actuators have great potential in robotic exoskeletons ([33]; [48]), assistive devices ([52]; [51]), tendon-driven robotic fingers and manipulators ([37]; [120]; [121]), and other robotic structures. In this paper, a TCS actuator-driven robotic bicep demonstrated the effectiveness of TCS actuators. 1.3-mm UHMWPE strings were used. The de-

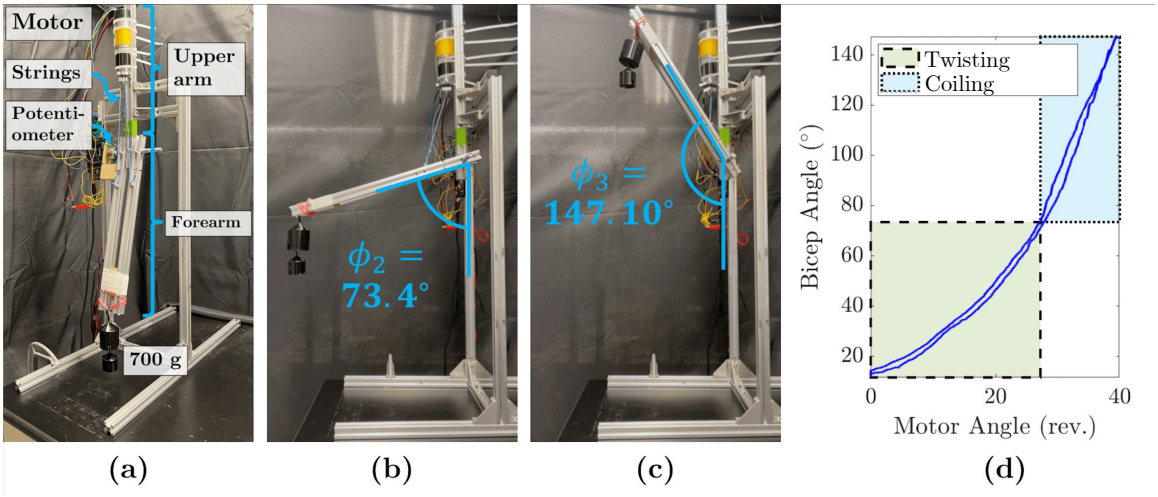

Figure 5.9: (a) Robotic bicep actuated by TCS actuator with UHMWPE strings having diameter of 1.3-mm. (b) Position of the forearm at the end of twisting phase. (c) Position of the forearm achieved through coiling. (d) The bending angle versus motor rotations for the robotic bicep.

vice was selected to demonstrate the effectiveness of the proposed mode of actuation because it has been employed by other similar works (70) to demonstrate the capabilities of novel soft actuators and artificial muscles. Furthermore, the robotic bicep is different from the weight-lifting setup used for experimental characterization because the tension force experienced by the strings changes as the bicep angle changes. This application therefore shows the enhanced strain and force outputs of the TCS actuators simultaneously. The robot was constructed using three metallic rods. The first rod (the stationary link, labeled as the upper arm in Fig. 5.9(a)) was suspended vertically from a metallic frame. The other two rods were assembled parallel to each other and formed the movable link, labeled as the forearm in Fig. 5.9(a). One end of the forearm was attached to the bottom of the upper arm by a revolute joint. The free end of the forearm was loaded with 700-g. A potentiometer at the joint measured the bending angle relative to the initial position of the forearm (Fig. 5.9(a)). The TCS actuator was installed with the motor attached to the upper arm and the bottom of the strings attached to the forearm. The initial angle was $\phi_1 = 13.1°$. Whereas

twisting of the TCS actuator resulted in a maximum bending angle of $\phi_2 = 73.4°$ ($\phi_2 - \phi_1 = 60.3°$, Fig. 5.9(b)), coiling resulted in the maximum bending angle of $\phi_3 = 147.10°$ ($\phi_2 - \phi_1 = 73.7°$, Fig. 5.9(c)). The bending angle versus motor rotations is presented in Fig. 5.9(d). The untwisted, fully twisted, and coiled lengths of the TCS actuator were 21.5 cm, 13.5 cm, and 6.8 cm, respectively.

5.5 Discussions

5.5.1 Interpretation of Performance Results

In order to achieve consistent and repeatable actuation upon coiling, the strings of the TCS actuators had to be trained. However, the training process does not necessarily increase the complexity of the proposed mode of actuation as the training procedure was simple and straightforward, and does not depend heavily on the external conditions such as applied load. For example, in the current work, the training procedure was applied when the strings were subjected to a physically feasible minimum load, which was determined experimentally based on the 'sufficiently taut' condition. This was done to demonstrate a general case of training the TCS actuator. This load can be greater than the physically feasible minimum load, as long as the strings are kept taut, and the exact amount of load can be decided by the user. Therefore, the increased actuation range caused by the proposed mode of actuation and the advantages pertaining to it, outweigh the requirement of the training the strings before using them in a given application.

The periodic motion was selected as an input for experimental characterization because of its repeated usage in similar work ([27; 40]). Due to their nonlinear gear

ratio, the actuation velocity of TCS actuators increases with increasing number of twists. Periodic input sequence, such as the one used in this work, enables better characterization of such velocity trends. When a more general input sequence is applied, the response of the actuators would be similar to its response to periodic motion, as long as the input sequences are within the bandwidth of the actuator. Systematically studying the response to non-periodic motion is beyond the scope of this study due to the following consideration: To comprehensively characterize the increased hysteresis during the coiling region, sufficiently rich input signals which guarantee persistent excitation of the actuator are required (102). Applying such complicated inputs is useful when attempting to model the behavior of the actuator, which is beyond the scope of this study.

An important performance metric which was not considered in this work was the bandwidth of TCS actuators. Bandwidth of the TCS actuator can be determined by studying its frequency responses. Based on the existing data, the following qualitative analysis on the frequency response can be presented: The frequency response of the TCS actuator would highly depend on the frequency response of the motor used in the TCS actuator. Since the TCS actuators generate more contraction with coiling as compared to TSAs, the bandwidth of the TCS actuators is expected to be slightly lower than the bandwidth of the TSAs. This is because TCS actuators require more motor rotations than TSAs to achieve their respective maximum strains. If the TCS actuators in the twisting phase and coiling phase are compared individually, then it can be concluded that the bandwidth of the TCS actuator in the coiling phase will be greater than the bandwidth in the twisting phase. This is due to the nonlinear gear ratio, varying linear actuation speed, and motor rotation range of the twisting and coiling phases. For constant motor speed, the linear actuation speed increases with as the strings twist more. Therefore, since the actuation speed of the TCS actuator

in the coiling phase is greater than that in the twisting phase, the bandwidth of the TCS actuator in coiling phase (assuming the TCS actuator oscillates without exiting the coiling phase) will be greater than the bandwidth in twisting phase.

However, systematically studying the frequency response of the proposed actuation mechanism is beyond the scope of our study due to the following reason: The frequency response of the actuator is based on its ability to track sinusoidal signals of different frequencies (9). Furthermore, for a system to track a desired signal, a mathematical model of its behavior is often necessary. Since linear systems generate sinusoidal outputs in response to sinusoidal inputs, their frequency responses can be obtained without the knowledge of the model which describes their behavior. However, to obtain the frequency response of nonlinear systems such as TCS actuators, knowledge of their input–output correlations is required (108; 49; 122). Due to the nonlinear gear ratio of the TCS actuator, the contraction and speed of the actuator vary non-linearly with the motor rotations. This implies that for a TCS actuator to generate a desired motion, the correlation between the motor rotations and contraction is required. These relations are known for twisting phase due to which the bandwidth of TCS actuators in twisting phase which is the same as the actuation of a TSA is well studied (108; 49; 122). However, the aforementioned relations are not derived for the coiling phase of the TCS actuators. Developing and verifying the physics-based models that describe the static behavior of the TCS actuators in coiling phase is presented in Chapter 7, whereas deriving models which describe the dynamic behavior of the TCS actuators is beyond the scope of this study. However, we plan on addressing these issues as a part of future work. Therefore, once the models are developed, the frequency response of the actuator in the coiling phase will be obtained.

5.5.2 Potential Impact

The TCS actuators exhibit smaller force outputs in the coiling phase compared to the twisting phase. However, the force generation of TCS actuators in coiling phase is still advantageous over popular artificial muscles such as SCP actuators, SMA actuators, and SMTAs ([9]; [123]). Therefore TCS actuators are highly suitable for applications which demand compact actuation mechanisms with high force outputs, even considering the decreased force output during the coiling phase. However, their application in soft robots, and exoskeletal technology has been limited due to their limited strain generation capability. Therefore, by the virtue of increasing their strain outputs, TCS actuators are more suitable in such applications.

The proposed TCS actuators exhibit significantly more strain generation than TSAs, which increases their impact in the field of robotics, more specifically in applications demanding high force and compact actuators, such as robotic exoskeletons ([124]; [48]), tendon-driven robotic fingers and arms ([37]), and other robotic structures ([43]; [33]). Large strains generated through coiling could result in the realization of compact solutions in areas that demand large displacements. For example, consider a robotic device like the one presented in Hosseini et. al. ([48]), which requires displacements of 10-mm. To meet this requirement, if only twisting is employed (with up to 30% contraction), then a TSA with a length of approximately 33-mm would be required. However, with coiling (with up to 70% contraction), a TCS actuator with a length of only 14.3-mm would be sufficient. This would effectively reduce the untwisted strings of the actuator to less than half of their original length. Even in the coiled phase, the twisted strings only mildly increased in diameter, which still allows the actuator to be conveniently placed in conduit or a sheath for wearable and assistive devices ([52]; [51]). For example, a TCS actuator made from two 6-ply SCP

strings and loaded with 200-g hanging weight had a diameter of 2.1-mm in the twisting phase and only 3.6-mm in the coiling phase. The uniformly coiled strings can also be put into bending actuators (10), and then can be further incorporated into different robotic applications. Furthermore, soft robotic structures, such as soft bending fingers (19), could be realized using compliant TCS actuators. Such devices would be able to generate larger forces and quicker actuation while maintaining compliance and compactness.

5.5.3 Limitations

Some evident limitations of the proposed mode of actuation are as follows: Firstly, the uniform coil formation, while enabling a stable and repeatable behavior, resulted in jerky motion due to formation of coils. Although the coils were uniform, every time a new coil was formed, the string would intermittently contract at a faster rate. This may generate unwanted oscillations of the payload attached to the string. Secondly, the proposed coiling mechanism increased the nonlinearity of the actuator. Hysteresis in the twisting phase of TCS actuators and particularly compliant TCS actuators made with SCP strings has been recently studied in our previous work on compliant TSAs (41; 40). Our previous study on self-sensing SCP-based TSAs showed that the length-resistance correlation is not only hysteretic but also contains creep and transient decay (40). While the hysteresis in compliant TCS actuators is significant, stiff strings have relatively less hysteresis. This may be due to the high stiffness of the strings. Furthermore, previous studies indicate that even in the twisting phase, TCS actuators exhibit hysteresis (27). In addition it was observed that the hysteresis in the coiling phase became less significant with increasing payload. This was observed in both stiff and compliant TCS actuators.

Hysteresis is an extensively studied nonlinearity in the robotics and mechatronics community. To capture hysteresis, both physics-based methods and phenomenology-based approaches, such as the Preisach operator, Prandtl-Ishlinskii model, and Bouc-Wen model, have been proposed ([70]; [89]; [125]; [83]). Furthermore, different control schemes like feedforward control, proportional–integral–derivative control, robust control, and adaptive control have been realized ([68]; [78]; [79]; [81]). In addition, the actuator also exhibited creep-like behavior as can be inferred from Fig. 5.6(d). Previous studies on TCS actuators with twisting have hinted creep-like behavior which was observed in the current study as well ([85]). Creep is a common nonlinearity found in many artificial muscles and smart materials, which does not make the actuator unstable if treated appropriately. Like hysteresis, creep has been extensively modeled in previous work ([126]; [127]). Those models could apply to coiling as well.

Lastly, compliant TCS actuators exhibited low lifetimes in comparison to stiff TCS actuators. This is mainly due to the inherent limitations of SCP strings: The coiled structure of the SCP strings resulted in increased frictional forces between the strings when twisted and coiled. Consequently, the wear and tear of the strings increased which led to their early failure. Meanwhile, the self-sensing realized by using conductive strings is an important concept because of the compact sensing achieved through it. The lifetime of compliant self-sensing TSAs can be potentially enhanced by using robust stretchable conductive strings.

CHAPTER 6

EXPERIMENTAL INVESTIGATION OF THE NON-SMOOTH HYSTERETIC ACTUATION IN TWISTED AND COILED STRING ACTUATORS

In this chapter, a comprehensive experimental characterization of the TSA actuation in the coiling phase will be conducted. Firstly, the load dependence of the TCS actuators' behavior is examined by applying input cycles under different loading conditions. Secondly, the non-smooth behavior is investigated by using sequences of input motor turns with different frequencies. Lastly, the hysteretic behavior and the properties of transitioning conditions are examined by applying different ranges of the input cycles under different loading conditions. The chapter is concluded with discussions on the implications of the experimental investigation. The contents of this chapter are based on the findings presented in (128).

6.1 Motivation

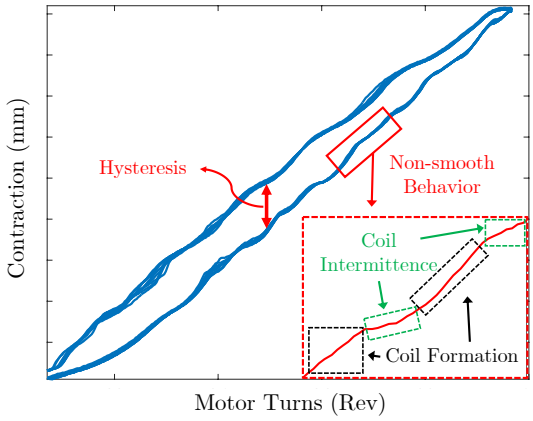

Figure 6.1: The behavior of TCS actuators in the coiling phase, comprising of hysteresis and non-smooth behavior. The non-smooth contraction is highlighted with the coil formation and intermittence instances labeled.

While experimental characterization of the TCS actuators in coiling phase in terms of output contraction, output contraction speed, and input torque, was presented in Chapter 5, few critical aspects of the TSA actuation in the coiling phase were not sufficiently studied: Firstly, the experimental characterization presented in chapter 5 was restricted to the analysis of steady-state properties of the actuation in the coiling phase. Secondly, the results presented in Chapter 5 indicated that in comparison to the actuation in the regular twisting phase, evident hysteresis appears in the actuation in the coiling phase, likely due to large friction between strings when coiled (Fig. 6.1). However, the dependence of hysteresis on the operating conditions was not studied in detail. Lastly, most experiments in chapter 5 were performed at a constant load. The dependence of the actuation on the applied payload was not sufficiently investigated. The non-uniform actuation resulting from the coiling-based actuation may not be desirable in applications demanding smooth actuation such as exoskeletal devices (33), and soft robotic manipulators (44). Furthermore, other aspects of the actuation mentioned earlier in this paragraph also need to be studied thoroughly to further establish the coiling process as a reliable mode of actuation for TCS actuators.

To motivate this study, results of preliminary experimental characterization are presented and discussed in this section. The input sequence used for the characterization was a triangle wave with four cycles. It is noted that the range of the input sequences was [0 40] turns. This was done to present and qualitatively compare the behavior of TCS actuators in both twisting and coiling phases thereby revealing the unique properties presented by the actuation in the coiling phase. It is known that the point of transition where the TCS actuators switch from coiling phase to twisting phase is defined as the number of motor turns where the last coil dissipates (111). From the obtained results (Fig. 6.2), the point of transition for the TCS actuator considered in this study, was identified as 27.9 turns. Without loss of generality, the

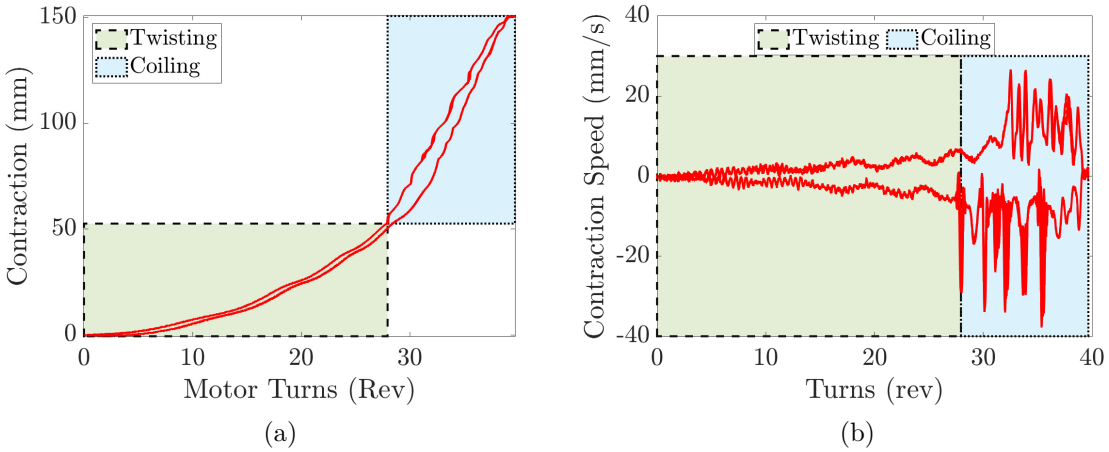

Figure 6.2: Experimental characterization results: (a) Motor turns – contraction correlation. The twisting and coiling phases are highlighted separately. (b) The contraction velocity plotted as a function of the motor turns.

motor was run at 1.2 rev/sec speed and a payload of 800 g was attached to the TCS actuators. The results revealed two distinct behaviors namely non-smooth actuation and hysteresis. Hysteresis is a common phenomenon found in numerous popular artificial actuators and has been extensively studied over the past years ([71]). However, the non-smooth actuation is relatively scarce and appears in TCS actuators due to its coiling-based actuation mechanism: Unlike other linear actuation mechanisms, the coil formation phenomenon is a discontinuous process with coil formation occurring at specific values of motor turns.

6.1.1 Non-smooth Actuation

While the actuation in the twisting phase is relatively smooth, actuation in the coiling phase exhibits non-smooth behavior (Fig. 6.1). This is mainly because, in the coiling phase, actuation is realized by TCS actuators through the formation of coils along their length. Twisting of strings in the coiling phase generates drastic contraction

accompanying larger non-smooth actuation during coil formation instances as compared to the intermittence between adjacent coil formations. This phenomenon is revealed in experimentally obtained motor turns – contraction relationship presented in Fig. 6.1, where the coil formation and coil intermittence instances are highlighted.

While the non-smooth component of actuation seems to be mild in Fig. 6.2(a), it has adverse effects on the contraction speed of the TCS actuators. As shown in Fig. 6.2(b), the speed profile of the TCS actuators becomes highly non-smooth in the coiling phase as compared to the speed profile in the twisting phase, which is not desirable in many applications which demand uniform and smooth motion. The spikes in the speed profile have varying magnitudes at different instances of coil formation (Fig. 6.2(b)). In addition, the non-smooth behavior shown in Fig. 6.2(b) also shows non-symmetric behavior for a symmetric motor turns input.

6.1.2 Hysteresis

Hysteresis is a common phenomenon found in a variety of smart materials, elastic materials, and ferromagnetic materials (83; 72). Fig. 6.2(a) reveals that while hysteresis was present in both phases of actuation, the hysteresis in the coiling phase was more significant in comparison to the hysteresis in the twisting phase. Previous studies report hysteresis in the twisting phase as well (85). As Fig. 6.2(a) shows, under a symmetric motor turns input, the contraction output was not symmetric. The quasi-static relationship between motor turns and contraction showed evident hysteresis in the coiling phase, as found in our previous work (111). Whereas determining the cause of increased hysteresis in the coiling phase is beyond the scope of this study, the increased friction between the strings and the coils could be a potential reason.

6.2 Fabrication of TCS actuators

This study utilized two strings with the same length and material properties to construct the TCS actuators. The strings were hung vertically in tension with a hanging mass attached to their bottom ends. The other ends of the strings were connected to a motor. The bottom of the strings were constrained such that the load moved linearly due to the motor's rotation. UHMWPE strings with diameters of 1.3 mm and a length of 210 mm, were used due to their repeated usage in relevant literature (27; 49). The TCS actuators are required to be trained to exhibit repeatable actuation through uniform-coil formation. The training procedure consisted of the following steps: Firstly, a load of 200 g was selected for training because this was the minimum load which ensured the strings to be sufficiently taut (111). Secondly, at this load, the strings underwent twisting and untwisting cycles until uniform coils formed. 50 cycles were sufficient to train the TCS actuators to generate uniform coils during coiling phase. Readers are referred to (111) for more details on the training process of TCS actuators.

6.3 Experimental Characterization

Three sets of experiments were conducted to investigate the different aspects of the TCS actuators' behavior. The experimental setup used to collect data for analysis was the same as the one described in Section 5.3.1.

6.3.1 Load Dependence

The first set of experiments addressed the effect of the applied payload on the behavior of the TCS actuators. It is noted that full actuation of the TCS actuators was considered. Preliminary experiments showed that the point of transition of the TCS actuators varied based on the applied payload. To further investigate this phenomenon, the following experiments were conducted. The input sequence applied to the actuators was restricted to range between 0 turns and 40 turns. The upper bound was selected to ensure that no damage was caused to the TCS actuator. As a part of this study, ten sets of experiments were conducted to investigate the load dependence of the TCS actuators' behavior. For each set, an input sequence consisting of four triangular waves was applied to the actuators (Fig. 6.3(a)). Four input cycles were applied to ensure the repeatability of the motion. Without loss of generality, the speed at which the motor rotated was selected to be 0.12 rev/sec. The applied payload ranged between 200 g and 1100 g, and was varied for each set with an increment of 100 g.

The experimental results are presented in Fig. 6.3(b)–(l). As it can be inferred from Fig. 6.3(b)–(k), the point of transition increased with the applied payload. It is worth mentioning that the behavior of the TCS actuators when the rate of input is positive (twisting), was mostly consistent. However, the TCS actuators' behavior exhibited relatively lower repeatability for a negative input rate (untwisting) at different loads. This is further validated by Fig. 6.3(l) which shows the variation of the number of turns where the first coil forms and the point of transition, where the last coil dissipates with the applied payload. These points were extracted by the motor turns – contraction correlation using the following procedures: When the input rate is positive, the point where the non-smooth behavior appears for the first time

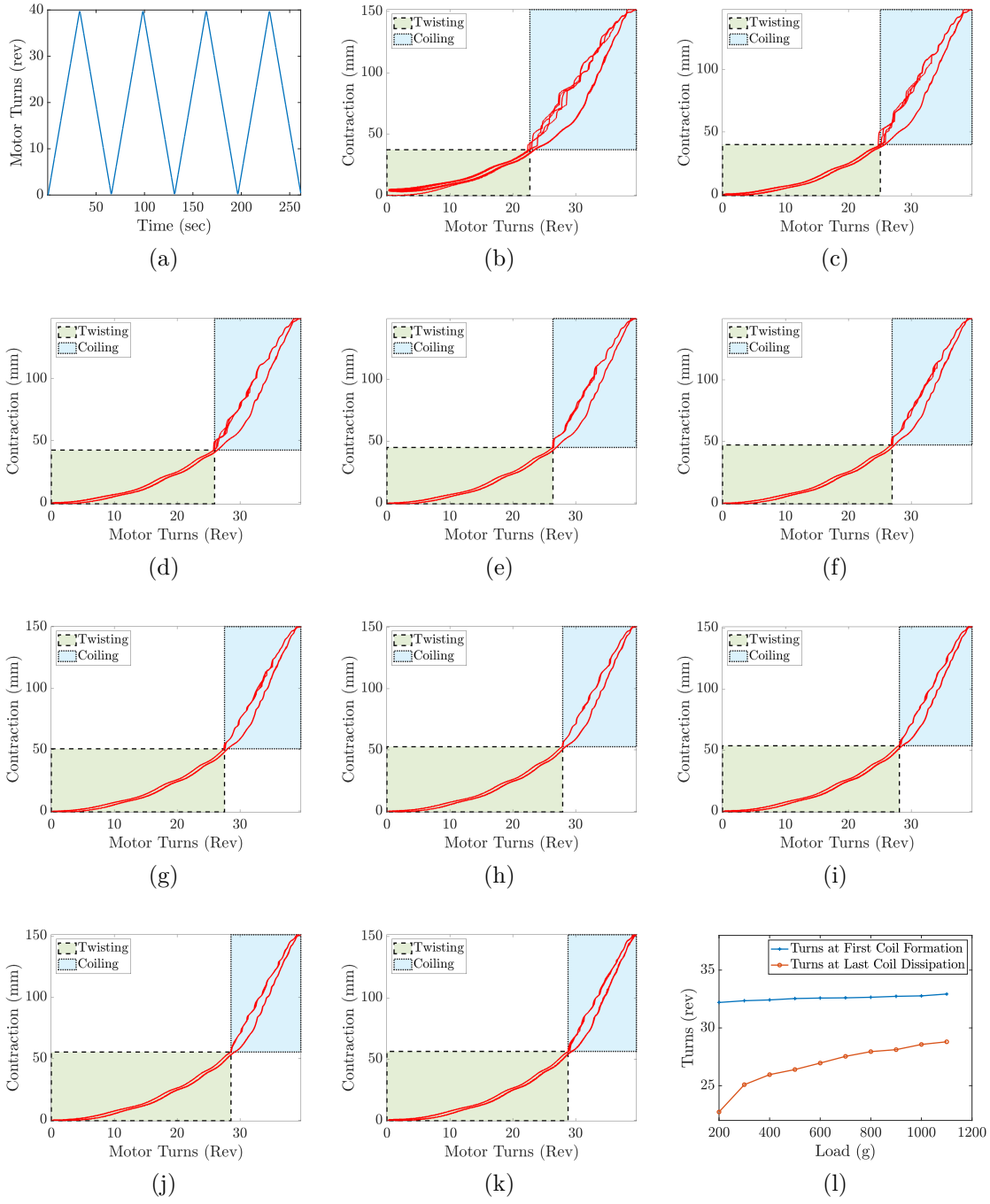

Figure 6.3: (a) Applied input sequence for the experiments to investigate the load dependence of the TCS actuators' behavior. Motor turns – contraction correlation of the TCS actuators for an applied payload of (b) 200 g, (c) 300 g, (d) 400 g, (e) 500 g, (f) 600 g, (g) 700 g, (h) 800 g, (i) 900 g, (j) 1000 g, and (k) 1100 g. (l) Variation of the motor turns at first coil formation and last coil dissipation with applied payload.

was labeled as the number of motor turns where the first coil forms. When the input rate is negative, the point where the top curve (contraction while untwisting) meet the bottom curve (contraction while twisting), was labeled as the number of motor turns where the last coil dissipates. As seen in Fig. 6.3(l), the number of turns where the first coil forms was fairly independent of the applied payload, whereas the number of motor turns where the last coil dissipates (point of transition) increased with the applied payload. This phenomenon results in the increased nonlinearity in the motor turns – contraction behavior of the TCS actuators at lower payloads.

6.3.2 Rate Dependence

The second set of experiments addressed the effect of input rate on the behavior of the TCS actuators. More specifically, the effect of the input rate on the non-smooth behavior of the TCS actuators will be investigated. It is noted that the behavior of the TCS actuators only in the coiling phase was considered. This was done because it is known that the behavior of the TCS actuators in the twisting phase, which is identical to the behavior of the TSAs, does not depend on the rate at which the input is being applied ([108]). To investigate the rate-dependence aspect of the TCS actuators, the following experiments were conducted. Without loss of generality, a payload of 800 g was attached to the TCS actuators. The input sequence applied to the actuators was restricted to range between 28 turns and 40 turns. The lower bound was selected based on the fact that the TCS actuators transitioned from coiling to twisting phase at 28 turns for a payload of 800 g (Fig. 6.3(h)). Ten sets of experiments were conducted. For each set, an input sequence consisting of four triangular waves was applied to the actuators. The speed at which the motor rotated was varied between 0.04 rev/sec to 0.13 rev/sec with an increment of 0.01 rev/sec for each set.

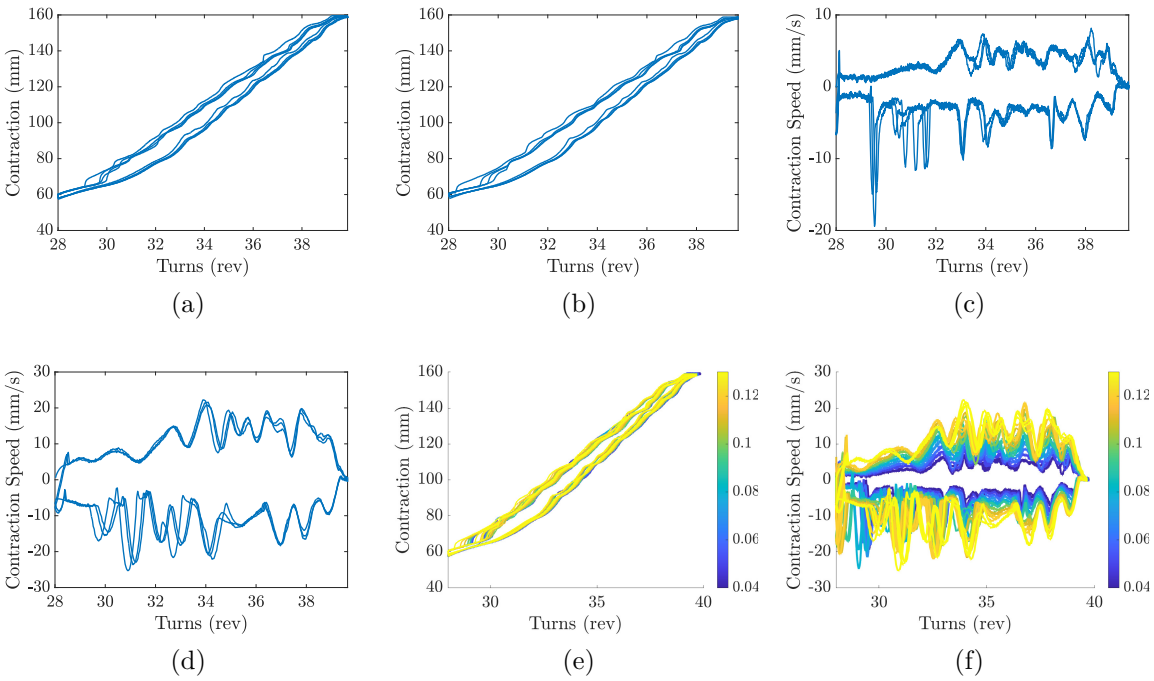

Figure 6.4: Motor turns – contraction correlation of the TCS actuators for a motor speed of (a) 0.04 rev/sec and (b) 0.13 rev/sec. Motor turns – contraction speed correlation of the TCS actuators for a motor speed of (c) 0.04 rev/sec and (d) 0.13 rev/sec. (e) Motor turns – contraction and (f) motor turns – contraction speed correlations for different motor speeds.

The experimental results are presented in Fig. 6.4. As an example, the motor turns – contraction correlation and the motor turns – contraction speed of the TCS actuators at 0.04 rev/sec, and 0.13 rev/sec are presented in Fig. 6.4(a)–(d). As it can be inferred from Fig. 6.4(a)–(b), the motor turns – contraction correlation of the TCS actuators is independent of the rate at which the motor turns were applied within the tested input range. This indicates that the non-smooth behavior which appears in the motor turns – contraction correlation cannot be pacified by varying the input rate and is an inherent property of the TCS actuators' behavior in the coiling phase. The motor turns – contraction speed correlations (Fig. 6.4(c)–(d)) show the effect of the coil formation phenomenon on the TCS actuators' contraction speed. The peaks in the correlation appear at the instances of coil formation and dissipation.

The magnitude of these peaks increased with the motor speed, which is an expected outcome. The full results of these experiments are presented in Fig. 6.4(e)–(f), which shows how the magnitude of the contraction speed increases with the motor speed, while the motor turns – contraction correlation remains mostly invariable with respect to the motor speed.

6.3.3 History Dependence

The last set of experiments addressed the effect of input history on the behavior of the TCS actuators. It is noted that only the behavior of the TCS actuators in the coiling phase was considered. This was done because of the fact that the behavior of the TCS actuators in the twisting phase which is identical to the behavior of the TSAs is not history-dependent. To investigate the history-dependence aspect of the TCS actuators, the following experiments were conducted.

Without loss of generality, a payload of 800 g was attached to the TCS actuators. The speed at which the motor rotated was selected to be 0.12 rev/sec. The input sequence applied to the actuators was restricted to range between 28 turns and 40 turns. Three experiments were conducted. The applied input sequences applied are presented in Fig. 6.5(a)–(c). For the remainder of the paper, the sequences presented in Fig. 6.5(a), (b), and (c) will be addressed as input sequence 1, input sequence 2, and input sequence 3, respectively.

The motor turns – contraction correlations for input sequence 1, input sequence 2, and input sequence 3, are presented in Fig. 6.5(d), (e), and (f), respectively. From these results, two unique phenomena can be observed: Firstly, the repeatabilty of the contraction profiles when the input rate is negative (untwisting of the strings)

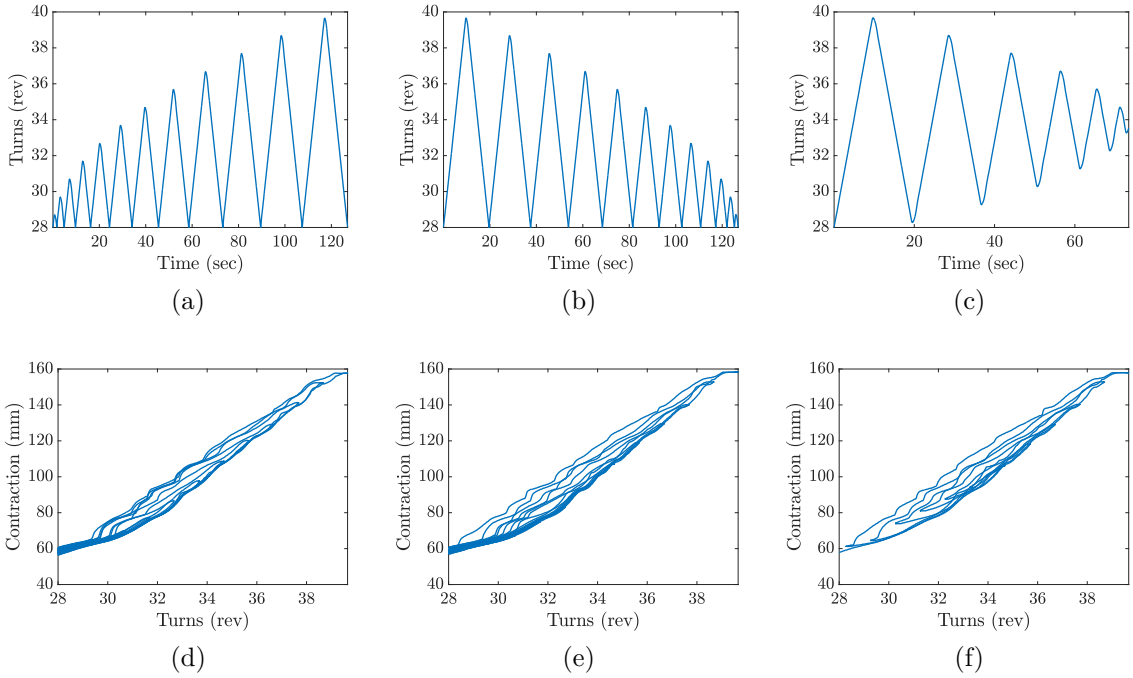

Figure 6.5: (a) Input sequence 1. (b) Input sequence 2. (c) Input sequence 3. Motor turns – contraction correlation of the TCS actuators when (d) input sequence 1, (e) input sequence 2, and (f) input sequence 3 are applied.

is relatively lower in comparison to the repeatabilty of the contraction profiles when the input rate is positive (twisting of the strings). More specifically, the non-smooth behavior while untwisting, which relates to the coil dissipation seems to be dependent on the input history and not just the current input which is applied to the TCS actuators. In contrast, the contraction profiles, including the non-smooth behavior are relatively more consistent and less dependent on the input history when the strings are being twisted.

Secondly, the point of transition, where the last coil dissipates, is not only load-dependent, but also history-dependent. This can be inferred from the correlations presented in Fig. 6.5(d)–(e), which were obtained by applying input sequence 1 and input sequence 2, which consisted of triangle waves of varying peak values. As the peak value for an input cycle increased, the point of transition which is the number of

turns where the last coil dissipates decreased. A potential reason for the appearance of this phenomenon could be the dry friction between the coiled strings, which increases with the number of coils formed in the TCS actuators' structure. The number of coils increased with the peak value of an input cycle, thereby increasing the overall dry friction in the structure. To overcome this increased dry friction, more number of untwists will be required which corresponds to low number of motor turns while untwisting.

6.4 Discussions

The experimental results indicated that the motor turns – contraction correlations of the TCS actuators are load and input history dependent but not rate dependent. The increase in the magnitudes of the peaks in the motor turns – contraction speed correlations with increasing motor speed indicated a positive correlation between the motor speed and the contraction speed. However, this phenomenon does not suggest rate dependent behavior as the motor turns – contraction correlations are fairly consistent at different motor speeds. This reduces the complexity of modeling this behavior because the models do not need to capture any rate dependence.

The motor turns – contraction correlations were dependent on the applied payload and input history. The results indicated that the contraction profiles while twisting were significantly less dependent on the load and the input history. However, the contraction profiles while untwisting largely varied based on the applied payload and the input history. Firstly, the applied payload dictated the point of transition of the TCS actuator, with the point of transition increasing with increasing payloads. This resulted in higher hysteresis and nonlinear behavior at lower loads. The results also

indicated that the point of transition became relatively more consistent for higher payloads, suggesting that TCS actuators could be more suitable for applications involving high force outputs.

Lastly, for a fixed payload, the motor turns – contraction correlations were history dependent with the history dependence mainly affecting the contraction profiles while the strings were being untwisted. During untwisting, not only the point of transition varied with the input history, but also the non-smooth behavior varied based on the input history. More specifically, the number of motor turns where coils dissipated varied based on the input history which affected the overall contraction profile. This would make the modeling and control of this behavior highly complicated. However, relatively simpler models and control strategies can be developed by sacrificing some amount of accuracy for lower complexity. By assuming zero history and load dependence, the geometry of the coiled structure could be leveraged to model the correlation between motor turns and contraction. Such models would accurately capture the TCS actuators' behavior during twisting, which is relatively more consistent and independent of applied payload and input history.

CHAPTER 7

MODELING AND INVERSE COMPENSATION OF THE NON-SMOOTH COILING-INDUCED ACTUATION IN TWISTED AND COILED STRING ACTUATORS

In this chapter the modeling and inverse compensation of the non-smooth coiling-induced actuation of the TCS actuators is addressed. TCS actuators' coiling-induced actuation is under-explored and exhibits unique characteristics: At a constant motor speed, twisting of strings generates contraction at increasing rate as the coil evolves from the coil initiation stage to the coil formation stage. As the coiling process is discrete with individual coils forming sequentially, the aforementioned behavior generates non-smooth input-output correlation. To facilitate the application of TCS actuators in robotic and mechatronic devices, modeling and control of their behavior needs to be established. As a first step towards this objective, modeling and compensation for the unique non-smooth behavior of the TCS actuators in the coiling phase is presented. The proposed strategies leverage the geometric configuration of the coils. The model is formulated by relating the bias angle of each coil to the corresponding motor twist inputs. The proposed strategies were experimentally validated to perform satisfactorily.

7.1 Motivation

Actuation in the coiling phase is generated by overtwisting the strings which results in the formation of coils along the length of the strings. While the coiling mechanism has been employed to fabricate soft actuators such as supercoiled polymer actuators ([129; 18]), its usage to generate actuation has been limited. The under-explored coiling phase of the TCS actuators exhibits unique properties: At a constant motor speed,

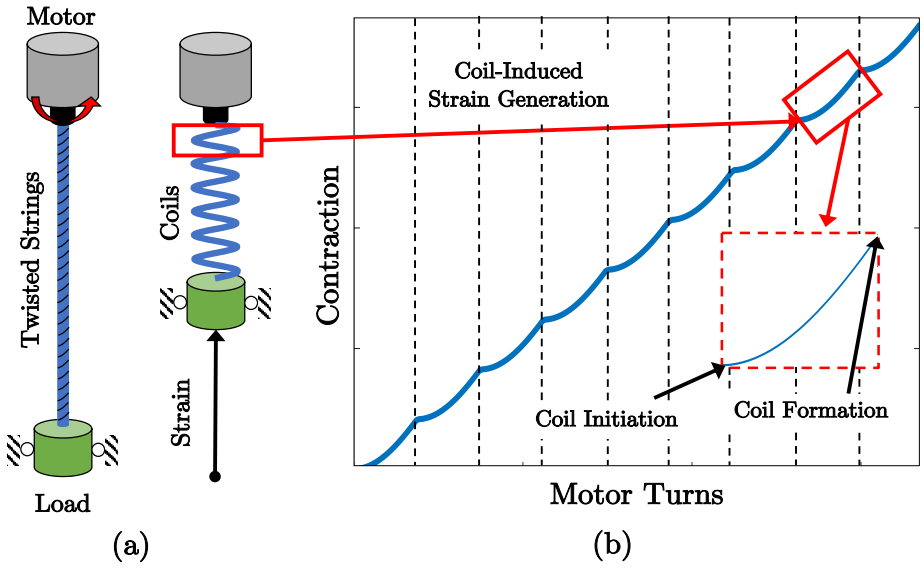

Figure 7.1: (a) Twisted and coiled string (TCS) actuators in their fully twisted (left) and fully coiled (right) states. (b) The coiling-induced actuation of TCS actuators comprising of the non-smooth behavior. The non-smooth contraction is highlighted with the coil initiation and formation instances labeled. The vertical lines in the plot divide the actuation range into different segments with each segment presenting the contraction due to a single coil.

twisting of strings generates contraction at increasing rate as the coil evolves from the coil initiation stage to the coil formation stage (Fig. 7.1(b)). We found that the coiling process is largely discrete with individual coils forming sequentially and not simultaneously (111). Due to this, the coiling-induced actuation generates non-smooth input-output correlation. The non-smooth relationship between the contraction of the TCS actuators and the input motor turns may cause oscillations and even vibrations in their output motion which is not desirable in applications where smooth motion is important, such as exoskeletal technology (130; 124), robotic grippers (131; 132), and soft robots (46; 43).

In order to facilitate the employment of TCS actuators in real-world applications, modeling and control of their behavior needs to be achieved. The modeling and control of the TCS actuators' behavior in the coiling phase has not been sufficiently

studied. Existing literature suggests two approaches to analyze the coiling process of overtwisted strings: 1) geometric models and 2) continuum mechanics models, but both present evident challenges.

Geometric models attempt to leverage the knowledge of the string configuration to study the behavior of coiled strings. A study exploring overtwisting of strings to generate higher strain generation was presented in (107). However, the presented geometric model had the following limitations: Firstly, the presented model does not consider the coiling process which results in the non-smooth behavior. While few coils are shown, the presented work in (107) does not fully consider the systematic coiling of the strings. Secondly, it is assumed that the mode of actuation remains same between regular twisting and overtwisting. Consequently, the equation describing the motion of the actuator in the regular twisting phase is directly used to capture the behavior in the overtwisting phase. The non-smooth coiling-induced actuation was not considered. Another study on the coiling mechanism presents geometric model which captures the relation between different coil parameters and the resultant contraction (133). However, the evolution of the coil from the coil initiation stage to the coil formation stage is not considered and only the configuration of the coil after it is fully formed is studied. Furthermore, both studies do not consider the control of the presented actuators.

Strategies based on continuum mechanics aim to capture the overall configuration of the coiled strings under different operating conditions (134; 135). For example, (136) presents models using Cosserat rod theory which correlate the contraction of the soft actuator to its input. However, the presented models rely on numerically realized continuum mechanics models, thereby making them not suitable for analysis from controls perspective. Furthermore, the actuator considered in (136) is already

in a coiled configuration and generates actuation through heating, which has been studied in existing literature using other modeling methods (18). Modeling strategies based on solid mechanics mainly focus on the conditions under which the coiling process commences. For example, the studies presented in (137; 138; 139; 140) focus on deriving and verifying the value of the input torque inserted into the strings where coils start forming for a given applied payload. The studies do not consider the behavior of the strings after the coiling process commences. While the aforementioned modeling strategies provide critical insights about the coiling process, they do not result in closed-form control-affine models. As a result, these existing models could not be conveniently used to control the behavior of the coiled strings.

As a first step towards developing control-affine models to model and control TCS actuators, in this study, the non-smooth coiling-induced actuation of TCS actuators is studied. The proposed modeling strategy leverages the knowledge about the geometry of the coils and generates a physics-based data-driven model. Furthermore, the model is inverted to realize inverse compensation. The proposed modeling and inverse compensation strategies were experimentally verified to be efficient. This is the *first* systematic study on the modeling and inverse compensation of the non-smooth coiling-induced actuation of TCS actuators.

7.2 Modeling and Control

In this section, the kinematic model which relates the motor turns to the TCS actuators' contraction, and the inverse model which relates the desired contraction with the required motor turns for inverse compensation, are presented.

7.2.1 Kinematic Model

The geometry of a segment of the string which evolves into a coil upon insertion of twists in different stages is shown in Fig. 7.2(a). Upon unwrapping the coiled segment, a right triangle can be constructed as shown in Fig. 7.2(b) ([133]). Here, l_i is the total length of the uncoiled string segment i under consideration, $l_{c,i}$ is the length of the coil i during the coil evolution, and α_i is the bias angle of coil i. The length of the coil $l_{c,i}$ can be related to l_i and α_i as follows:

$$l_{c,i} = l_i sin(\alpha_i). \tag{7.1}$$

By summing the lengths of different coils formed during the actuation process, the contraction of the TCS actuators can be obtained. In order to compute the contraction of the different coils, the lower and upper thresholds of motor turns where a particular coil is formed, and the relation between the motor turns θ and α_i for each coil are required.

Proposed Model

The proposed model is based on the following assumptions:

1. The formation of $(i+1)^{th}$ coil starts only after the formation of coil i is completed.
2. The coil bias angle α_i and the motor turns inserted into the string segment i can be approximately captured using a monotonically decreasing polynomial.

The first assumption is an acceptable approximation as experiments suggested that no two coils begin formation at the same instance and multiple coils form sequentially.

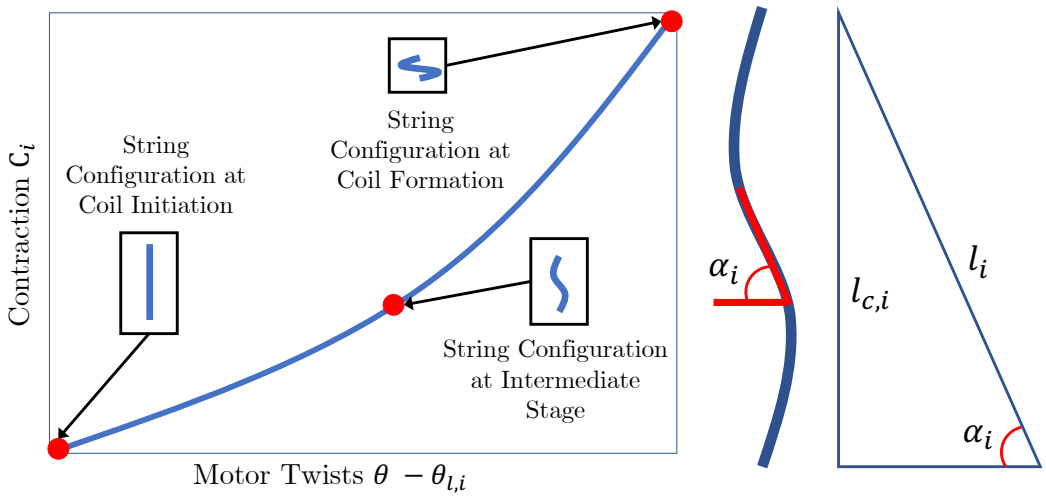

(a) (b)

Figure 7.2: (a) The contraction of the TCS actuator as a result of i^{th} coil evolution from the point of coil initiation to the point of coil formation. The coil configuration at different stages are highlighted in the plot. (b) Unwrapping the final coil configuration to construct a right triangle with different parameters labelled.

This can be further confirmed by the supplementary videos of our recent work on TCS actuators (111). The second assumption implies a monotonically decreasing relationship between α_{i} and the number of motor turns inserted in string segment i. The relationship is monotonically decreasing due to the description of α_{i} in Fig. 7.2: before coil initiation, the string is just in a straight configuration with $\alpha_{\mathrm{i}} = 90°$. As the coil evolves and progresses towards coil formation, α_{i} keeps decreasing. It is noted that when a coil is fully formed, $\alpha_i > 0°$.

For a string segment i, the lower and upper thresholds of motor turns between which the coil evolution takes place are defined as $\theta_{\mathrm{l,i}}$ and $\theta_{\mathrm{u,i}}$, respectively. The geometry of the coils and the range of motor turns for each coil, within which a coil evolves during motor twisting range $[\theta_{\mathrm{l,i}}, \theta_{\mathrm{u,i}}]$ could be different. The contraction C_i

of the string segment i can be defined as

$$C_{\mathrm{i}} = \begin{cases} 0 & \text{if} \quad \theta < \theta_{\mathrm{l,i}} \\ l_i(1 - sin(\alpha_i)), & \text{if} \quad \theta \geq \theta_{\mathrm{l,i}}, \end{cases} \tag{7.2}$$

where,

$$\alpha_{\mathrm{i}} = \begin{cases} G_i(\theta - \theta_{\mathrm{l,i}}) + \frac{\pi}{2}, & \text{if} \quad \theta_{\mathrm{l,i}} \leq \theta \leq \theta_{\mathrm{u,i}} \\ G_i(\theta_{\mathrm{u,i}} - \theta_{\mathrm{l,i}}) + \frac{\pi}{2}, & \text{if} \quad \theta > \theta_{\mathrm{u,i}}, \end{cases} \tag{7.3}$$

where

$$G_i(x) = a_{0,i} + a_{1,i}x + a_{2,i}x^2 + ... + a_{m,i}x^m. \tag{7.4}$$

G_i is an m^{th} order polynomial which describes the relation between α_{i} and the motor turns $(\theta - \theta_{\mathrm{l,i}})$ inserted in the i^{th} string segment. To maintain simplicity, the proposed model is formulated such that the order of G_i for all i will be the same. In Eq. (7.4), $a_{k,i}$ with $k = 0, 1, 2, ..., m$, are constant coefficients.

$\theta_{\mathrm{l,i}}$ and $\theta_{\mathrm{u,i}}$ of each coil can be obtained based on the velocity profile of the TCS actuators in the coiling phase: The peaks in the velocity profile denote the instances where a coil is fully formed. The number of turns where a particular peak reaches it maximum value will be defined as the upper threshold for the corresponding coil. Since it is assumed that the formation of $(i+1)^{th}$ coil starts only after the formation of coil i is completed, the lower threshold $\theta_{\mathrm{l,i}}$ for different coils can be defined as follows:

$$\begin{aligned} \theta_{\mathrm{l,1}} &= \min(\theta), \\ \theta_{\mathrm{l,i}} &= \theta_{\mathrm{u,i-1}}, \text{ for } i = 2, 3, ..., n, \end{aligned} \tag{7.5}$$

where n is the total number of coils. The upper threshold of the final coil (n^{th} coil) is defined as $\theta_{\mathrm{u,n}} = \max(\theta)$. Due to this description of $\theta_{\mathrm{l,i}}$ and $\theta_{\mathrm{u,i}}$, the proposed model will be continuous and differentiable in the range [min(θ), max(θ)].

The parameters which will be identified based on experimental data include the string segments lengths l_i and the coefficients for each G_i. For example, the bias

angle at the coil initiation stage ($\alpha_{\mathrm{i,max}}$) and after a coil is fully formed ($\alpha_{\mathrm{i,min}}$) can be experimentally measured. Therefore, the constant coefficients of G_i in the proposed model will be identified based on data assuming a monotonically decreasing correlation between α_{i} and the motor turns inserted in the string segment i, with α_{i} decreasing from $\alpha_{\mathrm{i,max}}$ to $\alpha_{\mathrm{i,min}}$. Consequently, the total number of parameters which need to be identified based on data is $n \times (m+1)$, where, n is the number of coils and m is the order of G_i. It is assumed that $\alpha_{\mathrm{i,max}}$ and $\alpha_{\mathrm{i,min}}$ for all coils is the same (133) as the coil bias angles for all the coils were measured to be similar with negligible difference. While $\alpha_{\mathrm{i,max}}$ for each coil can be defined as 90°, $\alpha_{\mathrm{i,min}}$ can be measured experimentally.

The total contraction C_{total} of the TCS actuators will be

$$C_{\mathrm{total}} = F(\theta) = \sum_{i=1}^{n} C_{\mathrm{i}}. \tag{7.6}$$

The proposed model will be addressed as Model #1 for the remainder of the paper.

Simplified Model with First-Order G_i

A simplified version of Model #1 can be obtained by assuming that G_i defined in Eq. (7.3) is a first-order polynomial. This simplified version of Model #1 results in Model #2. Assuming a linear correlation for G_i simplifies the analysis in two ways: Firstly, the coefficients of the linear correlation can be predefined as $\alpha_{\mathrm{i,max}}$ and $\alpha_{\mathrm{i,min}}$, and their corresponding motor turns, $\theta_{\mathrm{l,i}}$ and $\theta_{\mathrm{u,i}}$, are known. Secondly, a linear model makes the model inversion for inverse compensation relatively simpler since parameter identification is greatly simplified.

For Model #2, α_{i} is defined as follows:

$$\alpha_{\mathrm{i}} = \begin{cases} K_i(\theta - \theta_{\mathrm{l,i}}) + \frac{\pi}{2}, & \text{if} \quad \theta_{\mathrm{l,i}} \leq \theta \leq \theta_{\mathrm{u,i}} \\ K_i(\theta_{\mathrm{u,i}} - \theta_{\mathrm{l,i}}) + \frac{\pi}{2}, & \text{if} \quad \theta > \theta_{\mathrm{u,i}}, \end{cases} \tag{7.7}$$

where, K_i is the constant of proportionality for the i^{th} coil, which can be defined as

$$K_i = \frac{\alpha_{\mathrm{i,max}} - \alpha_{\mathrm{i,min}}}{\theta_{\mathrm{l,i}} - \theta_{\mathrm{u,i}}}. \tag{7.8}$$

The thresholds of each coil $\theta_{\mathrm{l,i}}$ and $\theta_{\mathrm{u,i}}$ are defined in the same manner as Model #1. The output of Model #2 can be computed using Eqs. (7.2), (7.6), and (7.7). Unlike Model #1, for Model #2, only the string segments' lengths l_i will be identified based on data.

Simplified Model with Same Coil Geometry

Model #2 can be further simplified to generate Model #3 by considering the following additional assumptions:

1. The coil geometry is same for the all the coils.
2. The number of turns required for a coil to form is the same for all the coils.

The additional assumptions imply that the geometry of the coils and the number of turns required for formation of each coil $\theta_{\mathrm{u,i}} - \theta_{\mathrm{l,i}}$ will be the same and will be equal to $(\max(\theta) - \min(\theta))/n$, n being the number of coils. Using this number, the range of motor turns for each coil can be defined.

The contraction of the TCS actuators will still be defined by Eqs. (7.2), (7.6), (7.7) and (7.8). Due to the assumptions for Model #3, variables such as K_i and l_i will

be the same for all the coils. Since Model #3 assumes that the geometry of all the coils will be the same, only one variable l_i will be identified based on the experimental data.

7.2.2 Inverse Compensation

To achieve control of TCS actuators, inverse compensation was chosen due to its demonstrated effectiveness in existing literature ([72; 141]). Control through inverse compensation requires inverting the forward model which relates the system input to the system output such that given a desired output, the inverse model computes the required input to apply to the system. The model presented in this section is an inversion of Model #2, due to its relatively simple structure which allows for model inversion without demanding any further parameter identification. The required number of turns θ_{r} is defined as

$$\theta_{\mathrm{r}} = F^{-1}(C_{\mathrm{d}}) = \sum_{i=1}^{n} \theta_{\mathrm{i}}, \tag{7.9}$$

where θ_{i} is the required number of turns to extract contraction from the i^{th} coil and C_{d} is the desired contraction. θ_{i} is a function of C_{d} and is defined as follows:

$$\theta_{\mathrm{i}} = \begin{cases} 0 & \text{if} \quad C_{\mathrm{d}} < C_{\mathrm{l,i}} \\ \dfrac{sin^{-1}(1-\frac{C_{\mathrm{d}}-C_{\mathrm{l,i}}}{l_i})-\frac{\pi}{2}}{K_i}, & \text{if} \quad C_{\mathrm{l,i}} \leq C_{\mathrm{d}} \leq C_{\mathrm{u,i}} \\ \dfrac{sin^{-1}(1-\frac{C_{\mathrm{u,i}}-C_{\mathrm{l,i}}}{l_i})-\frac{\pi}{2}}{K_i}, & \text{if} \quad C_{\mathrm{d}} > C_{\mathrm{u,i}}, \end{cases} \tag{7.10}$$

where $C_{\mathrm{l,i}}$ and $C_{\mathrm{u,i}}$ are the contraction thresholds of the i^{th} coil and are analogous to $\theta_{\mathrm{l,i}}$ and $\theta_{\mathrm{u,i}}$ in the kinematic model. For each coil, $C_{\mathrm{l,i}}$ and $C_{\mathrm{u,i}}$ are computed using

$\theta_{\mathrm{l,i}}$ and $\theta_{\mathrm{u,i}}$, and the kinematic model as:

$$\begin{aligned} C_{\mathrm{l,i}} &= F(\theta_{\mathrm{l,i}}), \\ C_{\mathrm{u,i}} &= F(\theta_{\mathrm{u,i}}). \end{aligned} \tag{7.11}$$

F is constructed from Eq. (7.6) with a first order polynomial for G_i in Eq. (7.3). K_i is the constant of proportionality for the i^{th} coil and is defined from the forward kinematic model using Eq. (7.8).

7.3 Experimental Results

In this section, the proposed models and inverse compensation strategy are experimentally validated. The TCS actuators were fabricated using the procedures described in Section 6.2. The experimental setup used to collect data for analysis was the same as the one described in Section 5.3.1.

7.3.1 Model Identification

Since the main focus of this study is the analysis of the TCS actuators' coiling phase, all the input sequences used in this study for model identification and validation will have a minimum value of 32 turns during which the strings are fully twisted. Furthermore, the input twists never exceeded 38.7 turns during which the TCS muscle was close to be fully coiled. This is to avoid damage to the experimental setup. To collect the data used to identify the models, without loss of generality, the motor was run at 1.2 rev/sec speed and a payload of 800 g was attached to the TCS actuators. The input sequence used to collect data for model identification and the resultant motor turns contraction correlation is presented in Fig. 7.3(a)–(b). For the TCS

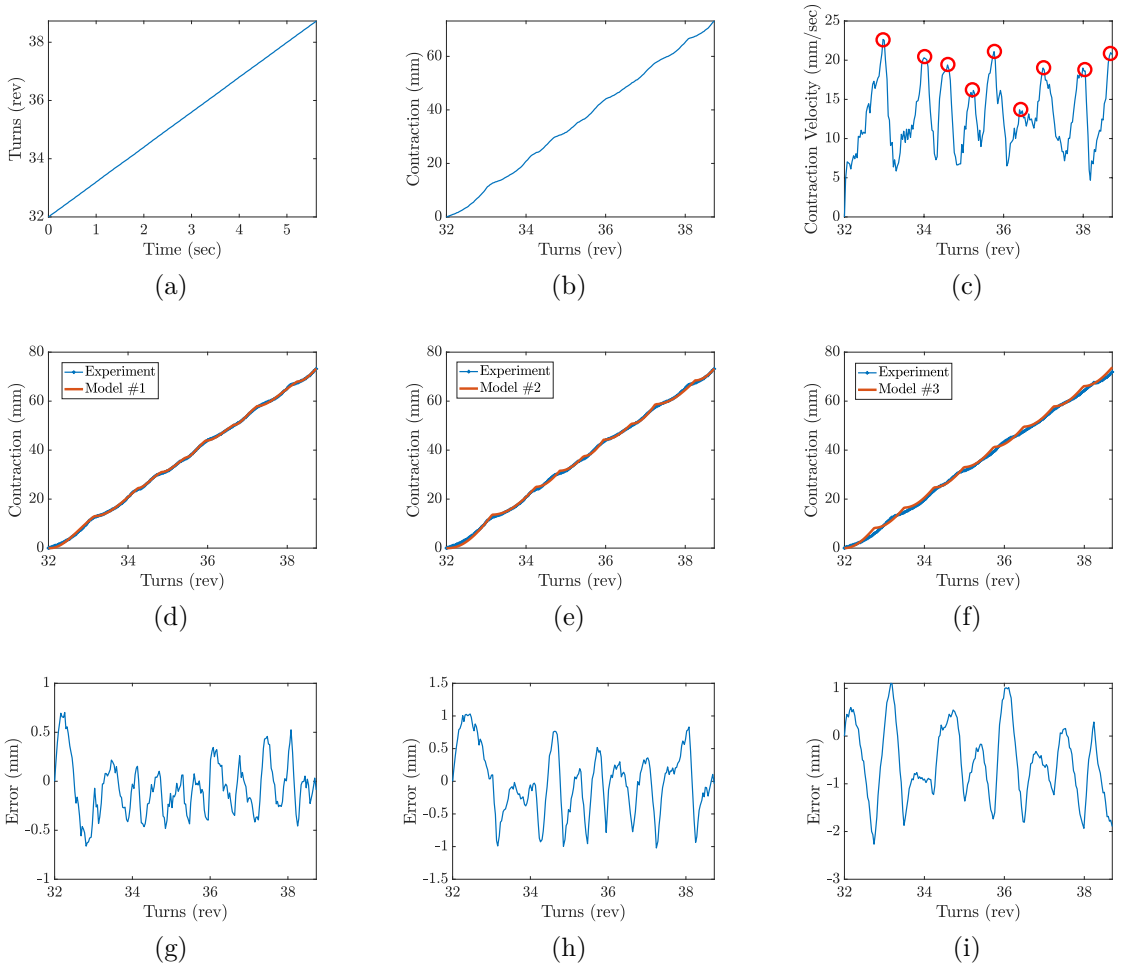

Figure 7.3: (a) Input motor turns applied to the TCS actuator for data collection used for model identification. (b) Motor turns – contraction correlation. (c) Motor turns – contraction velocity correlation used to define the range of motor turns of each coil. The maximum values for each peak used to determine $\theta_{u,i}$ for each coil are highlighted. Model identification results for (d) Model #1, (e) Model #2, and (f) Model #3. Model identification error for (g) Model #1, (h) Model #2, and (i) Model #3.

actuators used in this study $\alpha_{i,min}$ was measured to be 13.5°. It is noted that for a TCS actuator constructed using a different string material, the value of $\alpha_{i,min}$ may change. The maximum contraction achieved during the coiling phase was 73.48 mm. It is noted that the TCS actuators produce more than 70% contraction when the twisting phase is also considered.

For Model #1 and Model #2, the range of motor turns for each coil have to be identified and predefined. This was done by examining the contraction velocity profile with respect to the motor turns. The experiments indicated that a total of nine coils were formed at 38.7 turns. For each coil, the number of turns where the peak reaches its maximum value was defined as $\theta_{\mathrm{u,i}}$. $\theta_{\mathrm{l,i}}$ for each coil was defined according to Eq. (7.5). The $\theta_{\mathrm{u,i}}$ for each coil is highlighted in the motor turns – contraction velocity correlation presented in Fig. 7.3(c). For Model #3, considering the coiling phase started at 32 turns, the number of turns required for formation each coil was predefined to be 0.75 turns. Using this number the range of motor turns for each coil were obtained.

Model #1 was constructed assuming a second order correlation for G_i in Eq. (7.3). The parameters for all the proposed models were identified using the *fmincon* function on MATLAB$^{\mathrm{TM}}$. The model identification results for Model #1, Model #2, and Model #3 are presented in Fig. 7.3(d)–(i). The error plots in Fig. 7.3(g)–(i) were generated by taking the difference between the estimated and the actual values. The modeling errors were computed using the following equation:

$$error = \sqrt{\frac{\sum_{k=1}^{w}(y_{estimated,k} - y_{actual,k})^2}{w}}, \tag{7.12}$$

where y_{actual} is the vector of experimental data, $y_{estimated}$ is the vector of data estimated by the model, k is the index of the data point in the corresponding vectors, and w is the length of the aforementioned vectors. The model identification errors for Model #1, Model #2, and Model #3 were 0.29 mm, 0.49 mm, and 0.95 mm, respectively. These numbers translated to 0.4%, 0.66%, and 1.3% errors with respect to the overall actuation range.

As indicated by the results, all the three proposed models performed satisfactorily, with Model #1 outperforming Model #2 and Model #3. The usage of less

assumptions could be a reason for the better performance of Model #1. However, considering its superior performance and simplicity in formulation, Model #2 could be a more desirable modeling strategy. A potential source of error for the proposed models could be the assumption that the $(i+1)^{th}$ coil forms only after the formation of i^{th} coil. There could have been an overlap between the motor turns ranges of two coils with $(i+1)^{th}$ coil forming before the completion of the i^{th} coil formation. However, this assumption on sequential coil formation greatly simplified the inversion of the kinematic model used for inverse compensation of the TCS actuators.

7.3.2 Model Validation

To validate the proposed models, data was collected by applying four cycles of triangle waves whose amplitude decreased as the number of cycles increased. From the obtained contraction data, the data corresponding to the forward stroke of the TCS actuator was selected. The reason for this is discussed in Section 6.4. The model validation results for Model #1, Model #2, and Model #3 are presented on Fig. 7.4. The error plots in Fig. 7.4(d)–(f) were generated by taking the difference between the estimated and the actual values. The model validation error was computed using Eq. (7.12).

The model validation errors for Model #1, Model #2, and Model #3 were 0.93 mm, 0.94 mm, and 1.27 mm, respectively. These numbers translated to 1.26%, 1.27%, and 1.76% errors with respect to the overall actuation range. Similar to the model identification results, the model validation results indicated that all the three models performed satisfactorily with Model #1 outperforming Model #2 and Model #3. It is noted that the obtained errors are larger than those in model identification in Section

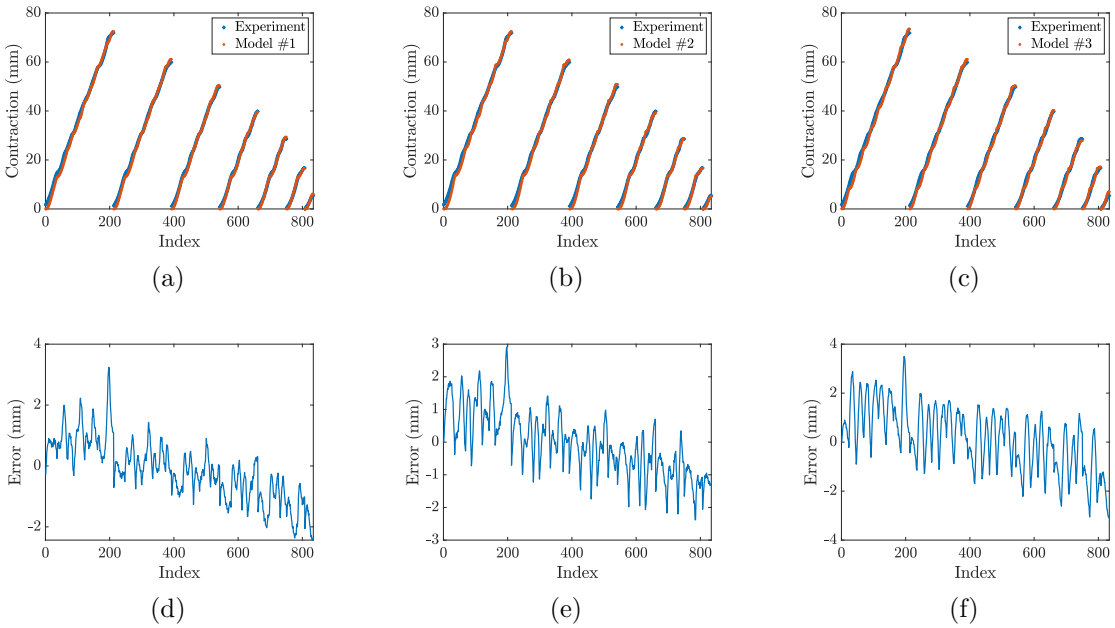

Figure 7.4: Model validation results for (a) Model #1, (b) Model #2, and (c) Model #3. Model validation error for (d) Model #1, (e) Model #2, and (f) Model #3.

6.3.1. This larger error could be caused due to TCS actuator's complex nonlinearities ([128]).

7.3.3 Inverse Compensation

For inverse compensation, the desired trajectory was four cycles of triangle waves whose amplitude increased as the number of cycles increased. From the obtained contraction data, the data corresponding to the forward stroke of the TCS actuator was selected. Similarly, the reason for this is discussed in Section 6.4. The results of the inverse compensation using the proposed inverse model are presented in Fig. 7.5. The error plots in Fig. 7.5(b) were generated by taking the difference between the desired and the actual values. The control error, which was computed using Eq. (7.12), for the proposed strategy was 0.83 mm. This translated to 1.11% error with

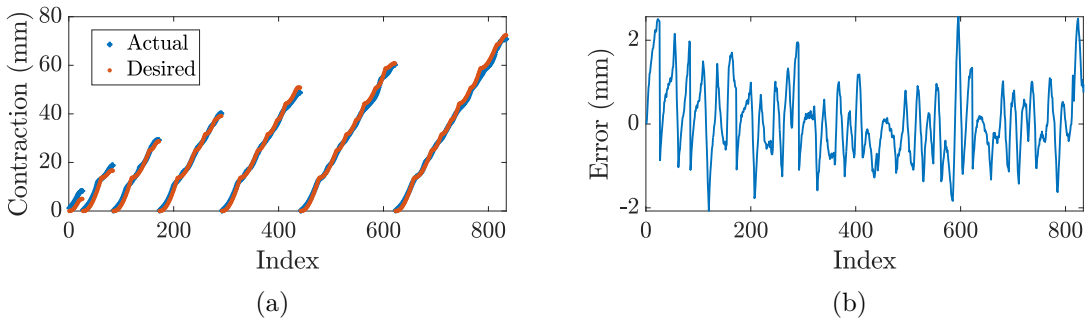

Figure 7.5: (a) Trajectory tracking and (b) control error using the proposed inverse model.

respect to the overall actuation range. This was deemed to be acceptable as it is similar to the modeling error of Model #2 based off of which the inverse model was developed.

7.4 Discussions

In this work, the unique non-smooth coiling-induced actuation of TCS actuators was modeled and compensated for. The proposed modeling strategy leveraged the knowledge about the coil geometry and related the motor twists with the output contraction in a novel way. Three modeling strategies were presented and one of them was used to derive an inverse model for inverse compensation. The proposed modeling and inverse compensation strategies were experimentally validated to be efficient. Further improvements to the proposed modeling and control strategies could be considered for future work. Firstly, the velocity kinematics of the TCS actuators can be derived and analyzed. Secondly, the motor dynamics in the coiling phase, which mainly depend on the applied payload to the TCS actuators, could be modeled.

CHAPTER 8
CONCLUSION AND FUTURE WORK

8.1 Conclusions

In this dissertation, the modeling and control for TSA-driven soft robotic manipulator was studied. The kinematic relationships between the TSA actuation and the manipulator's bending angle were modeled and experimentally verified. Open-loop control was realized by applying the inverse kinematic model. The experimental results confirmed the effectiveness of the proposed strategies. The drawbacks which appear in the soft robotic manipulator as a result of the inherent limitations of the TSAs were discussed and addressed.

Firstly, the hysteresis with lonely stroke behavior exhibited by multiple popular artificial muscles and soft robots was experimentally characterized, modeled, and compensated. A detailed analysis of the proposed modeling approach was presented where the effects of discretization levels and expanded columns on the modeling performance and computational cost were examined. The effectiveness of the proposed algorithm was verified through a statistical analysis. The proposed approach was applied to capture the quasi-static hysteresis with lonely stroke property of SCP actuator. The approach was further validated by applying it to model the hysteresis with lonely stroke properties of pneumatic actuators, SMA actuators, and SMP actuators. An inverse compensation algorithm was presented and its control performance was evaluated in experiment.

Secondly, estimation and adaptive control algorithms for TSAs were formulated, and their effectiveness was verified through simulation. The simulations results

showed satisfactory performance. Overall, the adaptive estimation and control techniques enable many unknown parameters of the TSA to be estimated, while achieving accurate tracking control.

Thirdly, stiff and compliant TCS actuators were fabricated and their behavior was experimentally characterized. In both cases, large strains of more than twice the strains achieved by regular twisting were obtained. The findings were further supported by the actuation speed, force generation and required torque of the TCS actuators. The consistent electrical resistance measurements indicated that the compliant SCP-based TCS actuators have strong potential to be utilized for strain self-sensing. The behavior of the TCS actuators was further experimentally characterized: The dependence of the TCS actuators' behavior on the applied payload, input rate, and input history were experimentally investigated. The results indicated that while the behavior did not exhibit dependence on the input rate, the behavior was dependent on the applied payload and the input history. More specifically, the contraction profiles of the TCS actuators when the strings were being untwisting varied based on the applied payload and the input history. The effects of these conclusions on the modeling and applications of TCS actuators were discussed.

Lastly, the unique non-smooth coiling-induced actuation of TCS actuators was modeled and compensated for. The proposed modeling strategy leveraged the knowledge about the coil geometry and related the motor twists with the output contraction in a novel way. Three modeling strategies were presented and one of them was used to derive an inverse model for inverse compensation. The proposed modeling and inverse compensation strategies were experimentally validated to be efficient.

8.2 Future Work

Further improvements can be made in the future. For the modeling and control of the soft robotic manipulator, firstly, the dynamic modeling of the TSA-driven soft robots can be derived by utilizing dynamic model of the TSA and continuum mechanics based strategies such as the Cosserat rod theory (55). Secondly, closed-loop control can be developed to accurately control the state of the TSA-driven soft robot. Thirdly, by replacing the traditional strings with compliant and conductive supercoiled polymer (SCP) strings, self-sensing TSAs can be obtained (40), where self-sensing based control can be explored. Lastly, the design of the manipulator can be modified to include TCS actuators as the driving mechanism.

Future improvements for the modeling and inverse compensation of hysteresis with lonely stroke behavior include the following considerations: Firstly, the analysis can be expanded to cover other commonly used hysteresis models such as the Prandtl-Ishlinskii (PI) model. Unlike Preisach operator, the inverse of a PI model is also a PI model. Hence accounting for the lonely stroke behavior in the inverse compensation of the PI model could possibly be less computationally expensive. Secondly, including the system dynamics into the proposed modeling and compensation schemes for lonely stroke behavior could be another area of potential future work. The system dynamics may result in rate-dependent hysteresis with lonely stroke behavior. Capturing this type of behavior would also enable real-time feedback control of artificial muscles exhibiting the hysteresis with lonely behavior. Sine and ramp signals are highly relevant in such studies and therefore will be used in future work. Finally, the behavior of several artificial muscles which exhibit three-dimensional hysteresis (70) could also incorporate the lonely stroke property. For example, both the quasi-static voltage-strain and load-strain relationships of SCP actuators exhibit hysteresis with lonely

stroke behavior. Hence, in theory, when the first loading cycle is applied to the SCP actuator with voltage cycles applied at each step, this could potentially result in a lonely stroke in three dimensional space. Furthermore, consider an SCP actuator-powered robotic bicep with two links similar to (70). The actuator contracts on the application of voltage, consequently lifting the lower link. During this movement, besides variation in the voltage, the actuator would also experience variation in the mechanical load due to the displacement of the lower link and gravitational effects. This could also potentially result in a three-dimensional lonely stroke. Experimental characterization, modeling and compensation of the three dimensional hysteresis with lonely stroke behavior would highly improve the control performance of artificial muscles and diverse intelligent systems.

Future improvements of the parameter estimation and adaptive control strategies for TSAs include the following considerations: Firstly, the proposed algorithms will be experimentally validated. Secondly, the estimation algorithm will be modified to consider the variable string radius. Lastly, the proposed estimation algorithm was not directly used in the control strategy presented in this paper. As a part of future work, other adaptive control strategies such as adaptive pole placement control (APPC), indirect MRAC, and robust MRAC will be explored and compared.

Future improvements for the modeling and inverse compensation of TCS actuators include the following considerations: Firstly, the velocity kinematics of the TCS actuators can be derived and analyzed. Secondly, the motor dynamics in the coiling phase, which mainly depend on the applied payload to the TCS actuators, could be modeled. In this study, only the TCS actuators' behavior during forward stroke was considered. This is because the TCS actuators' behavior during the forward stroke exhibited relatively higher consistency and lower dependence on the operating

conditions as opposed the backward stroke which was affected by hysteresis. Furthermore, the hysteretic behavior exhibited dependencies on applied payload to the TCS actuator and the type of input sequences applied to the TCS actuator (128). Purely data-driven mathematical models would be suitable to capture such hysteretic correlations. Hysteresis modeling will be considered as a part of future work.

BIBLIOGRAPHY

[1] S. I. Rich, R. J. Wood, and C. Majidi, "Untethered soft robotics," *Nature Electronics*, vol. 1, no. 2, p. 102, 2018.

[2] Y. Almubarak and Y. Tadesse, "Twisted and coiled polymer (TCP) muscles embedded in silicone elastomer for use in soft robot," *Int. J. Intell. Robot. Appl.*, 2017.

[3] S. Chen, Y. Cao, M. Sarparast, H. Yuan, L. Dong, X. Tan, and C. Cao, "Soft crawling robots: design, actuation, and locomotion," *Advanced Materials Technologies*, vol. 5, no. 2, p. 1900837, 2020.

[4] J. Sun, B. Tighe, Y. Liu, and J. Zhao, "Twisted-and-coiled actuators with free strokes enable soft robots with programmable motions," *Soft Robotics*, vol. 8, no. 2, pp. 213–225, 2021.

[5] D. S. Shah, J. P. Powers, L. G. Tilton, S. Kriegman, J. Bongard, and R. Kramer-Bottiglio, "A soft robot that adapts to environments through shape change," *Nature Machine Intelligence*, vol. 3, no. 1, pp. 51–59, 2021.

[6] R. F. Shepherd, F. Ilievski, W. Choi, S. A. Morin, A. A. Stokes, A. D. Mazzeo, X. Chen, M. Wang, and G. M. Whitesides, "Multigait soft robot," *Proceedings of the National Academy of Sciences*, vol. 108, no. 51, pp. 20 400–20 403, 2011.

[7] Y. Hao, S. Biswas, E. W. Hawkes, T. Wang, M. Zhu, L. Wen, and Y. Visell, "A multimodal, enveloping soft gripper: shape conformation, bioinspired adhesion, and expansion-driven suction," *IEEE Transactions on Robotics*, vol. 37, no. 2, pp. 350–362, 2020.

[8] Y. Cui, X.-J. Liu, X. Dong, J. Zhou, and H. Zhao, "Enhancing the universality of a pneumatic gripper via continuously adjustable initial grasp postures," *IEEE Transactions on Robotics*, pp. 1–15, 2021.

[9] J. Zhang, J. Sheng, C. O'Neill, C. J. Walsh, R. J. Wood, J. H. Ryu, J. P. Desai, and M. C. Yip, "Robotic artificial muscles: Current progress and future perspectives for biomimetic actuators," *IEEE Trans. Robot.*, vol. 35, no. 3, pp. 761–781, 2019.

[10] S. M. Mirvakili and I. W. Hunter, "Artificial muscles: Mechanisms, applications, and challenges," *Advanced Materials*, vol. 30, no. 6, p. 1704407, 2017.

[11] Z. Ye and Z. Chen, "Modeling and control of a 2-DOF dielectric elastomer diaphragm actuator," *IEEE/ASME Transactions on Mechatronics*, vol. 24, no. 1, pp. 218–227, 2019.

[12] M. A. Robertson, O. C. Kara, and J. Paik, "Soft pneumatic actuator-driven origami-inspired modular robotic 'pneumagami'," *The International Journal of Robotics Research*, vol. 40, no. 1, pp. 72–85, 2021.

[13] C. Laschi, B. Mazzolai, and M. Cianchetti, "Soft robotics: Technologies and systems pushing the boundaries of robot abilities," *Science Robotics*, vol. 1, no. 1, 2016.

[14] N. Kellaris, V. Gopaluni Venkata, G. M. Smith, S. K. Mitchell, and C. Keplinger, "Peano-HASEL actuators: Muscle-mimetic, electrohydraulic transducers that linearly contract on activation," *Science Robotics*, vol. 3, no. 14, 2018.

[15] P. Rothemund, N. Kellaris, S. K. Mitchell, E. Acome, and C. Keplinger,

"HASEL artificial muscles for a new generation of lifelike robots—recent progress and future opportunities," *Advanced Materials*, vol. 33, no. 19, 2021.

[16] Z. Ye, Z. Chen, R. Asmatulu, and H. Chan, "Robust control of dielectric elastomer diaphragm actuator for human pulse signal tracking," *Smart Materials and Structures*, vol. 26, no. 8, p. 085043, 2017.

[17] H. Rodrigue, W. Wang, M. W. Han, T. J. Y. Kim, and S. H. Ahn, "An overview of shape memory alloy-coupled actuators and robots," *Soft Robot.*, vol. 4, no. 1, pp. 3–15, 2017.

[18] M. C. Yip and G. Niemeyer, "On the control and properties of supercoiled polymer artificial muscles," *IEEE Transactions on Robotics*, vol. 33, no. 3, pp. 689–699, 2017.

[19] X. Tang, K. Li, Y. Liu, D. Zhou, and J. Zhao, "A general soft robot module driven by twisted and coiled actuators," *Smart Materials and Structures*, vol. 28, no. 3, p. 035019, 2019.

[20] W. S. Chu, K. T. Lee, S. H. Song, M. W. Han, J. Y. Lee, H. S. Kim, M. S. Kim, Y. J. Park, K. J. Cho, and S. H. Ahn, "Review of biomimetic underwater robots using smart actuators," *Int. J. Precis. Eng. Manuf.*, vol. 13, no. 7, pp. 1281–1292, 2012.

[21] J.-H. Koo, A. Dawson, and H.-J. Jung, "Characterization of actuation properties of magnetorheological elastomers with embedded hard magnetic particles," *Journal of Intelligent Material Systems and Structures*, vol. 23, no. 9, pp. 1049–1054, 2012.

[22] T. Kikuchi, K. Otsuki, J. Furusho, H. Abe, J. Noma, M. Naito, and N. Lauzier,

"Development of a compact magnetorheological fluid clutch for human-friendly actuator," *Adv. Robot.*, vol. 24, no. 10, pp. 1489–1502, 2010.

[23] B. Shih, D. Drotman, C. Christianson, Z. Huo, R. White, H. I. Christensen, and M. T. Tolley, "Custom soft robotic gripper sensor skins for haptic object visualization," in *2017 IEEE/RSJ International Conference on Intelligent Robots and Systems (IROS)*, 2017, pp. 494–501.

[24] Y. Tang, Y. Chi, J. Sun, T.-H. Huang, O. H. Maghsoudi, A. Spence, J. Zhao, H. Su, and J. Yin, "Leveraging elastic instabilities for amplified performance: Spine-inspired high-speed and high-force soft robots," *Science Advances*, vol. 6, no. 19, 2020.

[25] Y. She, C. Li, J. Cleary, and H.-J. Su, "Design and fabrication of a soft robotic hand with embedded actuators and sensors," *Journal of Mechanisms and Robotics*, vol. 7, no. 2, 2015.

[26] C. Laschi, M. Cianchetti, B. Mazzolai, L. Margheri, M. Follador, and P. Dario, "Soft robot arm inspired by the octopus," *Advanced Robotics*, vol. 27, no. 7, pp. 709–727, 2012.

[27] I. Gaponov, D. Popov, and J. H. Ryu, "Twisted string actuation systems: A study of the mathematical model and a comparison of twisted strings," *IEEE/ASME Transactions on Mechatronics*, vol. 19, no. 4, pp. 1331–1342, 2014.

[28] D. Bombara, R. Konda, Z. Kibria, and J. Zhang, "Inverse modeling for component selection of twisted string actuators," *IEEE/ASME Transactions on Mechatronics*, vol. 28, no. 2, pp. 1047–1058, 2023.

[29] J. Shintake, V. Cacucciolo, D. Floreano, and H. Shea, "Soft robotic grippers," *Advanced Materials*, vol. 30, no. 29, p. 1707035, 2018.

[30] I. Gaponov, D. Popov, S. J. Lee, and J.-H. Ryu, "Auxilio: A portable cable-driven exosuit for upper extremity assistance," *International Journal of Control, Automation and Systems*, vol. 15, no. 1, pp. 73–84, 2017.

[31] I. W. Park and V. SunSpiral, "Impedance controlled twisted string actuators for tensegrity robots," in *Proceedings of International Conference of Control, Automation and Systems*, 2014, pp. 1331–1338.

[32] Y. J. Shin, H. J. Lee, K.-S. Kim, and S. Kim, "A robot finger design using a dual-mode twisting mechanism to achieve high-speed motion and large grasping force," *IEEE Transactions on Robotics*, vol. 28, no. 6, pp. 1398–1405, 2012.

[33] T. Tsabedze, E. Hartman, and J. Zhang, "A compact, compliant, and biomimetic robotic assistive glove driven by twisted string actuators," *International Journal of Intelligent Robotics and Applications*, vol. 5, no. 3, pp. 381–394, 2021.

[34] J. I. Kim, J. Choi, J. Kim, and Y.-L. Park, "A twisted elastic rotary-rail actuator (terra) using a double-stranded helix structure," *IEEE Robotics and Automation Letters*, vol. 6, no. 4, pp. 7381–7388, 2021.

[35] D. Lee, D. H. Kim, C. H. Che, J. B. In, and D. Shin, "Highly durable bidirectional joint with twisted string actuators and variable radius pulley," *IEEE/ASME Transactions on Mechatronics*, vol. 25, no. 1, pp. 360–370, 2020.

[36] R. Müller, M. Hessinger, H. Schlaak, and P. Pott, "Modelling and characterisation of twisted string actuation for usage in active knee orthoses," *IFAC-PapersOnLine*, vol. 48, no. 20, pp. 207–212, 2015, 9th IFAC Symposium on Biological and Medical Systems BMS 2015.

[37] R. Shisheie, L. Jiang, L. Banta, and M. Cheng, "Modeling and control of a bidirectional twisted-string actuation for an upper arm robotic device," *Proceedings of the American Control Conference*, pp. 5794–5799, 2015.

[38] D. Popov, I. Gaponov, and J. Ryu, "Bidirectional elbow exoskeleton based on twisted-string actuators," in *2013 IEEE/RSJ International Conference on Intelligent Robots and Systems*, 2013, pp. 5853–5858.

[39] M. Hosseini, R. Meattini, A. San-Millan, G. Palli, C. Melchiorri, and J. Paik, "A sEMG-driven soft exosuit based on twisted string actuators for elbow assistive applications," *IEEE Robotics and Automation Letters*, vol. 5, no. 3, pp. 4094–4101, 2020.

[40] D. Bombara, R. Konda, and J. Zhang, "Experimental characterization and modeling of the self-sensing property in compliant twisted string actuators," *IEEE Robotics and Automation Letters*, vol. 6, no. 2, pp. 974–981, 2021.

[41] D. Bombara, S. Fowzer, and J. Zhang, "Compliant, large-strain, and self-sensing twisted string actuators," *Soft Robotics*, vol. 9, no. 1, pp. 72–88, 2022.

[42] T. Helps, M. Taghavi, S. Wang, and J. Rossiter, "Twisted rubber variable-stiffness artificial muscles," *Soft Robotics*, vol. 7, no. 3, pp. 386–395, 2020.

[43] R. Konda, D. Bombara, S. Swanbeck, and J. Zhang, "Anthropomorphic twisted string-actuated soft robotic gripper with tendon-based stiffening," *IEEE Transactions on Robotics*, pp. 1–18, 2022.

[44] D. Bombara, R. Coulter, R. Konda, and J. Zhang, "A twisted string actuator-driven soft robotic manipulator," in *2021 Modeling, Estimation, and Control Conference (MECC)*, 2021.

[45] D. Bombara, R. Konda, E. Chow, and J. Zhang, "Physics-based kinematic modeling of a twisted string actuator-driven soft robotic manipulator," in *2022 American Control Conference (ACC)*, 2022.

[46] R. Konda, D. Bombara, E. Chow, and J. Zhang, "Kinematic Modeling and Open-Loop Control of a Twisted String Actuator-Driven Soft Robotic Manipulator," *Journal of Mechanisms and Robotics*, vol. 16, no. 4, p. 041007, 2023.

[47] J.-B. Chossat, D. K. Chen, Y.-L. Park, and P. B. Shull, "Soft wearable skin-stretch device for haptic feedback using twisted and coiled polymer actuators," *IEEE Transactions on Haptics*, vol. 12, no. 4, pp. 521–532, 2019.

[48] M. Hosseini, A. Sengül, Y. Pane, J. De Schutter, and H. Bruyninck, "Exoten-glove: A force-feedback haptic glove based on twisted string actuation system," in *2018 27th IEEE International Symposium on Robot and Human Interactive Communication (RO-MAN)*. IEEE, 2018, pp. 320–327.

[49] G. Palli, C. Natale, C. May, C. Melchiorri, and T. Wurtz, "Modeling and control of the twisted string actuation system," *IEEE/ASME Transactions on Mechatronics*, vol. 18, no. 2, pp. 664–673, 2013.

[50] A. Savitzky and M. J. E. Golay, "Smoothing and differentiation of data by simplified least squares procedures," *Analytical Chemistry*, vol. 36, no. 8, pp. 1627–1639, 1964.

[51] G. Palli, M. Hosseini, and C. Melchiorri, "Twisted string actuation with sliding surfaces," in *2016 IEEE/RSJ International Conference on Intelligent Robots and Systems (IROS)*, 2016, pp. 260–265.

[52] B. Suthar, M. Usman, H. Seong, I. Gaponov, and J.-H. Ryu, "Preliminary study of twisted string actuation through a conduit toward soft and wearable

actuation," in *2018 IEEE International Conference on Robotics and Automation (ICRA)*, 2018, pp. 2260–2265.

[53] T. George Thuruthel, F. Renda, and F. Iida, "First-order dynamic modeling and control of soft robots," *Frontiers in Robotics and AI*, vol. 7, 2020.

[54] M. S. Xavier, A. J. Fleming, and Y. K. Yong, "Finite element modeling of soft fluidic actuators: Overview and recent developments," *Advanced Intelligent Systems*, vol. 3, no. 2, p. 2000187, 2021.

[55] J. Till, V. Aloi, and C. Rucker, "Real-time dynamics of soft and continuum robots based on cosserat rod models," *The International Journal of Robotics Research*, vol. 38, no. 6, pp. 723–746, 2019.

[56] B. Pawlowski, J. Sun, J. Xu, Y. Liu, and J. Zhao, "Modeling of soft robots actuated by twisted-and-coiled actuators," *IEEE/ASME Transactions on Mechatronics*, vol. 24, no. 1, pp. 5–15, 2019.

[57] P. Rao, Q. Peyron, S. Lilge, and J. Burgner-Kahrs, "How to model tendon-driven continuum robots and benchmark modelling performance," *Frontiers in Robotics and AI*, vol. 7, 2021.

[58] M. Moradi Dalvand, S. Nahavandi, and R. D. Howe, "General forward kinematics for tendon-driven continuum robots," *IEEE Access*, vol. 10, pp. 60 330–60 340, 2022.

[59] A. S.-M. Rodriguez, M. Hosseini, and J. Paik, "Hybrid control strategy for force and precise end effector positioning of a twisted string actuator," *IEEE/ASME Transactions on Mechatronics*, vol. 26, no. 5, pp. 2791–2802, 2020.

[60] A. Baker, C. Foy, S. Swanbeck, R. Konda, and J. Zhang, "Star–2: A soft twisted-string-actuated anthropomorphic robotic gripper: Design, fabrication,

and preliminary testing," in *2023 IEEE/ASME International Conference on Advanced Intelligent Mechatronics (AIM)*, 2023, pp. 643–648.

[61] X. Huang, J. Zou, and G. Gu, "Kinematic modeling and control of variable curvature soft continuum robots," *IEEE/ASME Transactions on Mechatronics*, vol. 26, no. 6, pp. 3175–3185, 2021.

[62] D. Lee, S. Kim, H.-J. Park, S. Kim, and D. Shin, "A spine assistive robot with a routed twisted string actuator and a flat-back alleviation mechanism for lumbar-degenerative flat back," *IEEE/ASME Transactions on Mechatronics*, pp. 1–12, 2022.

[63] M. W. Hannan and I. D. Walker, "Kinematics and the implementation of an elephant's trunk manipulator and other continuum style robots," *Journal of Robotic Systems*, vol. 20, no. 2, pp. 45–63, 2003.

[64] H. Lee, H. Choi, and S. Park, "Accurate modeling and nonlinearity compensation in the speed mode of a twisted string actuator," *Mechanism and Machine Theory*, vol. 137, pp. 53–66, 2019.

[65] S. Nedelchev, I. Gaponov, and J.-H. Ryu, "Accurate dynamic modeling of twisted string actuators accounting for string compliance and friction," *IEEE Robotics and Automation Letters*, vol. 5, no. 2, pp. 3438–3443, 2020.

[66] C. Lin, C. Lin, S. Yu, and C. Chen, "Hysteresis modeling and tracking control for a dual pneumatic artificial muscle system using Prandtl-Ishlinskii model," *Mechatronics*, vol. 28, pp. 35–45, 2015.

[67] M. Wehner, Y. Park, C. Walsh, R. Nagpal, R. J. Wood, T. Moore, and E. Goldfield, "Experimental characterization of components for active soft orthotics,"

ser. 4th IEEE RAS and EMBS International Conference Biomedical Robotics and Biomechatronics, 2012.

[68] J. Li and H. Tian, "Position control of sma actuator based on inverse empirical model and smc-rbf compensation," *Mechanical Systems and Signal Processing*, vol. 108, pp. 203–215, 2018.

[69] M. C. Yip and G. Niemeyer, "High-performance robotic muscles from conductive nylon sewing thread," in *Proc. IEEE Int. Conf. Robot. Autom.*, 2015, pp. 2313–2318.

[70] J. Zhang, A. Simeonov, and M. C. Yip, "Three-dimensional hysteresis compensation enhances accuracy of robotic artificial muscles," *Smart Mater. Struct.*, vol. 27, no. 3, p. 035002, 2018.

[71] I. Mayergoyz, *Mathematical models of hysteresis*. Springer-Verlag, 1991.

[72] X. Tan and J. Baras, "Modeling and control of hysteresis in magnetostrictive actuators," *Automatica*, vol. 40, no. 9, pp. 1469–1480, 2004.

[73] C. Cisse, W. Zaki, and T. B. Zineb, "A review of constitutive models and modeling techniques for shape memory alloys," *Int. J. Plasticity*, vol. 76, pp. 244–284, 2016.

[74] V. Hassani, T. Tjahjowidodo, and T. N. Do, "A survey on hysteresis modeling, identification and control," *Mechanical Systems and Signal Processing*, vol. 49, no. 1, pp. 209–233, 2014. [Online]. Available: https://www.sciencedirect.com/science/article/pii/S0888327014001186

[75] T. Vo-Minh, T. Tjahjowidodo, H. Ramon, and H. Van Brussel, "A new approach to modeling hysteresis in a pneumatic artificial muscle using the maxwell-slip

model," *IEEE/ASME Transactions on Mechatronics*, vol. 16, no. 1, pp. 177–186, 2011.

[76] F. Schreiber, Y. Sklyarenko, K. Schlüter, J. Schmitt, S. Rost, A. Raatz, and W. Schumacher, "Tracking control with hysteresis compensation for manipulator segments driven by pneumatic artificial muscles," in *2011 IEEE International Conference on Robotics and Biomimetics*, 2011, pp. 2750–2755.

[77] Y. Guo, J. Mao, and K. Zhou, "Rate-dependent modeling and H_∞ robust control of gma based on hammerstein model with preisach operator," *IEEE Transactions on Control Systems Technology*, vol. 23, no. 6, pp. 2432–2439, 2015.

[78] Y. Shan and K. K. Leang, "Accounting for hysteresis in repetitive control design: Nanopositioning example," *Automatica*, vol. 48, no. 8, pp. 1751 – 1758, 2012.

[79] X. Chen, Y. Feng, and C.-Y. Su, "Adaptive control for continuous-time systems with actuator and sensor hysteresis," *Automatica*, vol. 64, pp. 196 – 207, 2016.

[80] U. Gupta, Y. Wang, H. Ren, and J. Zhu, "Dynamic modeling and feedforward control of jaw movements driven by viscoelastic artificial muscles," *IEEE/ASME Transactions on Mechatronics*, vol. 24, no. 1, pp. 25–35, 2019.

[81] S. Liu, C. Su, and Z. Li, "Robust adaptive inverse control of a class of nonlinear systems with Prandtl-Ishlinskii hysteresis model," *IEEE Transactions on Automatic Control*, vol. 59, no. 8, pp. 2170–2175, 2014.

[82] J. Liu, J. Wang, and Q. Zou, "Decomposition-learning-based output tracking to simultaneous hysteresis and dynamics control: High-speed large-range nanopositioning example," *IEEE Transactions on Control Systems Technology*, pp. 1–8, 2020.

[83] R. Konda and J. Zhang, "Hysteresis with lonely stroke in artificial muscles: Characterization, modeling, and inverse compensation," *Mechanical Systems and Signal Processing*, vol. 164, p. 108240, 2022.

[84] R. Konda and J. Zhang, "Modeling and inverse compensation of the quasi-static voltage-strain lonely stroke and hysteresis in supercoiled polymer artificial muscles," in *American Control Conference*, 2021.

[85] M. Usman, H. Seong, B. Suthar, I. Gaponov, and J. H. Ryu, "A study on life cycle of twisted string actuators: Preliminary results," *in Proceedings of IEEE/RSJ International Conference on Intelligent Robots and Systems*, pp. 2789–2794, 2017.

[86] L. Jiang, R. Shisheie, M. Cheng, and E. Bakhoum, "Controller synthesis for assistive robotic device using twisted-string actuation," in *2015 American Control Conference (ACC)*, 2015, pp. 2248–2253.

[87] J. H. Wiest and G. D. Buckner, "Indirect intelligent sliding mode control of antagonistic shape memory alloy actuators using hysteretic recurrent neural networks," *IEEE Transactions on Control Systems Technology*, vol. 22, no. 3, pp. 921–929, 2014.

[88] R. Konda, E. Hartman, and J. Zhang, "A bio-inspired multi-directional HASEL actuator-driven soft robotic tail: design and characterization," in *Electroactive Polymer Actuators and Devices (EAPAD) XXV*, vol. 12482. SPIE, 2023, p. 124820M. [Online]. Available: https://doi.org/10.1117/12.2656884

[89] S. Shakiba, M. Ourak, E. V. Poorten, M. Ayati, and A. Yousefi-Koma, "Modeling and compensation of asymmetric rate-dependent hysteresis of a minia-

ture pneumatic artificial muscle-based catheter," *Mechanical Systems and Signal Processing*, vol. 154, p. 107532, 2021.

[90] G. Heo, K.-h. Pyo, D. H. Lee, Y. Kim, and J.-W. Kim, "Critical role of Diels-Adler adducts to realise stretchable transparent electrodes based on silver nanowires and silicone elastomer," *Scientific Reports*, 2016.

[91] A. Safdel, A. Zarei-Hanzaki, A. Shamsolhodaei, P. Kroob, and T. Niendorf, "Room temperature superelastic responses of NiTi alloy treated by two distinct thermomechanical processing schemes," *Materials Science and Engineering A*, 2017.

[92] D. Vokoun, V. Kafka, and C. T. Hu, "Recovery stresses generated by NiTi shape memory wires under different constraint conditions," *Smart Materials and Structures*, vol. 12, no. 5, pp. 680–685, 2003.

[93] Z. Wang, J. Liu, J. Guo, X. Sun, and L. Xu, "The study of thermal, mechanical and shape memory properties of chopped carbon fiber-reinforced TPI shape memory polymer composites," *Polymers*, vol. 9, no. 11, p. 594, 2017.

[94] R. Konda and J. Zhang, "Experimental investigation of the lonely stroke behavior in supercoiled polymer artificial muscles," ser. Proc. SPIE Electroactive Polymer Actuators and Devices (EAPAD), 2020.

[95] G. Cybenko, "Approximation by superposition of a sigmoidal function," *Mathematics of Controls, Signals, and Systems*, vol. 2, pp. 303–314, 1989.

[96] K. Hornik, M. Stinchcombe, and H. White, "Universal approximation of an unknown mapping and its derivatives using multilayer feedforward networks," *Neural Networks*, vol. 3, no. 5, pp. 551–560, 1990.

[97] R. K. Luo, "Mullins damage effect on rubber products with residual strain," *International Journal of Damage Mechanics*, vol. 24, no. 2, pp. 153–167, 2015.

[98] M. A. Janaideh, M. Saaideh, and M. Rakotondrabe, "On hysteresis modeling of a piezoelectric precise positioning system under variable temperature," *Mechanical Systems and Signal Processing*, vol. 145, 2020.

[99] J. Ahrens, X. Tan, and H. K. Khalil, "Multirate sampled-data output feedback control with application to smart material actuated systems," *IEEE Trans. Automat. Contr.*, vol. 54, no. 11, pp. 2518–2529, 2009.

[100] I. Mayergoyz and G. Friedman, "Generalized preisach model of hysteresis," *IEEE Trans. Magn.*, vol. 24, no. 1, pp. 212–217, 1988.

[101] J. Zhang, E. Merced, N. Sepúlveda, and X. Tan, "Kullback-leibler divergence-based optimal compression of Preisach operator in hysteresis modeling," in *2013 American Control Conference*, 2013, pp. 89–94.

[102] Xiaobo Tan and J. S. Baras, "Adaptive identification and control of hysteresis in smart materials," *IEEE Transactions on Automatic Control*, vol. 50, no. 6, pp. 827–839, 2005.

[103] J. Zhang, D. Torres, J. L. Ebel, N. Sepúlveda, and X. Tan, "A composite hysteresis model in self-sensing feedback control of fully-integrated VO_2 microactuators," *IEEE/ASME Trans. Mech.*, vol. 21, no. 5, pp. 2405–2417, 2016.

[104] J. Zhang, D. Torres, N. Sepulveda, and X. Tan, "A compressive sensing based-approach for Preisach hysteresis model identification," *Smart Materials and Structures*, vol. 25, pp. 1–12, 2016.

[105] R. Konda, D. Bombara, and J. Zhang, "Parameter estimation and adaptive control of twisted string actuators," in *2022 IEEE/ASME International Conference on Advanced Intelligent Mechatronics (AIM)*, 2022, pp. 1366–1371.

[106] D. Popov, I. Gaponov, and J. H. Ryu, "Towards variable stiffness control of antagonistic twisted string actuators," *IEEE International Conference on Intelligent Robots and Systems*, no. Iros, pp. 2789–2794, 2014.

[107] M. Tavakoli, R. Batista, and P. Neto, "A compact two-phase twisted string actuation system: Modeling and validation," *Mechanism and Machine Theory*, vol. 101, pp. 23–35, 2016.

[108] S. Nedelchev, I. Gaponov, and J.-H. Ryu, "High-bandwidth control of twisted string actuators," in *2019 International Conference on Robotics and Automation (ICRA)*, 2019, pp. 5359–5364.

[109] I. Godler and T. Sonoda, "A five fingered robotic hand prototype by using twist drive," in *ISR 2010 (41st International Symposium on Robotics) and ROBOTIK 2010 (6th German Conference on Robotics)*. VDE, 2010, pp. 1–6.

[110] P. Ioannou and B. Fidan, *Adaptive control tutorial*. SIAM, 2006.

[111] R. Konda, D. Bombara, and J. Zhang, "Overtwisting and coiling highly enhances strain generation of twisted string actuators," *Soft Robotics*, vol. 10, no. 4, pp. 760–769, 2023.

[112] T. Inoue, S. Yamamoto, R. Miyata, and S. Hirai, "Robotic joint design by agonist and antagonist arrangement with twisting small-diameter round-belts," in *2015 IEEE/RSJ International Conference on Intelligent Robots and Systems (IROS)*, 2015, pp. 1751–1756.

[113] C. S. Haines, M. D. Lima, N. Li, G. M. Spinks, J. Foroughi, J. D. Madden, S. H. J. Kim, S. Fang, M. Jung de Andrade, F. Goktepe, O. Goktepe, S. M. Mirvakili, S. Naficy, X. Lepro, J. Oh, M. E. Kozlov, S. H. J. Kim, X. Xu, B. J. Swedlove, G. G. Wallace, and R. H. Baughman, "Artificial muscles from fishing line and sewing thread," *Science*, vol. 343, no. 6173, pp. 868–872, 2014.

[114] A. Abbas and J. Zhao, "Twisted and coiled sensor for shape estimation of soft robots," *IEEE International Conference on Intelligent Robots and Systems*, pp. 482–487, 2017.

[115] H. S. Seong, D. H. Kim, I. Gaponov, and J. H. Ryu, "Development of a twisted string actuator-based exoskeleton for hip joint assistance in lifting tasks," in *2020 IEEE International Conference on Robotics and Automation (ICRA)*, 2020, pp. 761–767.

[116] L. Jiang, R. Shisheie, M. H. Cheng, L. E. Banta, and G. Guo, "Moving trajectories and controller synthesis for an assistive device for arm rehabilitation," in *2013 IEEE International Conference on Automation Science and Engineering (CASE)*, 2013, pp. 268–273.

[117] S. Zhao, Y. Yang, Y. Gao, Z. Zhang, T. Zheng, and Y. Zhu, "Development of a soft knee exosuit with twisted string actuators for stair climbing assistance," in *2019 IEEE International Conference on Robotics and Biomimetics (ROBIO)*, 2019, pp. 2541–2546.

[118] K. Olsen and J. Bohr, "The generic geometry of helices and their close-packed structures," *Theor Chem Acc*, vol. 125, pp. 207–215, 2010.

[119] G. M. Spinks, N. D. Martino, S. Naficy, D. J. Shepherd, and J. Foroughi,

"Dual high-stroke and high-work capacity artificial muscles inspired by dna supercoiling," *Science Robotics*, vol. 6, no. 53, p. eabf4788, 2021.

[120] T. Sonoda and I. Godler, "Multi-fingered robotic hand employing strings transmission named "twist drive"," in *2010 IEEE/RSJ International Conference on Intelligent Robots and Systems*, 2010, pp. 2733–2738.

[121] Y. Yang, Z. Liu, Y. Wang, S. Liu, and M. Y. Wang, "A compact and low-cost robotic manipulator driven by supercoiled polymer actuators," in *2020 IEEE International Conference on Robotics and Automation (ICRA)*, 2020.

[122] G. Palli, M. Hosseini, L. Moriello, and C. Melchiorri, "Modeling and identification of a variable stiffness joint based on twisted string actuators," in *2015 IEEE/RSJ International Conference on Intelligent Robots and Systems (IROS)*, 2015, pp. 1757–1762.

[123] T. Tsabedze, E. Hartman, E. Abrego, C. Brennan, and J. Zhang, "TSA-BRAG: A twisted string actuator-powered biomimetic robotic assistive glove," in *2020 International Symposium on Medical Robotics (ISMR)*. IEEE, 2020, pp. 159–165.

[124] M. Stevens and A. S. Kernbaum, "Twisted string actuators for exo-suits," in *Proc. IEEE/RSJ Int. Conf. Intell. Robot. Syst., Workshop on Twisted String Actuation: State of the Art, Challenges and New Applications*, 2016.

[125] K. Ogura, S. Wakimoto, K. Suzumori, and Y. Nishioka, "Micro pneumatic curling actuator - nematode actuator," in *2008 IEEE International Conference on Robotics and Biomimetics*, 2009, pp. 462–467.

[126] K. K. Leang and S. Devasia, "Feedback-linearized inverse feedforward for creep,

hysteresis, and vibration compensation in afm piezoactuators," *IEEE Transactions on Control Systems Technology*, vol. 15, no. 5, pp. 927–935, 2007.

[127] P. Krejci and K. Kuhnen, "Inverse control of systems with hysteresis and creep," *IEE Proceedings - Control Theory and Applications*, vol. 148, no. 3, pp. 185–192, 2001.

[128] R. Konda and J. Zhang, "Experimental investigation of the non-smooth actuation in twisted and coiled string artificial muscles," in *2023 SPIE Conference on Bioinspiration, Biomimetics, and Bioreplication XIII*, 2023.

[129] ——, "The effects of nylon polymer threads on hysteresis behavior of supercoiled polymer (SCP) artificial muscles," in *Proc. ASME Dynamic Systems and Control Conf.*, Paper DSCC2019-9169, 2019.

[130] Y. Kim, S. S. Cheng, A. Ecins, C. Fermüller, K. P. Westlake, and J. P. Desai, "Towards a robotic hand rehabilitation exoskeleton for stroke therapy," in *Proc. ASME Dyn. Syst. Contr. Conf.*, 2014, p. V001T04A006.

[131] Y. J. Shin, K.-H. Rew, K.-S. Kim, and S. Kim, "Development of anthropomorphic robot hand with dual-mode twisting actuation and electromagnetic joint locking mechanism," in *2013 IEEE International Conference on Robotics and Automation*, 2013, pp. 2759–2764.

[132] M. Tavakoli, R. Batista, and L. Sgrigna, "The UC softhand: Light weight adaptive bionic hand with a compact twisted string actuation system," *Actuators*, vol. 5, no. 1, 2016.

[133] S. Aziz, S. Naficy, J. Foroughi, H. R. Brown, and G. M. Spinks, "Twist–coil coupling fibres for high stroke tensile artificial muscles," *Sensors and Actuators A: Physical*, vol. 283, pp. 98–106, 2018.

[134] N. Charles, M. Gazzola, and L. Mahadevan, "Topology, geometry, and mechanics of strongly stretched and twisted filaments: Solenoids, plectonemes, and artificial muscle fibers," *Phys. Rev. Lett.*, vol. 123, p. 208003, Nov 2019.

[135] M. Gazzola, L. H. Dudte, A. G. McCormick, and L. Mahadevan, "Forward and inverse problems in the mechanics of soft filaments," *R. Soc. Open Sci*, vol. 5, p. 171628, 2018.

[136] J. Sun and J. Zhao, "Physics-based modeling of twisted-and-coiled actuators using cosserat rod theory," *IEEE Transactions on Robotics*, vol. 38, no. 2, pp. 779–796, 2022.

[137] J. Coyne, "Analysis of the formation and elimination of loops in twisted cable," *IEEE Journal of Oceanic Engineering*, vol. 15, no. 2, pp. 72–83, 1990.

[138] J. Hu, L. Liu, L. Zeng, Y. He, and D. Liu, "Instability of Soft Elastic Filaments Under Torsion: Experiment and Analysis," *Journal of Applied Mechanics*, vol. 89, no. 5, p. 051001, 02 2022.

[139] C. O. Horgan and J. G. Murphy, "Kinking Instability in the Torsion of Stretched Anisotropic Elastomeric Filaments ," *Journal of Elasticity*, vol. 122, no. 2, pp. 197–209, 2016.

[140] A. Ghatak and L. Mahadevan, "Solenoids and plectonemes in stretched and twisted elastomeric filaments," *Phys. Rev. Lett.*, vol. 95, p. 057801, Jul 2005.

[141] R. Iyer and X. Tan, "Control of hysteretic systems through inverse compensation," *IEEE Contr. Syst. Mag.*, vol. 29, no. 1, pp. 83–99, 2009.